4-5-2019 3:00 PM

Non-Classical Nucleation Phenomena Study And Following Process Monitoring and Optimization in Solution Crystallization Process

Zhenguo Gao
Western University

Supervisor
Sohrab Rohani
The University of Western Ontario

Graduate Program in Chemical and Biochemical Engineering
A thesis submitted in partial fulfillment of the requirements for the degree in Doctor of Philosophy
© Zhenguo Gao 2019

Abstract

Nucleation is a crucial step in the solution crystallization process. Despite the intensive study on nucleation, classical nucleation theory and two-step nucleation theory cannot explain all the nucleation phenomena, especially for the non-classical nucleation phenomena which include oiling out, gelation and non-monotonic nucleation. Accordingly, for the non-classical nucleation systems, the crystallization processes are seldom designed based on the nucleation monitoring and supervision. In this thesis, crystallization process optimization was conducted to study the mechanism of non-classical nucleation phenomena and in-line process monitoring technology development.

Two kinds of non-classical nucleation phenomena with non-monotonic nucleation rate and gel formation were investigated, and accordingly, two nucleation pathways that self-induced nucleation and jellylike phase mediated nucleation were proposed based on the analysis of in-line spectral monitoring and off-line sample characterizations. Results indicated the agitation level would affect the pre-nucleation clusters' existence in the non-monotonic nucleation system, and the properties of solvent determined the formation of jellylike phase and the transformation to crystals. Motion-based objects tracking model and the state-of-the-art neural network Mask R-CNN were introduced to monitor the onset of nucleation and following the crystallization process. Combined with a cost-effective camera probe, the developed real-time tracking system can detect the nucleation onset accurately even with ultrasonic irradiation and can extract much more information during the whole crystallization process. Subsequently, ultrasonic irradiation, and seeding were used to optimize a non-classical nucleation system that accompanied oiling out phenomenon. Different frequencies and intensities of ultrasonic irradiation and seeds addition time were screened to optimize the nucleation step, which proved their effectiveness of promoting nucleation and narrowing the metastable zone widths of oiling out and nucleation. A fine-tuning of nucleation step was carried out in a mixed suspension mixed product removal (MSMPR)-tubular crystallizer series. The nucleation step was optimized in the MSMPR stage with the aid of principal component analysis, which enabled growth of crystals in the tubular crystallizer with preferred polymorphism, shape, and size. The study in this thesis provides insights into non-classical nucleation mechanism and nucleation based crystallization process design and optimization.

i

Keywords

Co-Authorship Statement

Chapter 1: Zhenguo Gao prepared the original manuscript, including collecting references, writing the manuscript. Professor Sohrab Rohani reviewed and revised the manuscript, Professor Jingkang Wang and Professor Junbo Gong gave directions at the time of writing the manuscript.

Chapter 2: Zhenguo Gao prepared the original draft, including conducting experiments, processing data, writing the manuscript. Professor Sohrab Rohani reviewed and revised this manuscript. A version of this chapter has been published in the journal Crystal Growth & Design:

Gao Z, Wu Y, Wu Y, Gong J, Bao Y, Wang J, Rohani S. Self-induced Nucleation During Anti-Solvent Crystallization Process of Candesartan Cilexetil. *Crystal Growth & Design*. 2018, 18 (12), 7655–7662

Yang Wu and Yuanyi Wu helped to conduct this experiments, Professor Jingkang Wang, Professor Junbo Gong and Professor Ying Bao reviewed the manuscript and gave advice for improvement.

Chapter 3: Zhenguo Gao conducted the experiments and prepared the original manuscript. Professor Ying Bao aided with experiments design, data analysis, and revised the manuscript. A version of this chapter has been published in the journal Industrial & Engineering Chemistry Research:

Gao Z, Li L, Bao Y, Wang Z, Hao H, Yin Q, Wang J. From jellylike phase to crystal: Effects of solvent on self-assembly of cefotaxime sodium. *Industrial & Engineering Chemistry Research*. 2016, 55(11), 3075-3083

Long Li helped to analyse the experimental data, Professor Zhao Wang, Hongxun Hao, Qiuxiang Yin, and Jingkang Wang reviewed the manuscript and provided improvement suggestions.

Chapter 4: Zhenguo Gao prepared the manuscript, including running the experiments, writing the manuscript. Professor Sohrab Rohani reviewed and revised the manuscript. A version of this manuscript has been published in the journal Crystal Growth & Design:

Gao Z, Zhu D, Wu Y, Rohani S, Gong J, Wang J. Motion-Based Multiple Object Tracking of Ultrasonic-Induced Nucleation: A Case Study of l-Glutamic Acid. *Crystal Growth & Design*. 2017 17(10), 5007-5011

Dan Zhu and Yuanyi Wu helped to run the experiments, Professor Junbo Gong and Professor Jingkang Wang gave directions during conducting the experiments.

Chapter 5: The manuscript was prepared by Zhenguo Gao, including design the experiment and writing the manuscript. Yuanyi Wu constructed the neural network, Fatima Altimimi and Brandon Julien helped to annotate the training dataset. A version of this chapter has been published in the journal Crystal Growth & Design:

Gao Z, Wu Y, Bao Y, Gong J, Wang J, Rohani S. Image Analysis for In-line Measurement of Multidimensional Size, Shape, and Polymorphic Transformation of l-Glutamic Acid Using Deep Learning-Based Image Segmentation and Classification. *Crystal Growth & Design*. 2018, 18(8), 4275-4281

Professor Sohrab Rohani reviewed and revised the manuscript, Professor Ying Bao, Junbo Gong, and Professor Jingkang Wang gave recommendations for improvement and revision.

Chapter 6: The manuscript was prepared by Zhenguo Gao, including design the experiment, analyse experimental data, and writing the manuscript. Fatima Altimimi helped to run the experiments and write the manuscript. A version of this chapter has been published in the journal Crystal Growth & Design:

Gao Z, Altimimi F, Gong J, Bao Y, Wang J, Rohani S. Ultrasonic Irradiation and Seeding to Prevent Metastable Liquid-Liquid Phase Separation and Intensify Crystallization. *Crystal Growth & Design*. 2018, 18(4), 2628-2635

Professor Ying Bao and Professor Sohrab Rohani reviewed and revised the manuscript. Professor Junbo Gong and Professor Jingkang Wang gave directions during conducting the experiments.

Chapter 7: Zhenguo Gao prepared the manuscript, including running the experiments, processing the data, and writing the manuscript. Yuanyi Wu helped to run the experiments. A version of this chapter has been published in the Journal of Crystal Growth:

Gao Z, Wu Y, Gong J, Wang J, Rohani S. Continuous crystallization of α-form L-glutamic acid in an MSMPR-Tubular crystallizer system. Journal of Crystal Growth. 2019, 507, 344-351

Professor Sohrab Rohani reviewed and revised the manuscript. Professor Junbo Gong and Professor Jingkang Wang reviewed and gave suggestions to improve the manuscript.

Chapter 8: Zhenguo Gao prepared the manuscript and provided the research suggestions. Professor Sohrab Rohani gave suggestions and revised this section.

Acknowledgments

At the moment of going to finish my Ph.D. degree, I would like to extend my sincerest gratitude to those who made this moment really comes to me. My sincerest appreciation to my supervisor, Professor Sohrab Rohani, for his invaluable knowledge guiding my scientific research and great patience and kindness inspiring me to achieve my best. I greatly appreciate that Professor Rohani is always available to provide expert guidance, direction when I needed, and there is always an opened door for discussion and guidance which has never let me down in the past four years. I cannot make this work possible without continuous support from Tianjin University. Thanks to my supervisor, Professor Jingkang Wang, for her allowing to explore my ideas as well as efforts to cultivate our young generation. I have deeply indebted to my advisors, Professor Junbo Gong and Professor Ying Bao who brought me into the "crystal" world. I appreciate every generous idea with them that from preparing a supersaturated solution to professional career development.

Thanks to the dual Ph.D. degree program supported by China Scholarship Council. Especially thanks to Professor Jesse Zhu, for launching the joint dual Ph.D. degree program between Tianjin University and the University of Western Ontario. Thanks to Professor Yuanyuan Shao for providing generous help to coordinate the joint program. Thanks to the great opportunity that helps to make me better.

To my dear friends and lab members in Tianjin University and the University of Western Ontario who provided ideas and favors and made me everyday meaningful, and also to those who made me upset and forced me to speed up and catch up. Especially thanks to Eddy Wu, Zhaohe Huang, Shichao Du, Long Li who would like to share happiness time with me, call me first for help, and also listen to me, encourage me when I was caught in a thorny issue.

Thanks to my dear family, my grandparents, my parents, my brother, and lovely nephew, who provided me with continuous support and generous love and accompanied me through all the difficulties to make me a better person. I am proud of what they have done, and I hope I have made them proud too.

There are so many others in the past few years that who lent me a hand, did me a favor or just a sweet smile, I would say thank you all and bless you all the best for your future endeavors.

Table of Contents

List of Tables

List of Figures

Nomenclature

Chapter 3: From Jellylike Phase to Crystal: Effects of Solvent on Nucleation of Cefotaxime Sodium

JLP	Jellylike phase
CTX	Cefotaxime sodium
LLPS	Liquid-liquid phase separation
PLM	Polarized light microscopy
J1	Jellylike phase 1 formed in anti-solvent experimental section
C1	Crystals 1 transformed from jellylike phase 1
J2	Jellylike phase 2 formed in cooling crystallization section
C2	Crystals 2 transformed from jellylike phase 2
J3	Jellylike phase 3 formed in adsorption experimental section
C3	Crystals 3 transformed from jellylike phase 3
J/Jp	Amorphous phase transforms to jellylike phase completely or partly (in Table 3-1 and Table 3-2)
C/Cp	Jellylike phase transforms to crystals completely or partly (in Table 3-1)

Chapter 4: Motion-Based Multiple Object Tracking of Ultrasonic-Induced Nucleation: A Case Study of L-Glutamic Acid

c	Crystal counts in equation 4-1, #
n	Moving period of object tracking in equation 4-1, second
C_0	Solution concentration, g/L
C*	The concentration of saturated solution, g/L
S_0	Supersaturation calculated by C_0/C^*

Chapter 5: Image Analysis for In-Line Measurement of Multi-Dimensional Size, Shape and Polymorphic Transformation of L-glutamic Acid Using Deep Learning-Based Image Segmentation and Classification

R-CNN	Regional Convolutional Neural Networks
RPN	Region Proposal Network
SMPT	Solvent mediated polymorphic transformation
CSD	Crystal size distribution
CLD	Chord length distribution
CAD	Crystal area distribution
PDF	probability density function

Chapter 6: Ultrasonic Irradiation and Seeding to Prevent Metastable Liquid-Liquid Phase Separation and Intensify Crystallization

LLP	Liquid-liquid phase
MZW	metastable zone width
CSD	Crystal size distribution
Point A	The starting point of ultrasonic experiments with high concentration
Point B	The starting point of ultrasonic experiments with medium concentration
Point C	The starting point of ultrasonic experiments with lower concentration
L_1	Phase 1 among the liquid-liquid phase separation system
L_2	Phase 2 among the liquid-liquid phase separation system
S	Solid crystals in the phase diagram

7   Continuous Crystallization of α-form L-Glutamic Acid in an MSMPR-Tubular Crystallizer System

CSD	Crystal size distribution
OBC	Oscillatory baffled crystallizer
MSMPR	Mixed Suspension Mixed Product Removal
S_0	Initial supersaturation
T_n	Nucleation temperature, °C

N	Stirring speed, rpm
f	Flowrate, mL/min
R_t	Residence time, min
V_e	Effective volume, mL
M	Suspension density, kg/m^3
B	Secondary nucleation rate, number/(volume · min)
$Sdtv$	Standard deviation
DNC	Direct nucleation control

Chapter 1

Introduction

1. Introduction

Abstract

Crystallization is one of the oldest separations and purification unit operations and has recently contributed to significant improvements in producing higher-value products with specific properties and in building efficient manufacturing processes. There are two main steps in a crystallization process, crystal nucleation and growth. Nucleation is a crucial step to determine the product qualities including purity, polymorphism, morphology, crystal size, etc. as well as process robustness and efficiency. In the past few years, there has been an increasing effort on the understanding of the non-classical nucleation phenomena e.g. oiling out, gelation, nucleation retardation, occurring in the pharmaceutical crystallization processes. These undesirable phenomena seriously affect the product quality or even interrupt the crystallization process. In this study, two kinds of non-classical nucleation phenomena including non-monotonic nucleation rate with the stirring speed, and gelation phenomenon were studied. In addition, two new methods i.e. motion-based nucleation tracking and deep learning-based image analysis were developed to improve the accuracy of monitoring of nucleation and crystallization. At last, ultrasonic irradiation and seeding were studied to optimize crystallization process that accompanied with oiling out phenomenon. An innovative combined MSMPR-tubular continuous crystallization configuration was developed to deal with the crystallization of crystallization products. This study provides insights to the non-classical nucleation mechanism, methods of following process monitoring, and effective optimization of non-classical nucleation systems.

1.1. Background

Nucleation is the initial step in solution crystallization. It involves the emergence of a new phase that assembles the solute molecules in nanoscale into microscale dimension particles (crystals). Nucleation rate often determines the crystal properties as well as the kinetics of crystallization process. Understanding of the nucleation mechanism is the inevitable step to realize the control of nucleation and the whole crystallization process. Despite its importance and intense study of nucleation, there are still many unknowns and variations

with the changes of model compounds and experimental conditions. Beyond the classical nucleation theory (CNT), the two-step nucleation theory (TNT) attracted much attention in the past few years, which provides an alternative route to explain the nucleation phenomena that the classical nucleation theory cannot explain. Apart from the nucleation phenomena, non-classical nucleation phenomena were reported frequently in the past few years [1, 2]. For example, oiling out or liquid-liquid phase separation, gelation, and nucleation retardation, in which an intermediate phase emerges before crystal nucleation, are among the difficult phenomena that cannot be explained by the classical nucleation theory. Understanding the mechanism of intermediate phase formation proceeding the nucleation occurrence is essential to getting control of nucleation progress.

1.1.1. Non-classical nucleation phenomenon

The non-classical nucleation phenomena included in this study contain gelation and non-monotonic nucleation phenomena during the anti-solvent crystallization process. In the pharmaceutical crystallization process, as the drug molecules are becoming bigger and the functional groups become much more complex, non-classical nucleation phenomena including oiling out, gelation, non-monotonic nucleation, and nucleation retardation etc., occur increasingly. The oil phase and gel phase can inhibit the nucleation that may lead to the loss of nucleation control or eventually interrupt the operation.

Oiling out which is also known as liquid-liquid phase separation is the formation of a second liquid phase during solution crystallization processes, which may occur in reaction, cooling, anti-solvent, evaporation, or the combination of those techniques. Along with the generation of supersaturation e.g. by cooling, adding anti-solvent, the mixture can be potentially separated into different phases of pure components while the Gibbs free energy of mixing is greater than zero. There is another possibility that the mixture does not separate into pure components and an a^* component rich phase and a b^* component rich phase may be formed. As shown in Figure 1-1 (1), during cooling or addition of anti-solvent process, the metastable zone may be formed between the binodal curve and spinodal curve. The area above the binodal curve and the area below the spinodal curve are stable and unstable status, respectively, and the unstable phase will directly go through a crystallization process. From the thermodynamic view, as indicated in Figure 1-1 (2), the component a^* or b^*

cannot dissolve into another as the Gibbs free energy of mixing is greater than zero over the entire range of composition and those two components will exist in completely immiscible phase like curve 1 (equation 1-1). Curve 3 indicates a totally miscible system in which the Gibbs free energy of mixing is positive and the second derivative of ΔG_{mix} over the composition x_i is negative (equation 1-2). The curves 1 and 3 are not in the consideration of crystallization process, and curve 2 exists in the crystallization process that the oiling out phenomenon will occur due to the existence of local minima points of Gibbs free energy like p_1 and p_4. The Gibbs free energy of mixture with a composition between p_1 and p_4 is lower than p_1 and p_4 which are known as the binodal points. Between p_1 and p_4 (equation 1-3), the spinodal points p_2 and p_3 exist beyond which the solution is unstable and will separate into two liquid phases without an energy barrier. The region between p_1 and p_2 and p_3 and p_4 are metastable i.e. the phase separation may occur which has to overcome an energy barrier to initiate a new phase [3].

$$\Delta G_{mix} > 0 \qquad\qquad 1\text{-}1$$

$$\Delta G_{mix} < 0,\ \partial^2 \Delta G_{mix}/\partial^2 x_i < 0 \qquad\qquad 1\text{-}2$$

$$\Delta G_{mix} < 0,\ \partial^2 \Delta G_{mix}/\partial^2 x_i > 0 \qquad\qquad 1\text{-}3$$
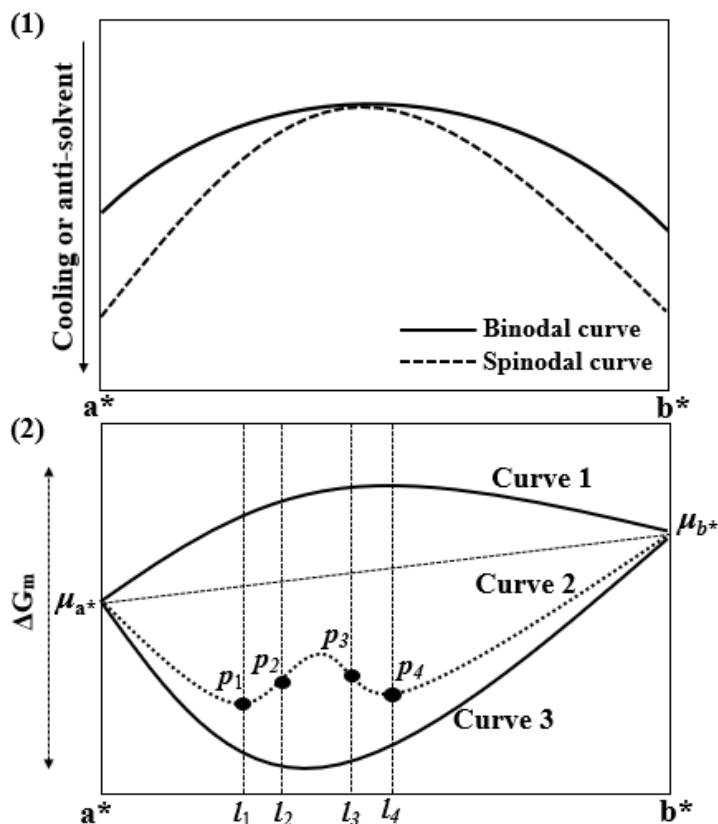
Figure 1-1: (1) phase diagram of a supersaturated solution with oiling out phenomenon, (2) Schematic of Gibbs free energy of mixing components $a*$ and $b*$

The occurrence of oiling out phenomenon usually depends on the model compound, supersaturation, solvent type, viscosity of the solution, temperature etc. The studies in pharmaceutical crystallization aim to avoid oiling out to improve the crystallization performance. Many studies have focused on the optimization of crystallization route e.g. selection of the solvent, temperature, cooling profile as well as thinking about the scale-up performance [4]. There are few papers on the mechanism at molecular level, which is essential to understand the process and control nucleation and growth, and thus the binary phases, and properties of crystal products [5-8].

Gelation during solution crystallization process is much more serious than oiling out that can interrupt the operation directly. Gelation that occurred during a crystallization process referrsd to the formation of semi-flow solid stage phase which can be divided into two types of jellylike phases with high viscosity and gel a phase with 3D microscopic network structure which is usually constructed through crystalline or non-crystalline fibers [9-13].

Actually, the gelation had not been studied in pharmaceutical crystallization process until the reports of pharmaceutical molecules appeared in the literature as gelators in solution [14]. Subsequently, few studies reported the gel transformation of some pharmaceutical molecules to crystals, in which the mechanism at molecular level was tracked through single crystal structure analysis [15-17]. Those studies inspired the follow-up works to investigate the mechanism of gelation to avoid its occurrence during crystallization and screen and optimize transformation conditions from gel or jellylike phase to novel crystal product. This is significant in the production practice as well as in novel product development.

Non-monotonic nucleation discussed in this thesis refers to a non-monotonic trend in the nucleation rate with the stirring speed in solution crystallization. The majority of studies in the literature have noted a monotonic increase in the nucleation rate with increasing the agitation rate [18, 19]. The changing of agitation level directly affects the shear force in the crystallization solution and the following assembly of solute molecules, attrition, and breakage of crystals. The non-monotonic dependence of induction time, primary and secondary nucleation rate on shear rate result in the difficulties in nucleation control and the process scale-up. The mechanism of the non-monotonic relationship and the quantitative tracking of the nucleation rate facilities the study of the non-classical phenomenon and control the whole crystallization process.

Retardation of nucleation refers to a relatively long induction time. Research in this area includes the study of nucleation induction time and various methods used to speed up and control nucleation process that will be discussed in section 1.1.3.

1.1.2. Nucleation and process monitoring

The quantitative investigation of nucleation mechanism and crystallization process relies on the effective monitoring of crystals, especially for the initial nucleation process. Until now, various technologies were developed to track crystallization process in real time including the focused beam reflection measurement (FBRM), laser-based turbidity measurement, ultrasonic velocity measurement, electrical conductivity, and light transmittance measurement, etc. Another technology based on image analysis was

investigated intensively, in the recent studies shown in Table 1-1, because of its advantage of visualization of the crystallization process. There are still several bottlenecks to realize accurate measurement in real time manner such as a high-quality image in a wide range of slurry density, image processing speed, crystal segmentation, transfer application of a well-optimized algorithm to other crystallization systems, etc. In October of 2017, Facebook artificial intelligence research (FAIR) team released a state-of-the-art neural network called Mask R-CNN (Regional Convolutional Neural Networks) which has shown great performance to segment objects in a picture in pixel-wise accuracy and tens of times faster than traditional mathematical algorithms. It provides a great opportunity to introduce the imaging to the crystallization process, which has the potential to move a big step forward for real-time crystallization monitoring.

Table 1-1: Recent studies of image-based crystallization process tracking

#	Hardware	Algorithms
1	Flow cell camera device [20, 21]	Motion Interactive Segmentation [26]
2	Stereo vision imaging system [22, 23]	Edge detection [27, 28]
3	Endoscopy stroboscope [24, 25]	Clustering segmentation
4	Particle vision and measurement (PVM) etc.	Region-based segmentation (threshold, watershed) etc.[29, 30]

1.1.3.   Nucleation-based crystallization process optimization

The study of nucleation mechanism using real-time tracking with non-classical nucleation phenomenon to produce high-quality crystal product in a robust and effective crystallization process, is of prime significance. Researchers realized the importance of control of nucleation on crystal quality and process performance, so that the techniques like the magnetic field, ultrasonic irradiation, microwave, wet milling, etc., were introduced to optimize nucleation [31-34]. In a crystallization process, the nucleation and the crystal growth can be controlled separately. As shown in Figure **1**-**2**, the nucleation step involves the number density and crystal formation followed by crystal growth, agglomeration, attrition etc. A direct nucleation control (DNC) methodology was proposed based on the real-time feedback control of nucleation rate that was estimated by the newly formed particles within detectable size range [35, 36]. Other crystallization process

configurations involved a separating nucleation and crystal growth processes that with fine-tuning the nucleation step including the number density, polymorphism, etc. [37] Various methodologies and different process configurations will be used in this study, for the non-classical nucleation systems to overcome the uncertainties of nucleation.
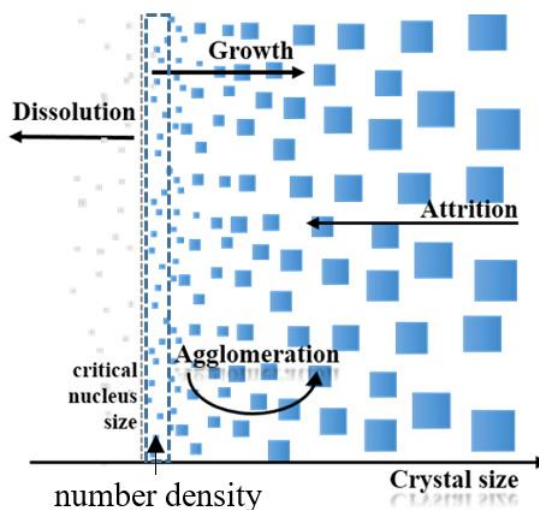
Figure 1-2: Schematic of crystallization process optimization that in nucleation step and crystal growth step, respectively

1.2.   Research Objectives and Approach

The overall objective of this thesis is to produce high-quality crystal product based on the careful study of nucleation mechanism especially for systems with non-classical nucleation phenomenon. The specific objectives are:

- First, study the nucleation mechanism of the crystallization systems that showed non-classical nucleation phenomena.
- Second, find the methodologies to monitor the nucleation onset point as well as the crystal evolutions, in an online fashion.
- Thirdly, produce high-quality crystal products through nucleation process optimization assisted by ultrasonic irradiation, and develop an innovative continuous configuration of a mixed suspension mixed product removal (MSMPR)-tubular crystallizer system.

For the study of the mechanism of non-classical nucleation systems, two levels of scope were considered to track the nucleation phenomena, i.e. a microscale scope and a molecular level. In the microscale scope level, micron dimensional particles were monitored using a

microscope in addition to the in-situ FBRM. In the molecular level which is much more important, the spectroscopy properties were collected using in-situ Raman, Fourier Transform Infrared Spectroscopy (FT-IR) in line and offline system, and the crystal structure was determined using powder X-ray diffraction (PXRD) and single crystal X-ray diffraction (SXRD) data, thermodynamic properties such as melting points, weight loss collected by thermogravimetric analysis (TGA) and differential scanning calorimetry (DSC) measurement. The combined methodology of spectroscopy properties analysis and direct observation of nucleation phenomena enable the study of the nucleation mechanism at the molecular level regarding the intermolecular interactions during nuclei's formation.

The study of nucleation was conducted with the motion-based multiple object tracking (MMOT) model in MATLAB which allows the detection of moving objects in a video stream. It was introduced, for the first time coupled with portable camera probe, for the nucleation monitoring, and was proven to have high accuracy. For the crystallization process monitoring, one of the most popular neural networks, Mask R-CNN, was introduced to process real-time images and extract crystal information to help to analyze crystal evolution. The great success of the Mask R-CNN in other applications like self-driving car, instance segmentation in object detection, etc. inspired us to explore the potentials in microscale field to mine the data in a crystallization process.

Nucleation process optimization was conducted based on the understanding of the non-classical nucleation mechanism. Ultrasonic irradiation was explored to optimize the nucleation of an oiling out system, and seeding method which is widely used in industry was investigated to help to avoid oiling out phenomenon and compare with the ultrasonic irradiation methodology. Apart from imposing an external force on a supersaturated solution, like ultrasonic irradiation, a new crystallizer configuration combining an MSMPR and a tubular crystallizer were proposed with the intention of separating crystal nucleation and growth steps. The MSMPR-tubular system enables the fine tuning of nucleation step producing desired crystal form and number density in the MSMPR stage, followed by the growth process in the tubular stage without detectable agglomeration and breakage.

1.3. Thesis Organization

Chapter 1 is introduction section that gives project background, objectives, research approaches, and organization of the thesis.

There are three main parts of the thesis, the non-classical nucleation mechanism study, nucleation and crystallization process monitoring, and nucleation-based crystallization process optimization. The research scheme corresponding to each chapter is indicated in Figure 1-3.

Study of non-classical nucleation mechanism	**Nucleation and following process monitoring**	**Nucleation-based process optimization**
❖ **Non-monotonic nucleation** Chapter 2 ❖ **Jellylike phase mediated nucleation** Chapter 3	❖ **Motion-based objects detection model,** Chapter 4 ❖ **Mask R-CNN segmentation, classification** Chapter 5	❖ **Ultrasound and seeding assisted optimization** Chapter 6 ❖ **MSMPR-tubular system** Chapter 7

Figure 1-3: Research outline and thesis scheme in chapters

In the first part of this thesis (chapters 2 and 3), efforts were put into the understanding of the mechanism of the formation of intermediate phase as well as the non-monotonic nucleation with the increasing of stirring rate. In chapter 2, a non-classical nucleation rate as a function of the stirring rate was investigated. The induction time was determined at different agitation levels which is an important parameter during process optimization and scaling-up. Two nucleation routes i.e. homogenous nucleation and pre-nucleation cluster formation were proposed depending on the intensity of the stirring rate. A jellylike phase formation was investigated in chapter 3 that transformed to stable crystals and formation of novel solvate crystals in the jellylike phase.

The second part discusses the monitoring of nucleation and the subsequent crystallization process in chapters 3 and 4. The chapter 3 introduces a motion-based multiple objects tracking model used to detect the nucleation onset, which is inspired by the study of nucleation mechanism. The MMOT model coupled with a portable camera probe is

introduced and proven to be a cost-effective technology with high detection accuracy. Chapter 4 extends the novel detection method to the entire crystallization process by introducing the state-of-the-art deep learning neural network, Mask R-CNN. Implementation of the Mask R-CNN is instructive and renders the information extracted from the real-time images, e.g. crystal segmentation, classification, surface area. Comparison between the newly developed methodology and traditional measurement tools is conducted which shows the advantages of deep learning-based tracking in accuracy and efficiency, and cost.

Finally, the third section (chapters 6 and 7) deals with improving the crystal product quality and optimizes the performance of the crystallization process during the oiling out phenomenon. Chapter 6 employs the ultrasonic irradiation in three different frequencies to promote nucleation and narrow down the metastable zone width. Seeding methodology is also included to explore of its effect in preventing the oiling out occurrence. In chapter 7, an MSMPR-tubular system is developed to optimize a crystallization process. In the MSMPR crystallizer, the nucleation step is fine-tuned to generate nuclei/crystals through principal component analysis (PCA) by optimizing the operation parameters. The continuous slurry with optimized seeds is transferred to three coiled tubular crystallizers for crystals growth, and the final crystals, as well as a proposed scale-up scheme, are demonstrated at the end of this chapter.

Chapter 8 summaries the research work and gives research suggestions for the future.

1.4.   References

1. Karthika, S.; Radhakrishnan, T. K.; Kalaichelvi, P. A review of classical and nonclassical nucleation theories. *Cryst. Growth Des.* 2016, 16(11) 6663-6681.

2. Smeets, P. J.; Finney, A. R.; Habraken, W. J.; Nudelman, F.; Friedrich, H.; Laven, J.; De Yoreo, J. J.; Rodger, P. M.; Sommerdijk, N. A. A classical view on nonclassical nucleation. *Proc. Natl. Acad. Sci. U.S.A.* 2017, 114(38) 7882-7890.

3. Deneau, E; Steele, G. An in-line study of oiling out and crystallization. *Org. Process Res. Dev.* 2005, 9(6), 943-950.

4. Veesler, S.; Lafferrère, L.; Garcia, E.; Hoff, C. Phase transitions in supersaturated drug solution. *Org. Process Res. Dev.* 2003, 7(6), 983-989.

5. Bonnett, P.; Carpenter, K.; Dawson, S.; Davey, R. Solution crystallisation via a submerged liquid–liquid phase boundary: oiling out *Chem. Commun.* 2003, 6, 698–699.

6. Lafferrère, L.; Hoff, C.; Veesler, S. In Situ Monitoring of the Impact of Liquid−Liquid Phase Separation on Drug Crystallization by Seeding. *Cryst. Growth Des.* 2004, 4(6), 1175–1180.

7. De Albuquerque, I.; Mazzotti, M. Crystallization process design using thermodynamics to avoid oiling out in a mixture of vanillin and water. *Cryst. Growth Des.* 2014, 14(11), 5617−5625.

8. Lu, J.; Li, Y. P.; Wang, J.; Ren, G. B.; Rohani, S.; Ching, C. B. Crystallization of an active pharmaceutical ingredient that oils out. Sep. *Purif. Technol.* 2012, 96, 1−6.

9. Ouyang, J. B.; Wang, J. K.; Huang, X.; Gao, Y.; Bao, Y.; Wang, Y. L.; Yin, Q. X.; Hao, H. X. Gel formation and phase transformation during the crystallization of Valnemulin Hydrogen Tartrate. *Ind. Eng. Chem. Res.* 2014, 53 (43), 16859−16863.

10. Yin, Y. H.; Gao, Z. G.; Bao, Y.; Hou, B. H.; Hao, H. X.; Liu, D.; Wang, Y. L. Gelation phenomenon during anti-solvent crystallization of cefotaxime sodium. *Ind. Eng. Chem. Res.* 2014, 53, 1286−1292.

11. Cui, J. X.; Shen, Z. H.; Wan, X. H. Study on the gel to crystal transition of a novel sugar-appended gelator. *Langmuir* 2010, 26, 97−103.

12. Xu, Y.; Kang, C. Q.; Chen, Y.; Bian, Z.; Qiu, X. P.; Gao, L. X.; Meng, Q. X. In-situ gel-to-crystal transition and synthesis of metal nanoparticles obtained by fluorination of a cyclic β-amino alcohol gelator. *Chem. Eur. J.* 2012, 18, 16955−16961.

13. Gao, Z.; Li, L.; Bao, Y.; Wang, Z.; Hao, H.;, Yin, Q.; Wang, J. From jellylike phase to crystal: Effects of solvent on self-assembly of cefotaxime sodium. *Ind. Eng. Chem. Res.* 2016, 55(11), 3075-3083.

14. Couffin-Hoarau, A. C.; Motulsky, A.; Delmas, P.; Leroux, J. C. In situ-forming pharmaceutical organogels based on the self-assembly of L-alanine derivatives. *Pharm. Res.* 21.3 (2004): 454-457.

15. Wang, Y.; Tang, L.; Yu, J. Investigation of spontaneous transition from low-molecular-weight hydrogel into macroscopic crystals. *Cryst. Growth Des.* 2008, 8(3), 884-889.

16. Zhu, P.; Yan, X.; Su, Y.; Yang, Y.; Li, J. Solvent-Induced Structural Transition of Self-Assembled Dipeptide: From Organogels to Microcrystals. *Chem. Eur. J.* 2010, 16(10), 3176-3183.

17. Kumar, D. K.; Steed, J. W. Supramolecular gel phase crystallization: orthogonal self-assembly under non-equilibrium conditions. *Chem. Soc. Rev.* 2014, 43(7), 2080-2088.

18. O'Grady, D.; Barrett, M.; Casey, E.; Glennon, B. The effect of mixing on the metastable zone width and nucleation kinetics in the anti-solvent crystallization of benzoic acid. *Chem. Eng. Res. Des.* 2007, 85, 945-952.

19. Liu, J.; Svärd, M. M.; Rasmuson, Å. C. Influence of Agitation and Fluid Shear on Nucleation of m-Hydroxybenzoic Acid Polymorphs. *Cryst. Growth Des.* 2015, 15 (11), 4177-4184.

20. Kempkes, M.; Vetter, T.; Mazzotti, M. Measurement of 3D particle size distributions by stereoscopic imaging. *Chem. Eng. Sci.* 2010, 65(4), 1362-1373.

21. Schorsch, S.; Vetter, T.; Mazzotti, M. Measuring multidimensional particle size distributions during crystallization. *Chem. Eng. Sci.* 2012, 77, 130-142.

22. Wang, X. Z.; Roberts, K. J.; Ma, C. Crystal growth measurement using 2D and 3D imaging and the perspectives for shape control. *Chem. Eng. Sci.* 2008, 65(3), 1173-1184.

23. Zhang, R.; Ma, C. Y.; Liu, J. J.; Zhang, Y.; Liu, Y. J.; Wang, X. Z. Stereo imaging camera model for 3D shape reconstruction of complex crystals and estimation of facet growth kinetics. *Chem. Eng. Sci.* 2017, 160, 171-182.

24. Simon, L. L.; Merz, T.; Dubuis, S.; Lieb, A.; Hungerbuhler, K. In-situ monitoring of pharmaceutical and specialty chemicals crystallization processes using endoscopy–stroboscopy and multivariate image analysis. *Chem. Eng. Res. Des.* 2012, 90(11), 1847-1855.

25. Simon, L. L.; Nagy, Z. K.; Hungerbuhler, K. Endoscopy-based in situ bulk video imaging of batch crystallization processes. *Org. Process Res. Dev.* 2009, 13(6) 1254-1261.

26. Gao, Z.; Zhu, D.; Wu, Y.; Rohani, S.; Gong, J.; Wang, J. Motion-Based Multiple Object Tracking of Ultrasonic-Induced Nucleation: A Case Study of l-Glutamic Acid. *Cryst. Growth Des.* 2017, 17(10), 5007-5011.

27. Huo, Y.; Liu, T.; Liu, H.; Ma, C. Y.; Wang, X. Z. In-situ crystal morphology identification using imaging analysis with application to the L-glutamic acid crystallization. *Chem. Eng. Sci.* 2016, 148, 126-139.

28. Lu, Z. M.; Zhu, F. C.; Gao, X. Y.; Chen, B. C.; Gao, Z. G. In-situ particle segmentation approach based on average background modeling and graph-cut for the monitoring of l-glutamic acid crystallization. *Chemom. Intell. Lab. Syst.* 2018, 17811-17823.

29. Sarkar, D.; Doan, X. T.; Ying, Z.; Srinivasan, R. In situ particle size estimation for crystallization processes by multivariate image analysis. *Chem. Eng. Sci.* 2009, 64(1), 9-19.

30. El Arnaout, T.; Cullen, P. J.; Sullivan, C. A novel backlight fiber optical probe and image algorithms for real time size-shape analysis during crystallization. *Chem. Eng. Sci.* 2016, 149, 42-50.

31. Jiang, S. An Examination of Sonocrystallization Kinetics of L-Glutamic Acid, University of Leeds, 2012.

32. Kacker, R.; Salvador, P. M.; Sturm, G. S.; Stefanidis, G. D.; Lakerveld, R.; Nagy, Z. K.; Kramer, H. J. Microwave assisted direct nucleation control for batch

crystallization: Crystal size control with reduced batch time. *Cryst. Growth Des.* 2015, 16(1), 440-446.

33. Hu, B.; Huang, K.; Zhang, P.; Zeng, X. A.; Han, Z.; Yu, S. Pulsed electric field effects on sucrose nucleation at low supersaturation. *Sugar Tech.* 2015, 17(1), 77-84.

34. Yin, D. C. Protein crystallization in a magnetic field. *Prog. Cryst. Growth Charact. Mater.* 2015, 61(1), 1-26.

35. Bakar, M. R. A.; Nagy, Z. K.; Saleemi, A. N.; Rielly, C. D. The Impact of Direct Nucleation Control on Crystal Size Distribution in Pharmaceutical Crystallization Processes. *Cryst. Growth Des.* 2009, 9, 1378–1384.

36. Yang, Y.; Song, L.; Nagy, Z. Automated Direct Nucleation Control in Continuous Mixed Suspension Mixed Product Removal Cooling Crystallization. *Cryst. Growth Des.* 2015, 15, 5839–5848.

37. Acevedo, D.; Jarmer, D. J.; Burcham, C. L.; Polster, C. S.; Nagy, Z. K. A continuous multi-stage mixed-suspension mixed-product-removal crystallization system with fines dissolution. *Chem. Eng. Res. Des.* 2018, 135, 112-120.

Chapter 2

Self-Induced Nucleation during the Anti-Solvent Crystallization Process of Candesartan Cilexetil

2. Self-Induced Nucleation During the Anti-Solvent Crystallization Process of Candesartan Cilexetil

Abstract

We report that the induction time goes through a maximum with increasing the agitation rate, while the majority of studies in the literature have noted a monotonic increase in the nucleation rate with increasing the agitation rate. Candesartan cilexetil (CC) was studied as the model compound during an anti-solvent crystallization process. A self-induced nucleation mechanism was proposed based on process tracking analysis by using the Focused Beam Reflectance Measurement (FBRM), in-situ Raman spectroscopy and an off-line differential scanning calorimetry (DSC) instrument. The pre-nucleation clusters generated by the instantaneous change of local supersaturation during the addition of anti-solvent were separated and characterized by X-ray powder diffraction (XRPD) and hot-stage microscope. Results indicate the pre-nucleation clusters are an amorphous phase with a lower melting point compared with the crystalline state. The pre-nucleation clusters acted as a nucleation inducer at low agitation level to promote the nucleation. On the contrary, the pre-nucleation clusters dissolved entirely at the high stirring rate before crystal nucleation occurred, which resulted in a maximum in the induction time with the change of stirring speed. In-situ Raman and DSC results combined with the single crystal structure information of acetone solvate show the evolution from pre-nucleation clusters to solvate crystals. This study helps to understand the nucleation mechanism during the anti-solvent crystallization process, especially for the process scale-up with the observed inconsistencies in the nucleation rate with the mixing rate.

2.1. Introduction

Nucleation kinetics affects the process robustness, crystalline product quality, as well as optimization and scale-up of the crystallization process. The classical nucleation theory (CNT) proposed in vapor-liquid systems relates the nucleation kinetics to the supersaturation, temperature, critical size of the nucleus, and surface tension [1,2]. On the basis of the CNT theory, Mitchell and Frawley [3], Xu *et al.* [4], Sangwal [5-7], and Nagy *et al.*[8] correlated the nucleation rate with the metastable zone width (MSZW) measurement, which gave the estimated critical nucleus size and the effect of working volume, cooling

rate, and agitation level on the nucleation rate. Instead of MSZW, through correlating induction time measurement, Xu *et al.* [9], Kulkarni *et al.* [10], and Jiang *et al.* [11], successfully determined the nucleation kinetics using the stochastic nature and probability theory of nucleation. The two-step nucleation theory stemmed from the protein crystallization process and was validated first through the direct dynamic light scattering tracking of the intermediate clusters [12–14]. Kashchiev *et al.* derived the kinetics of the two-step model including the formation of the intermediate clusters followed by crystal nucleation [15]. Recent studies provide direct observation of the existence of the intermediate clusters in more and more systems using advanced instruments, e.g., atomic force microscopy (AFM) and transmission electron microscopy (TEM) [16–18]. Hsieh *et al.* constructed a peptide assembly model based on the two-step nucleation theory and simulated its kinetics with the experimental validation[18]. The distinction between the classical nucleation theory and the two-step nucleation model is based on whether the intermediate clusters exist. Variation of the two-step model in different systems depends on the lifespan of the intermediate clusters which are metastable and can potentially transform into either nucleus or dissolve. The study of the nucleation mechanism including the CNT and the two-step model is usually conducted in a homogeneous phase encountered in a cooling crystallization from a clear solution. In the pharmaceutical industry, anti-solvent crystallization is widely used because of the lower temperature sensitivity of the active pharmaceutical ingredients (APIs) [19, 20]. The addition of an anti-solvent will induce a super high supersaturation in a local region of the bulk solution. Therefore, the location of the feed pipe is selected close to the tip of the stirrer or in the most turbulent region [21]. Otherwise, the sudden increase in the local supersaturation will generate a second phase that is visible as cloudy droplets or particles. Rohani [21] and Tykiyama *et al.* [22] highlighted that poor mixing induces excess primary nucleation and agglomeration in the processing of inorganic compounds. Genck [23] introduced the possibility of the formation of an amorphous phase during the crystallization of an organic compound that oils out or agglomerates in an anti-solvent crystallization process. The oil droplets or the particles with undefined structures tend to clump together and then harden into a jellylike material. The existence of the oily droplets/particles can be explained by the Ostwald's rule of stages that a thermodynamically metastable phase appears first until the most stable phase finally forms [24, 25]. For the APIs, Bao *et al.* [26–29]

and Shi *et al*. [30] reported a series of gelation phenomena that occurred in the anti-solvent crystallization process, suggesting a competition between the crystal nucleation and gelation. [31] The controllable variables that affect the nucleation kinetics include supersaturation, the addition rate of anti-solvent, agitation level, and the operating temperature, etc. Steendam *et al*. [32] studied a series of scale-up criteria and concluded that the shear rate contributed the most significant parameter in the nucleation kinetics. O'Grady *et al*. [33] reported an increasing trend of nucleation rate with agitation rate. Liu *et al*. [34] studied the effect of fluid shear on the primary nucleation of butylparaben, showing the promotion of nucleation with an increase in the shear force and then a hindering effect after a certain value. Nappo *et al*. [35] found a non-monotonic relationship between the nucleation rate and the shear rate. They proposed that beyond a certain level of shear rate, the nucleation process may be hindered, but there is no experimental evidence to confirm this hypothesis. In this study, we propose a self-induced nucleation mechanism for the candesartan cilexetil (CC) anti-solvent crystallization process. The pre-nucleation clusters that are generated by the instantaneous change of supersaturation during the addition of anti-solvent and captured by in-situ Raman, differential scanning calorimetry (DSC) and hot-stage microscopy provided direct evidence for the existence of clusters that lowered the nucleation barrier and enhanced the nucleation rate. The single crystal structure of the acetone solvate of CC was determined for the first time to assist in the understanding of the evolution from the pre-nucleation cluster to the crystal nuclei. Finally, a schematic of the self-induced nucleation mechanism was proposed to understand the non-monotonic tendency of the nucleation rate with the stirring rate during the anti-solvent crystallization process.

2.2. Material and Experimental Methods

2.2.1. Materials

The pharmaceutical model compound CC (CAS: 145040-37-5, Form I) was purchased from Xi'an Sgonek Biological Technology Co., Ltd. (Xi'an, China) with an HPLC purity of better than 99%. The molecular structure of CC is shown in Figure 2-1. Analytical grade acetone (Caledon Laboratories, Georgetown, Ontario) and distilled water were used.
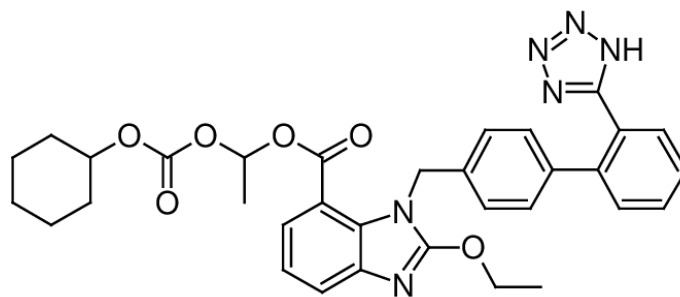
Figure 2-1: Molecular structure of candesartan cilexetil

2.2.2. Experimental Procedures

The experiments were conducted in a 50 mL double-jacketed crystallizer (inner diameter, Φ 39.0 mm, height 43.5 mm) coupled with a magnetic stirrer plate (Cimarec, Thermo Fisher Scientific, USA) and a stirrer bar (Φ 8.6 mm, length 25.5 mm). The saturated solution was prepared in the ratio of CC 3.96 ± 0.01 g, acetone 33.33 ± 0.02 g, and water 2.58 ± 0.01 g. The solution was heated up (FT50, Julabo, Germany) to 30.0 °C and held for 30 min to ensure complete dissolution and then cooled down to 20.0 °C before adding 9.50 ± 0.01 g of water as the anti-solvent at a flow rate of 5 mL/min using a peristaltic pump (Masterflex C/L, IL, USA). The induction time measurements were conducted at different stirring speeds (40, 60, 80, 100, 200, 300, 400, 500, 600, 700 and 800 rpm) to study the nucleation rate. The solubility data of CC in the mixture of acetone and water were used from the literature [36] and validated for consistency. Every experiment was repeated at least three times to ensure the reproducibility of the results. To obtain enough cloudy particles for analysis, an experiment was conducted in a centrifuge tube by rapidly adding the saturated solution and the anti-solvent at the same time, as illustrated in Figure 2-2. The cloudy slurry formed immediately was centrifuged for 10 min in 1550 rpm Centricone (Precision Scientific, IL) and dried for 1 h at room temperature for the powder X-ray diffraction (PXRD) and DSC analyses.
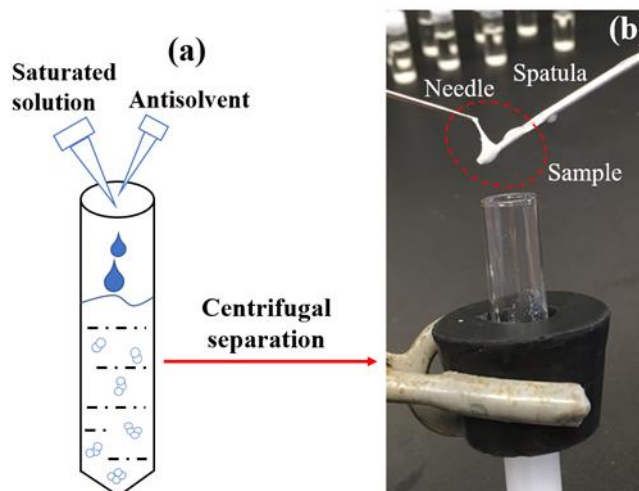
Figure 2-2: Schematic of rapid addition experiment to obtain enough sample for solid-state characterizations, (b) appearance of clumped pre-nucleation clusters after 10 min centrifugal separation

Finally, a series of experiments with no mixing was conducted in twenty 5 mL vials using the same saturated solution and the anti-solvent composition ratio. Three-milliliter saturated solutions were prepared and introduced in each vial followed by the addition of 0.65 mL of water drop by drop using a 200 μL Eppendorf pipet (Hamburg, Germany). The saturated solution and water were held at 20 °C in a water bath, and photographs were taken at room temperature. At every 5 min interval, one of the vials was inverted to check if the crystals have appeared and stuck to the bottom of the vial.

2.2.3. In-Situ Monitoring of the Crystallization Process

In-situ monitoring of the crystallization process was initiated at the time of adding the anti-solvent, until the end of the process. In-situ focused beam reflectance measurement (FBRM) (S400, Mettler Toledo, WA, USA) coupled with iC-FBRM software was used to measure the induction time. The detection limit of the chord length was set at 0.5 μm by using the "fine" measurement model. The counts of the particles with a chord length up to 50 μm were collected every 30s to monitor the nucleation event. In-situ Raman (Kaiser Optical Systems, Inc. Michigan, USA) measurements were recorded using an RXN1-785 Raman spectrometer and analyzed by iC-Raman software. The measurements were conducted using three accumulations of 1 s exposure time, and the interval between two data points was set as short as 5 s in order to capture the pre-nucleation clusters. The experimental setup is shown in Figure 2-3.
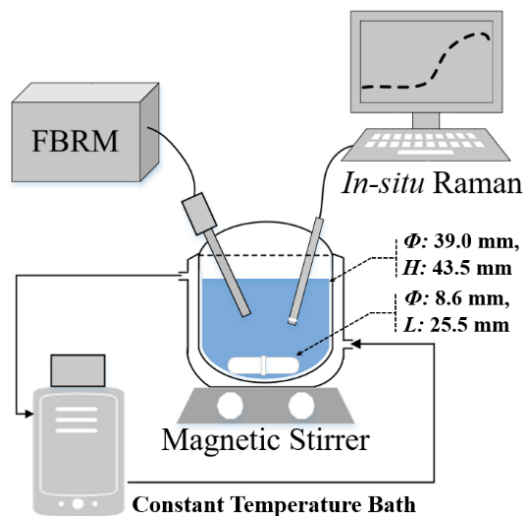
Figure 2-3: Experimental setup combined with the in-situ Raman and FBRM. The sizes of the magnetic stirrer and crystallizer are indicated above

2.2.4.   Solid-State Characterization

The crystallization products at different stirring speeds were collected and dried at room temperature for about 1 h to run PXRD measurements. PXRD was conducted on a powder X-ray diffractometer (Rigaku RINT 2500, Tokyo, Japan) with Cu K radiation ($\lambda = 1.54$ Å) at 40 kV and 50 mA. The scanning speed was 2° per min over a 2θ range of 2° to 40°. The melting points of the samples at different stages were measured using DSC 822e (Mettler Toledo, Switzerland). About 10 mg samples were weighed in a covered aluminum crucible and heated up from 25 to 200 °C with a heating rate of 10 K/min. Nitrogen (100 mL/min) was used to purge the chamber and samples. Hot-stage microscopy experiments were conducted using a combination of a Zeiss Axioskop 40 microscope (Carl Zeiss, Germany) and a hot plate (model LTS350/TMS94, Linkam Scientific Instruments Limited, UK). The heating rate used was 10 K/min.

2.2.5.   Single Crystal Growth

A series of supersaturated solutions with the supersaturation ranging from 1.5 to 8.5 were prepared at 20 °C to screen the suitable conditions for the growth of CC acetone solvate single crystals. For every data point, 50 mL supersaturated solution was generated by adding the anti-solvent to the saturated solution and mixed rapidly in a double-jacketed crystallizer. Four mL of the filtered solution (0.45 μm pore-size membrane filter (Sarstedt, Germany)) were placed in the 5 mL vials (10 vials in one group) in ambient conditions for

3 weeks for slow evaporation. The solution supersaturation was calculated by S = c/c*, where c is the prepared solution concentration, c* is the saturated concentration calculated using the equation: [36]

$$\ln c^* = -6.72455 + 24.39087\, x_1 - 23.90961\, x_1^2 + 13.34692\, x_1^3 - 5.20199\, x_1^4 \quad (2\text{-}1)$$

Where x 1 refers to the initial mole fraction of acetone in the binary solvent (acetone and water). The obtained single crystals were analyzed by single crystal X-ray diffraction at the Western University X-ray facility (Bruker Kappa Axis Apex2, 113.0K).

2.3.   Results and Discussions

2.3.1.   In-Situ Process Monitoring

2.3.1.1. In-Situ FBRM Based Induction Time Measurements

The supersaturation of the solution prepared for induction time measurement was 6.0 for all the experiments. As reported by Cui et al. [37], the acetone solvate can be harvested at a supersaturation below 7.0 during the anti-solvent crystallization process. The acetone solvate is plate-like and was tracked by in- situ FBRM to determine the onset of nucleation. The measurements started at the same time as the beginning of the anti-solvent addition with the stirring speeds ranging from 40 to 800 rpm. Example curves at the stirring speeds 40, 100, 200, and 800 rpm were selected and are shown in Figure 2-4. In the previous studies, the in-situ FBRM has been shown to provide a robust methodology to measure the induction time. During the measurement, the crystals can be detected over a certain size range, and the nucleation event can only be designated beyond a certain value of the crystals counts [32, 38]. In this case, instead of reaching a certain value of the counts, the starting time at which there was a continuous increase in the FBRM counts was designated as the onset of nucleation. This is considered to be more reasonable than selecting a certain value in the counts to designate the onset of nucleation because a continuous increase in the counts can only be induced by a nucleation event. As an example at a stirring rate of 40 rpm, the total counts of crystals under 50 μm was less than 200, while a clear continuous increase in the counts could be seen along with the appearance of the crystals at 8 min. A slight decrease of the counts around 50 min was identified as the agglomeration and the

settling down of crystals happened, which was caused by the ineffective mixing under 40 rpm stirring rate. The fluctuations at the beginning of the measurements are due to the addition of anti-solvent which would generate the clumped and detectable droplets/particles in a short time. With increasing the stirring rate, the crystals' counts increased to several thousand within 1 h. While at 200 rpm, the detected counts were less than both the counts at 100 and 800 rpm, and the induction time was 40 min which is the longest among all the experimental agitation rates.
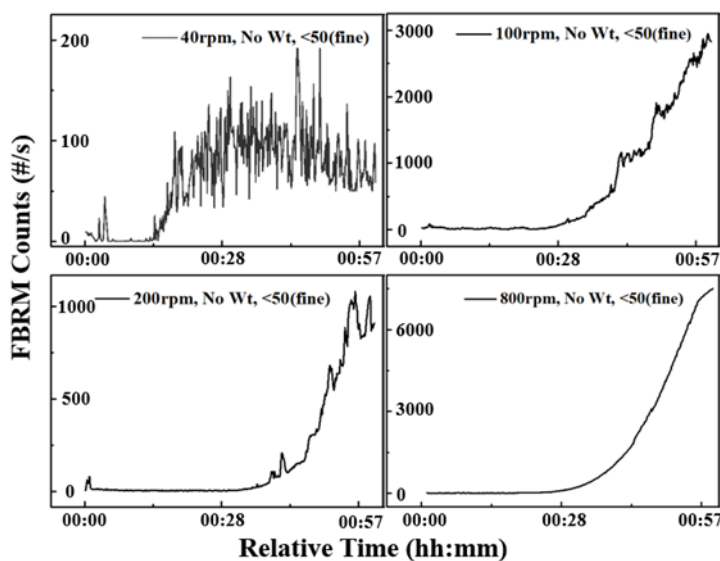
Figure 2-4: FBRM measurements of induction time at different stirring speeds

The measured induction time with the increasing stirring speed is plotted in Figure 2-5. Our results show a maximum in the induction time with the stirrer speed in contrast to a general decreasing trend as shown in Figure 2-5. Figure 2-5 shows the reported results in the literature [33, 34] in which the induction time first reduces and then slightly increases in the second stage. In our measurements, the lowest induction time (the highest nucleation rate) was observed at the lowest stirring rate of 40 rpm. This is attributed to the generation of high local supersaturation at the point of anti-solvent entry. At 200 rpm, the appearance of crystals took about 40 min i.e., five times of the induction time at 40 rpm. The increase in the induction time between 40 and 200 rpm is due to the elimination of high local supersaturation due to the better mixing. The induction time decreased to about 25 min at 800 rpm, which can be explained by the shear-enhanced cluster growth and the coalescence in the range of 200-800 rpm [39, 40]. The cloudy particles were observed by naked eyes at the

time of adding the anti-solvent, and the fluid shear was speculated to contribute to the dissolving of the cloudy particles.
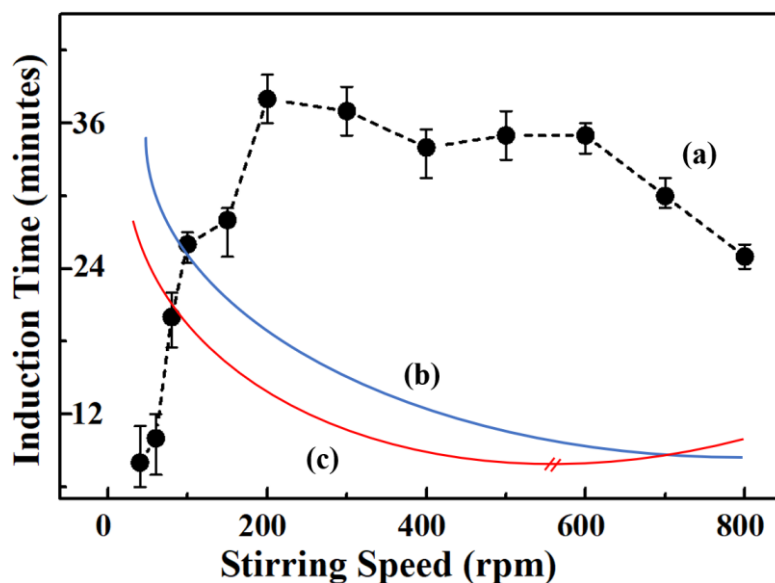
Figure 2-5: (a) Measurements of the induction time of CC during the anti-solvent crystallization process. The dashed line indicates the trend. (b) A general trend of induction time decreasing with agitation level reported in the literature, (c) reported qualitative trend of a slight increase of induction time after a certain level of agitation. Panels (b) and (c) show the qualitative trends reported in the literature

In order to characterize the properties of the cloudy particles, an experiment was performed in a tube (Figure 2-2) by rapidly adding the saturated solution and the anti-solvent at the same time to collect enough samples for the characterization. Instead of vacuum filtration, a centrifuge was used for separation of the particle clusters, as the particles adhered to the filter paper and interrupted the filtration process. The dried particles were characterized as amorphous by PXRD measurement as shown in Figure 2-6 a. According to Ostwald's rule of stages, the instantaneous change in local supersaturation generates an amorphous particles structure without allowing enough time to order the molecules to form a crystal structure.

Following the formation of clusters in the experiments conducted in the crystallizer (Figure 2-3), the acetone solvate crystals of CC appeared at all the stirring speeds as shown in Figure 2-6 b, c. As the stirring speed increasing, the crystallinity of the CC acetone solvate improved as is shown by higher peak intensity in Figure 2-6 c. The acetone solvate crystal

desolvated during the drying process to form II crystals as indicated in Figure 2-6 d. The polymorphic outcome is consistent with the report by Cui *et al*.[37]
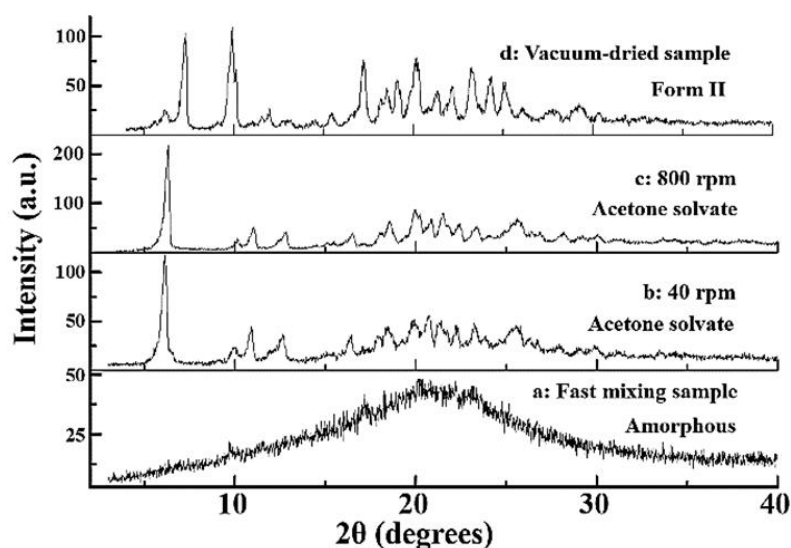
Figure 2-6: PXRD patterns of different candesartan cilexetil polymorphs obtained at different conditions. *a* is amorphous, *b* and *c* are acetone solvate, and *d* is Form II

2.3.1.2.In-situ Raman Process Monitoring

The in-situ Raman spectrometer is an effective instrument to track the solid phase in a crystallization process, e.g., polymorphic transformation [41], gelation, and nucleation [27]. The pre-nucleation clusters created by adding anti-solvent were visible by the naked eyes and detectable by FBRM at the beginning. In-situ Raman spectrometer was used to tracking the characteristic peaks of the cloudy particles and corresponding evolution to final crystals. As shown in Figure 2-7, the characteristic peaks were captured immediately after adding the anti-solvent, and the following addition, corresponding to the pre-nucleation clusters ($694 \ cm^{-1}$) and acetone solvate crystals ($750 \ cm^{-1}$) of CC, respectively. The characteristic peak at $694 \ cm^{-1}$ disappeared and the peak at $750 \ cm^{-1}$ appeared as the crystallization progressed. As shown in Figure 2-8, the Raman shifts at different agitation rates were tracked. For every stirring speed, five moments were selected to indicate the change of the two characteristic peaks at the zeroth, 10th, 20th, 30th, 120th min. The lowest agitation rate at 40 rpm showed the strongest peak of the pre-nucleation clusters at $694 \ cm^{-1}$ which decreased with the increasing of solvate crystal's characteristic peak at $750 \ cm^{-1}$. The ineffective mixing allowed the pre-nucleation clusters to exist in the bulk solution until the occurrence of nucleation. Along with the increase of agitation rate, the time of the

existence of pre-nucleation clusters was shortened. The pre-nucleation clusters could only be captured at the beginning of the process at 100 rpm and disappeared immediately at the stirring speed of 800 rpm. In correlating with the nucleation event, the appearance of the peak at 750 cm^{-1} took a shorter time in the presence of pre-nucleation clusters. The pre-nucleation clusters were tested as amorphous by PXRD as there was not enough time for the ordering of molecules to develop a lattice structure. Therefore, the existence of pre-nucleation clusters in the bulk solution is similar to the second stage of the two-stage nucleation theory, lowering the barrier of nucleation. At higher agitation rates above 200 rpm, the pre-nucleation clusters disappeared before becoming crystalline. The solution went back to a homogeneous state, and the nucleation followed the classical nucleation which was enhanced by increasing agitation level (>200 rpm) as shown in Figure 2-5.
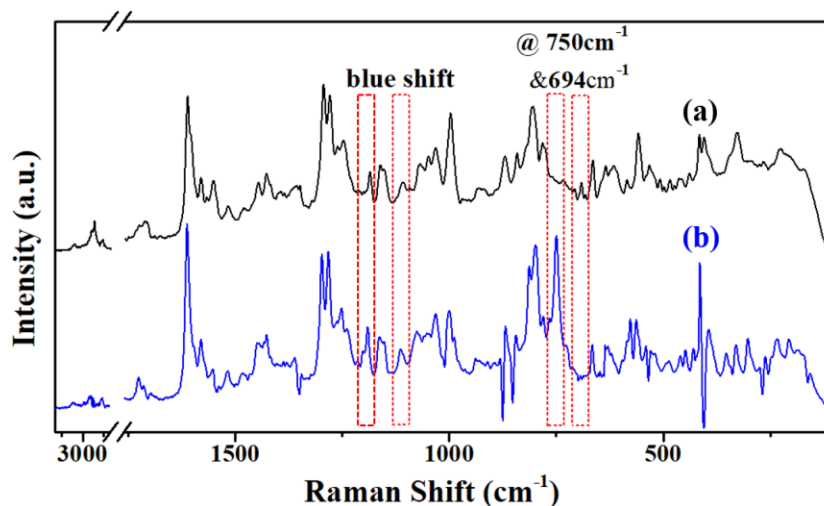
Figure 2-7: Difference of Raman spectrum of pre-nucleation clusters (a) and acetone solvate crystals (b) of candesartan cilexetil during and after the anti-solvent addition process
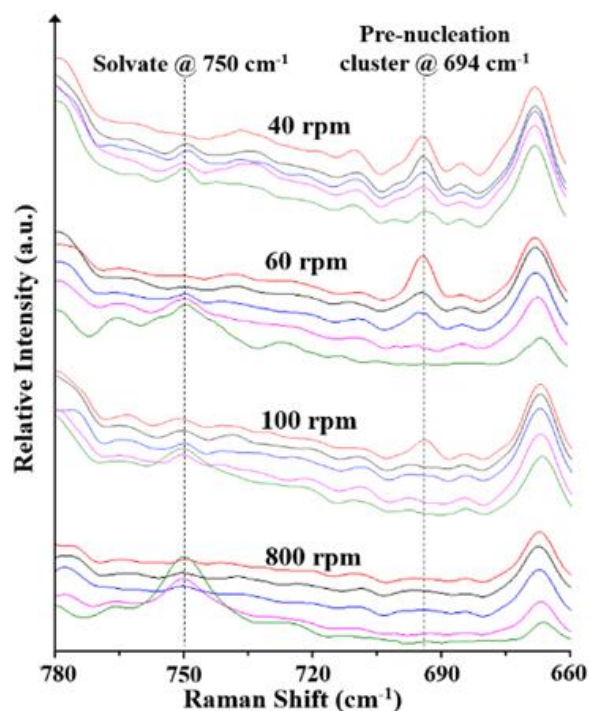
Figure 2-8: In-situ Raman tracking of characteristic peaks of acetone solvate and pre-nucleation clusters of candesartan cilexetil during the anti-solvent crystallization process. For every stirring rate, the spectra correspond to zeroth, 10th, 20th, 30th, 120th min after the addition of the anti-solvent plotted in a descending (top spectrum corresponds to zeroth min) sequence

As indicated in Figure 2-7, the blue shifts from 1187 to 1192 cm^{-1} and 1108 to 1112 cm^{-1} were detected between the pre-nucleation clusters and the acetone solvate. According to the molecular structure as shown in Figure 2-1, the spectrum ranged from 1000 to 1200 cm^{-1} is speculated to be the vibrations of C−O group or the nitrogen atoms located at the tetrazole ring and the 2-ethoxybenzimidazole group [42]. To determine the intermolecular interactions, the single crystal structure of acetone solvate was solved for the first time as indicated in Figure 2-9. The hydrogen bonds N−H···N formed between the donor and acceptor nitrogen atoms that located at the tetrazole ring and the 2-ethoxybenzimidazole group, respectively. Figure 2-9 shows the packing model induced by the hydrogen bonds arranging the CC molecules in a chain that propagates along the b (green) axis. A network with isolated channels is constructed, and the acetone molecules fill the channels without intermolecular hydrogen bonds with the CC molecules (channel solvate). The supersaturation level determined the polymorph of the crystalline products [37], and the

acetone solvate could desolvate to Form II (Figure 2-6 d) and has a melting point at 116.3 °C which would be discussed in the following thermodynamic analysis.
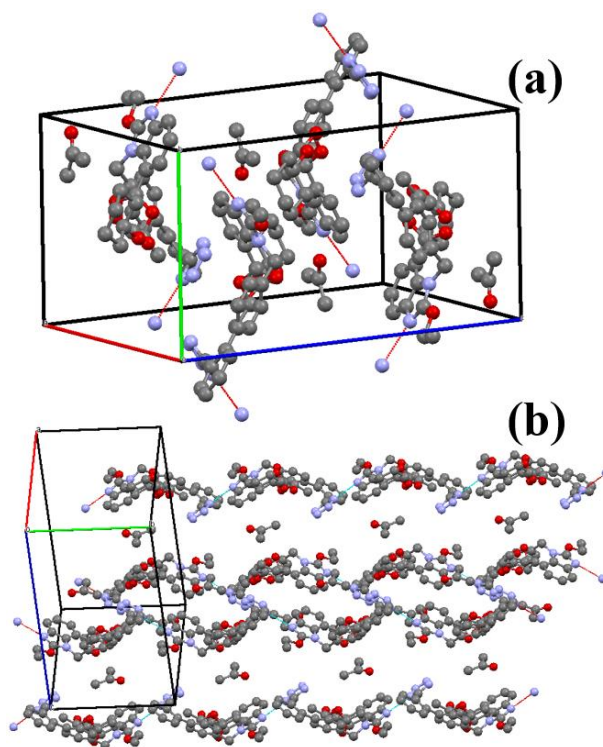
Figure 2-9: (a) Single crystal lattice structure of candesartan cilexetil acetone solvate, (b) molecular packing of candesartan cilexetil acetone solvate. The acetone molecules are embedded between the layers

2.3.2.   Solid-State Characterization

2.3.2.1.DSC Measurements

In Figure 2-2, the sample corresponding to the rapid addition experiment in the tube was separated by a centrifuge. The sample shows elastic and waxy physical characteristics. The sample harvested in the rapid addition experiment was dried and tested by DSC first, as the green curve line shown in Figure 2-10, in which a single endothermic peak was observed at 88.2 °C. As there is, generally, no melting point for an amorphous material, the characteristic peak was suspected to be the desolvation of the clumped pre-nucleation clusters, in which acetone interacted with CC molecules to form inclusive complexes. For the acetone solvate, the melting point was measured at 116.3 °C for both the milled single crystals (blue curve) and the product at 800 rpm (red curve). Cui *et al*. [37] reported the endothermic peak of acetone solvate located at 110.8 °C (5 °C/min) using a punched cover

of the measurement crucible. The difference compared with this study was the heating rate (10 °C/min) as well as the sealed cover of aluminum crucible which was used in our study to prevent the desolvation of acetone solvate. On the basis of the measurements of pre-nucleation clusters and acetone solvate above, the sample under the 40 rpm stirring rate at 30th min was analyzed to be a mixture of pre-nucleation clusters and acetone solvate crystals, which showed dual endothermic peaks (black curve). This verified the coexistence of pre-nucleation clusters and crystalline acetone solvate in the early stage at 40 rpm experiments, which is consistent with the in-situ Raman measurement. Furthermore, a series of DSC tests were conducted on samples conducted at 40 rpm to track the evolution of the ratio of pre-nucleation clusters to crystalline acetone solvate (Figure 2-11). At 15th min for the 40 rpm experiment, a small endothermic peak at 116.3 °C indicated the existence of acetone solvate, while the peak at 88.2 °C corresponds to the pre-nucleation clusters. As the process progressed (20th and 30th min), the ratio of the two endothermic peaks changed in the crystallization process of acetone solvate crystals. Finally, a single melting peak was observed at the same location as the milled single crystals of acetone solvate. The DSC measurement results showed the thermal properties of the pre-nucleation clusters and the acetone solvate confirming their coexistence at a low level of agitation.
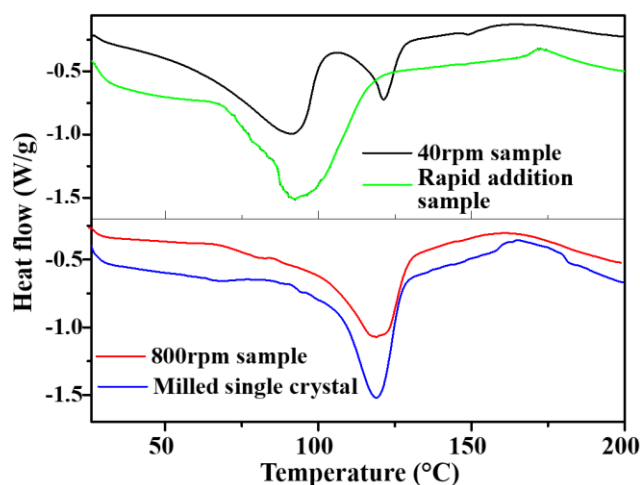
Figure 2-10: DSC measurement of crystallization samples: with the stirring speed at 40 rpm (black) and 800 rpm (red), rapid addition sample (green), and milled single crystals (blue). The samples under 40 and 800 rpm stirring speed were collected at 30 min after the addition of anti-solvent
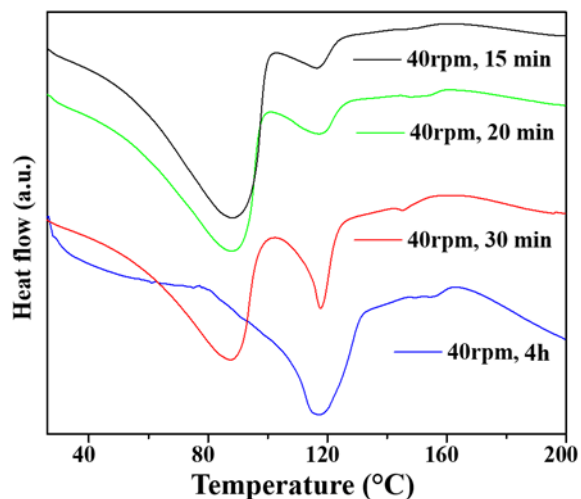
Figure 2-11: DSC measurement tracking of crystallization samples at 40 rpm stirring speed at 15 min (black), 20 min (green), 30 min (red) and 4 h (blue)

2.3.2.2.Hot-stage Microscopy Characterization

As measured above, the cloudy particles that appeared during the addition of anti-solvent had a desolvation peak at 88.2 °C with amorphous properties. Moreover, the in-situ Raman and DSC measurements showed the existence of pre-nucleation clusters during the anti-solvent addition, especially at low levels of agitation. So, the hot-stage microscopy experiments were designed to test the evolution of the sample at 40 rpm stirring rate. As shown in Figure 2-12, the sample at 30th min was heated at a heating rate of 10 °C/min. The pre-nucleation clusters melted before 110 °C, as shown in Figure 2-12, and the plate-like acetone solvate was enclosed inside the melt liquid. Above 150 °C, all the sample melted into a single liquid phase. This methodology provided direct observation of the mixture of the pre-nucleation cluster and the acetone solvate from the dynamic images taken by hot-stage microscopy.
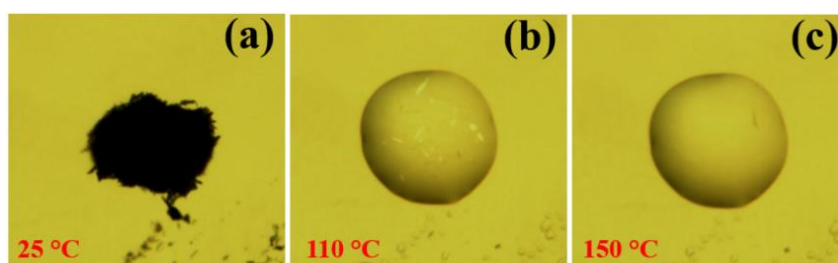
Figure 2-12: Panels (a), (b) and (c) are pictures taken by a hot-stage microscope during heating up of the crystallization sample at 40 rpm stirring speed

2.3.3.   Stationary Experiments

The in-situ monitoring and solid-state characterization at different moments during the evolution of the crystallization process illustrated the existence of pre-nucleation clusters at low agitation levels which lowered the nucleation barrier and enhanced the nucleation rate. A series of stationary experiments was designed to further observe the appearance of pre-nucleation clusters upon anti-solvent addition and the subsequent crystals' formation. As shown in Figure 2-13, the addition of anti-solvent created a localized super high supersaturation that resulted in the formation of cloudy particles labeled by the red ellipse. The visible cloudy particles are clumped pre-nucleation clusters with amorphous undefined structures. The amorphous particles tended to settle down at the bottom of the vial and agglomerated to form a dense phase as highlighted by the red rectangle in Figure 2-13. The dense phase had good flow-ability and showed no adhesion of the dense phase to the bottom of the vials once it was inverted as shown in Figure 2-13 corresponding all inverted vials up to 30 min. Crystals were first observed in the dense phase at the bottom of the vial at 30 min and thereafter (Figure 2-13), which supports the analysis that the pre-nucleation clusters induced nucleation. The experiments were repeated three times confirming good flow-ability of the dense phase before 30 min and the appearance of crystals and sticking at the bottom of the vials inverted after 30 min. Once the crystals appeared at the bottom of the vials, they grew very quickly as indicated in Figure 2-13 at 40th min up to 100 min forming agglomerates to millimeter size which is much larger than crystal size in the experiments with stirring.
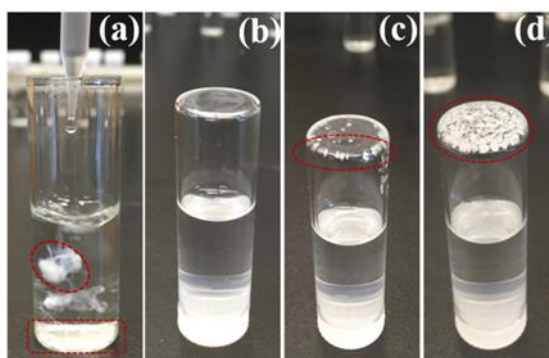
Figure 2-13: Stationary experiments in vials (a) the moment of adding anti-solvent, 0th min, (b-d) appearance of the vials that inverted at 0th min, 30th min and 40th min, respectively

Compared with the stationary experiments carried out in vials, the experiments conducted in the crystallizer with agitation did not allow the cloudy particles to settle down to the bottom of the crystallizer. According to Ostwald's rule of stages, the instantaneous supersaturation would force the solute molecules in the solution to agglomerate into an amorphous, undefined structure which is unstable for both the solution and crystalline state. At a high level of agitation, the large number of cloudy particles created during anti-solvent addition would dissolve entirely as indicated by blue arrows in the schematic of Figure 2-14. In the next step, the clear solution would go through a primary nucleation route for further crystallization process in which the CNT or two-step nucleation may be involved. On the contrary, at low agitation rates, the cloudy particles could exist for a more extended period to act as an inducer for crystal nucleation. As the route in the red arrows in Figure 2-14 shows, the pre-nucleation clusters lowered the nucleation barrier and shortened the induction time.

Different from the concept of "pre-nucleation cluster" that was proposed specifically for a homogeneous solution [43, 44], the anti-solvent crystallization process generated instantly a second phase (pre-nucleation clusters) which is different from the structure of the final crystalline state. Interestingly, Gebauer *et al.* [44] posed an open question at the end of their review "Are PNC (pre-nucleation cluster)-like pathways relevant in heterogeneous nucleation?" which has already been discussed in detail in this study.
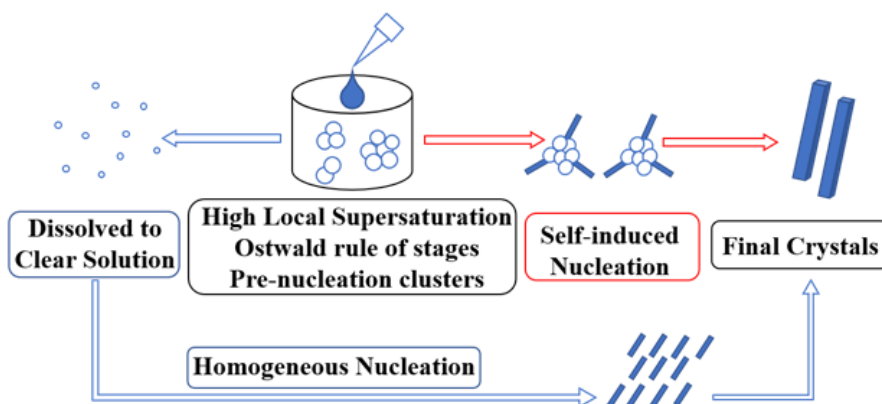
Figure 2-14: Schematic of the mechanism of self-induced nucleation during the anti-solvent crystallization process of candesartan cilexetil

2.4.   Conclusions

A non-monotonic dependence of induction time on the level of agitation was reported in the anti-solvent crystallization process of CC. The self-induced pre-nucleation clusters mechanism was proposed based on the analysis of in-situ process tracking as well as the solid-state characterization in different stages. The pre-nucleation clusters were monitored during the crystallization process and identified as an amorphous unstable phase. The addition of anti-solvent would result in an instantaneous change of supersaturation in a localized region, in which the solute molecules are forced out to form a metastable state that does not have sufficient time to develop a crystal structure. Whether the pre-nucleation clusters act as a nucleation inducer depends on its existence period in the bulk solution. At a high agitation level, the anti-solvent addition induced cloudy particles that dissolved before the occurrence of nucleation. Therefore, the solution eventually would go through homogeneous nucleation pathway. Inversely, at low levels of agitation, the cloudy particles would act as the nucleation inducer. This mechanism may help to explain the abnormal phenomenon during the scaling-up of the anti-solvent crystallization process. It is worth noting that in the conventional crystallization process, the anti-solvent addition rate is usually controlled to ensure the growth of the crystal. While in the measurement of induction time, the anti-solvent is added in a relatively quick manner in order to achieve a certain supersaturation level, so that the localized supersaturation is very high that may promote the formation of the unstable phase.

Accession Codes CCDC 1870085 contains the supplementary crystallographic data for this paper. These data can be obtained free of charge via www.ccdc.cam.ac.uk/data_request/cif, or by emailing data_request@ccdc.cam.ac.uk, or by contacting The Cambridge Crystallographic Data Centre, 12 Union Road, Cambridge CB2 1EZ, UK; fax: +44 1223 336033.

2.5. References

1. Volmer, M.; Weber, A. Keimbildung in übersättigten Gebilden. Z. *Phys. Chem.* 1926, 119, 277–301.

2. Frenkel, J. A General Theory of Heterophase Fluctuations and Pretransition Phenomena. *J. Chem. Phys.* 1939, 7, 538–547.

3. Mitchell, N. A.; Frawley, P. J. Nucleation kinetics of paracetamol−ethanol solutions from metastable zone widths. *J. Cryst. Growth* 2010, 312, 2740–2746.

4. Xu, S.; Wang, J.; Zhang, K.; Wu, S.; Liu, S.; Li, K.; Yu, B.; Gong, J. Nucleation behavior of eszopiclone-butyl acetate solutions from metastable zone widths. *Chem. Eng. Sci.* 2016, 155, 248–257.

5. Sangwal, K. Novel approach to analyze metastable zone width determined by the polythermal method: physical interpretation of various parameters. *Cryst. Growth Des.* 2009, 9, 942–950.

6. Sangwal, K. Recent developments in understanding of the metastable zone width of different solute-solvent systems. *J. Cryst. Growth* 2011, 318, 103–109.

7. Sangwal, K. Some features of metastable zone width of various systems determined by polythermal method. *CrystEngComm* 2011, 13, 489–501.

8. Nagy, Z. K.; Fujiwara, M.; Woo, X. Y.; Braatz, R. D. Determination of the Kinetic Parameters for the Crystallization of Paracetamol from Water Using Metastable Zone Width Experiments. *Ind. Eng. Chem. Res.* 2008, 47, 1245–1252.

9. Xu, S.; Chen, Y.; Gong, J.; Wang, J. Interplay between Kinetics and Thermodynamics on the Probability Nucleation Rate of a Urea−Water Crystallization System. *Cryst. Growth Des.* 2018, 18, 2305–2315.

10. Kulkarni, S. A.; Kadam, S. S.; Meekes, H.; Stankiewicz, A. I.; ter Horst, J. H. Crystal Nucleation Kinetics from Induction Times and Metastable Zone Widths. *Cryst. Growth Des.* 2013, 13, 2435–2440.

11. Jiang, S.; ter Horst, J. H. Crystal nucleation rates from probability distributions of induction times. *Cryst. Growth Des.* 2011, 11, 256–261.

12. Maes, D.; Vorontsova, M. A.; Potenza, M. A. C.; Sanvito, T.; Sleutel, M.; Giglio, M.; Vekilov, P. G. Do protein crystals nucleate within dense liquid clusters?. *Acta Crystallogr., Sect. F: Struct. Biol. Commun.* 2015, 71, 815–822.

13. Erdemir, D.; Lee, A. Y.; Myerson, A. S. Nucleation of crystals from solution: classical and two-step models. *Acc. Chem. Res.*, 2009, 42, 621-629.

14. Gliko, O.; Neumaier, N.; Pan, W.; Haase, I.; Fischer, M.; Bacher, A.; Weinkauf, S.; Vekilov, P. G. A Metastable Prerequisite for the Growth of Lumazine Synthase Crystals. *J. Am. Chem. Soc.*, 2005, 127, 3433–3438.

15. Kashchiev, D.; Vekilov, P. G.; Kolomeisky, A. B. Kinetics of two-step nucleation of crystals. *J. Chem. Phys.*, 2005, 122, 244706.

16. Schubert, R.; Meyer, A.; Baitan, D.; Dierks, K.; Perbandt, M.; Betzel, C. Real-time observation of protein dense liquid cluster evolution during nucleation in protein crystallization. *Cryst. Growth Des.* 2017, 17, 954–958.

17. Sleutel, M.; Van Driessche, A. E. Nucleation of protein crystals−a nanoscopic perspective. *Nanoscale*, 2018, 10, 12256-12267.

18. Hsieh, M. C.; Lynn, D. G.; Grover, M. A. Kinetic model for two-step nucleation of peptide assembly. *J. Phys. Chem. B*, 2017, 121, 7401–7411.

19. Nowee, S. M.; Abbas, A.; Romagnoli, J. A. Antisolvent crystallization: Model identification, experimental validation and dynamic simulation. *Chem. Eng. Sci.*, 2008, 63, 5457-5467.

20. Zhou, G. X.; Fujiwara, M.; Woo, X. Y.; Rusli, E.; Tung, H. H.; Starbuck, C.; Davidson, O.; Ge, Z.; Braatz, R. D. Direct design of pharmaceutical anti-solvent crystallization through concentration control. *Cryst. Growth Des.*, 2006, 6, 892–898.

21. Rohani, S.; Chapter 10. Crystallization Technology Handbook, second edition, Marcel Dekker Inc., New York, 2001, 475-512.

22. Takiyama, H.; Otsuhata, T.; Matsuoka, M. Morphology of NaCl Crystals in Drowning-Out Precipitation Operation. Chem. Eng. Res. Des., 1998, 76, 809-814.

23. Genck, W. Make the most of antisolvent crystallization. *Chemical Processing*. 2010 Nov 8. https://www.chemicalprocessing.com/articles/2010/210.

24. Levin, A.; Mason, T. O.; Adler-Abramovich, L.; Buell, A. K.; Meisl, G.; Galvagnion, C.; Bram, Y.; Stratford, S. A.; Dobson, C. M.; Knowles, T. P.; Gazit, E. Ostwald's rule of stages governs structural transitions and morphology of dipeptide supramolecular polymers. *Nat. Commun.*, 2014, 5: 5219.

25. Chung, S. Y.; Kim, Y. M.; Kim, J. G.; Kim, Y. J. Multiphase transformation and Ostwald's rule of stages during crystallization of a metal phosphate. *Nat. Phys.*, 2009, 5, 68-73.

26. Yin, Y.; Gao, Z.; Bao, Y.; Hou, B.; Hao, H.; Liu, D.; Wang, Y. Gelation phenomenon during anti-solvent crystallization of cefotaxime sodium. *Ind. Eng. Chem. Res.*, 2014, 53, 1286-1292.

27. Gao, Z.; Li, L.; Bao, Y.; Wang, Z.; Hao, H.; Yin, Q.; Wang, J. From jellylike phase to crystal: Effects of solvent on self-assembly of cefotaxime sodium. *Ind. Eng. Chem. Res.*, 2016, 55, 3075-3083.

28. Ouyang, J.; Wang, J.; Huang, X.; Gao, Y.; Bao, Y.; Wang, Y.; Yin, Q.; Hao, H. *Ind. Eng. Chem. Res.*, 2014, 53, 16859-16863.

29. Su, X.; Gao, Z.; Bao, Y.; Guan, M.; Rohani, S.; Yin, Q.; Hao, H.; Xie, C.; Wang, J. Gelation Mechanism of Erythromycin Ethylsuccinate During Crystallization. *Trans. Tianjin Univ.*, 2018, https://doi.org/10.1007/s12209-018-0163-5.

30. Shi, Z.; Hao, L.; Zhang, M.; Dang, L.; Wei, H. Gel formation and transformation of Moxidectin during the anti-solvent crystallization. *J. Cryst. Growth*, 2017, 469, 8-12.

31. Kapoor, I.; Schon, E. M.; Bachl, J.; Kuhbeck, D.; Cativiela, C.; Saha, S.; Banerjee, R.; Roelens, S.; Marrero-Tellado, J. J.; Diaz, D. D. Competition between gelation and crystallisation of a peculiar multicomponent liquid system based on ammonium salts. *Soft Matter*, 2012, 8, 3446−3456.

32. Steendam, R. R. E.; Keshavarz, L.; Blijlevens, M. A. R.; de Souza, B.; Croker, D. M.; Frawley, P. J. Effects of Scale-Up on the Mechanism and Kinetics of Crystal Nucleation. *Cryst. Growth Des.*, 2018, 18, 5547–5555.

33. O'Grady, D.; Barrett, M.; Casey, E.; Glennon, B. The effect of mixing on the metastable zone width and nucleation kinetics in the anti-solvent crystallization of benzoic acid. *Chem. Eng. Res. Des.*, 2007, 85, 945-952.

34. Liu, J.; Svärd, M. M.; Rasmuson, Å. C. Influence of Agitation and Fluid Shear on Nucleation of m-Hydroxybenzoic Acid Polymorphs. *Cryst. Growth Des.*, 2015, 15, 4177-4184.

35. Nappo, V.; Sullivan, R.; Davey, R.; Kuhn, S.; Gavriilidis, A.; Mazzei, L. Effect of shear rate on primary nucleation of para-amino benzoic acid in solution under different fluid dynamic conditions. *Chem. Eng. Res. Des.*, 2018, 136, 48-56.

36. Cui, P.; Yin, Q.; Gong, J. Solubility of candesartan cilexetil in different solvents at various temperatures. *J. Chem. Eng. Data*, 2011, 56, 658–660.

37. Cui, P.; Yin, Q.; Guo, Y.; Gong, J. Polymorphic Crystallization and Transformation of Candesartan Cilexetil. *Ind. Eng. Chem. Res.*, 2012, 51, 12910–12916.\

38. Gao, Z.; Altimimi, F.; Gong, J.; Bao, Y.; Wang, J.; Rohani, S. Ultrasonic Irradiation and Seeding to Prevent Metastable Liquid-Liquid Phase Separation and Intensify Crystallization. *Cryst. Growth Des.*, 2018, 18, 2628–2635.

39. Allen, R. J.; Valeriani, C.; Tănase-Nicola, S.; ten Wolde, P. R.; Frenkel, D. Homogeneous nucleation under shear in a two-dimensional Ising model: Cluster growth, coalescence, and breakup. *J. Chem. Phys.*, 2008, 129, 134704.

40. Winter, D.; Virnau, P.; Horbach, H.; Binder, K. Finite-size scaling analysis of the anisotropic critical behavior of the two-dimensional Ising model under shear. EPL (Europhysics Letters), 2010, 91, 60002.

41. Schöll, J.; Bonalumi, D.; Vicum, L.; Mazzotti, M.; Müller, M. In-Situ Monitoring and Modeling of the Solvent-Mediated Polymorphic Transformation of l-Glutamic Acid. *Cryst. Growth Des.*, 2006, 6, 881-891.

42. Socrates, G. Infrared and Raman characteristic group frequencies: Tables and Charts, 3rd edition, John Wiley & Sons, New York, 2004.

43. Davey, R. J.; Schroeder, S. L.; ter Horst, J. H. Nucleation of organic crystals-a molecular perspective. *Angew. Chem. Int. Ed.*, 2013, 52, 2166-2179.

44. Gebauer, D.; Kellermeier, M.; Gale, J. D.; Bergström, L.; Cölfen, H. Pre-nucleation clusters as solute precursors in crystallization. *Chem. Soc. Rev.*, 2014, 43, 2348-2371.

Chapter 3

From Jellylike Phase to Crystal: Effects of Solvent on Nucleation of Cefotaxime Sodium

3. From Jellylike Phase to Crystal: Effects of Solvent on Nucleation of Cefotaxime Sodium

Abstract

Jellylike phase (JLP) is usually harmful to the process of crystallization. The special state of cefotaxime sodium (CTX) jellylike phase and its spontaneous transition to crystals are investigated in this paper. The crystals transformed from JLPs containing different solvents exhibit distinct habits and forms. The solvent used in JLP formation and crystallization was very important. The results show that the polarity and hydrogen bonding ability of the solvent plays a decisive role in the JLP formation and its crystallization. Combined with Fourier transform infrared spectra, in-situ Raman spectroscopy monitoring experiment indicates that the orientational hydrogen bonding between the solvent and CTX molecule facilitates the construction of the CTX crystal structure. JLP crystallization offers a new way for novel polymorph development and crystal habit modification, especially for drugs that are difficult to crystallize from solution.

3.1.   Introduction

Solution crystallization is a common method used to prepare drug crystals. Many clinical drugs are amphiphilic or hydrophobic and tend to self-assemble or aggregate in aqueous or non-aqueous environments [1]. The difference in intermolecular interaction strength will lead to different self-assembly forms, such as gel, weak gel, or jellylike phase (JLP), during the crystallization process. JLP, which is similar to oiling out or liquid-liquid phase separation (LLPS) to some extent [2–5], is considered a more severe problem that leads to the failure of crystallization.

In fact, gelation, oiling out, and crystallization are all driven by supersaturation. Because of dynamic arrest, solvent and drug molecules are trapped in a JLP or gel state [6]. Gel and JLP are unstable systems in which there is a balance between drug molecule aggregating forces and solubilizing solvent-drug molecule interaction [7, 8]. They tend to transform into crystals to achieve a thermodynamically stable state [9–12]. During the transition process, the weak interactions between solvent and drug molecules will be reorganized to promote 3D condensed lattice packing. Some of these interactions include dipole-dipole, electrostatic force, π−π stacking, and hydrogen bonding. There are several typical cases focused on the

gel-to-crystal transition mechanism. For hydrogels made up of neutral bile acid derivatives, Terech et al.[10] discovered that it was the spherulitic microdomains that were acting as seeds for a slow crystallization and resulted in the complete phase separation. Smith et al.[13] found individual nanofibers in the gel crystalline material. Cui et al.[14] suggested the molecular sheets of sugar-appended gelator insert into each other with a glide movement that causes the collapse of the gel and translates into a needlelike crystal. Houton et al.[15] pointed out that the molecular packing in the dipeptide hydrogel is one-dimensional, and they would reorganize to align multiple axes, allowing 3D growth. The participation of solvent in the construction of crystals during the transition process has been verified. Zhu et al.[16] illuminated that cosolvent with higher polarity might form strong hydrogen bonds with gelators and thus promote the isotropic gelators to aggregate into the crystal structure. A delicate experiment designed by Xu et al.[17] indicated that through diffusion into the gel phase, the non-gelled solvent that o-xylene repairs the defects of the molecular packing in the gel and facilitates the evolution of molecular self-assembly from low-order to high-order. Braga et al.[18] found that the form of the crystal transformed from gel depended on the kind of gelling solvent. There are few reports about JLP transition to crystals, although recently JLP is found increasingly in the pharmaceutical field. This is probably due to JLP being undesirable in industrial crystallization, and most research is focused on how to avoid it [19–22]. In fact, some outstanding features of JLP are beneficial to drug crystal preparation. For instance, the mass transfer rate in JLP is slow [23], which results in a retardation effect on crystallization and favors formation of large and perfect crystals. In addition, the supersaturation in JLP is high and changes slowly, which is favorable for control of crystal form. Therefore, JLP crystallization offers a new way for novel polymorph development and crystal habit modification, especially for drugs that are difficult to crystallize. In this study, we report a JLP-to-crystal transition phenomenon of CTX (Figure **3**-**1**), a typical drug that is apt to form JLP during solution crystallization. Targeted experiments are designed to study the effects of solvent on JLP formation and crystal formation. The results show that the polarity of solvents is crucial to JLP formation and that the hydrogen bonding ability of solvents is an important factor in the formation of CTX crystal. In the JLP-to-crystal transition process, solvent molecules act as a bridge through hydrogen bonding to connect CTX molecules into a 3D periodic structure.
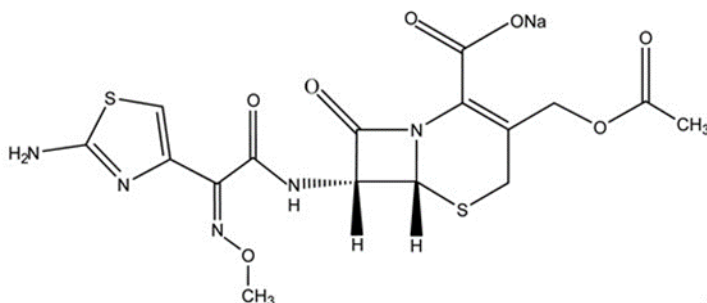
Figure 3-1: Chemical structure of cefotaxime sodium

3.2. Experimental Section

3.2.1. Materials.

Cefotaxime acid (purity > 98.5%) was supplied by Huabei Pharmaceutical Co., Ltd., of China. CTX standard sample (high-performance liquid chromatography (HPLC)-purity, >99.5%) was purchased from Aladdin Industrial Corporation. Sodium acetate and all the organic solvents (analytical-reagent-grade) were purchased from Tianjin Jiangtian Chemical Technology Co., Ltd., of China and used without further purification. Deionized water was purchased from Tianjin QingYuanquan purified water Co., Ltd., of China.

3.2.2. JLP Preparation and Crystallization

3.2.2.1.Anti-solvent Method.

At 10.2 ± 0.2 °C (controlled by a thermostatic water-circulator bath 501 A with an inherent error of ±0.1 °C, Shanghai Laboratory Instrument Works, China), the sodium acetate was dissolved completely in a mixture of deionized water (12.0 ± 0.2 mL, measured using a graduated cylinder with an inherent error of ±0.1 mL) and isopropanol (IPA, 23.2 ± 0.3 mL, inherent error ±0.1 mL). Cefotaxime acid powder (10.06 ± 0.02 g, weighed using a balance with an inherent error of ±0.01 g) was added, and the suspension was gently stirred until a clear solution was formed. Filtration through double filter papers (pore size 30-50 μm) under vacuum was used to prepare the CTX solution. The solution is transparent, light-yellow, and does not contain any visible solid particles. Then, IPA (70.0 ± 0.3 mL, measured using a graduated cylinder with an inherent error of ±0.2 mL) was added into the CTX solution at a constant rate of 1.05 ± 0.03 mL/min using a peristaltic pump (Model BT100-1F, inherent error ±0.01 mL/min, Baoding Longer, China). With the addition of

IPA, the solution became cloudy, and precipitates occurred and gradually aggregated. About 10 min later, the viscous aggregates adhered to the bottom of the container and formed the JLP (named J1). For the convenience of observation, J1 and part of the supernatant were placed in a glass screw-capped vial (10 cm length and 1 cm diameter, 1 mm wall thickness) at 20.0 ± 0.3 °C (controlled by the thermostatic water-circulator bath 501 A with an inherent error of ±0.1 °C) for JLP crystallization experiments. When the JLP-to-crystal transition finished, the crystals (named C1) were separated by filtration, washed with IPA, and dried at 40.0 ± 0.5 °C (inherent error ±0.1 °C) in a vacuum oven until a constant weight was achieved. The anti-solvent experiment was conducted at least six times.

3.2.2.2. Cooling Method.

CTX solution was prepared as described above using a 2:1 mixture of N−N-dimethylformamide (DMF) and ethyl acetate (EA), and the concentration of CTX was 0.132 ± 0.001 g mL^{-1}. The uncertainty of the concentration came from the uncertainties of the solvent volume and the weight of CTX. The propagated uncertainty u(c) was calculated by the following equation:

$$u(c) = \frac{x_1}{x_2} \sqrt{\left(\frac{u(x_1)}{x_1}\right)^2 + \left(\frac{u(x_2)}{x_2}\right)^2} \qquad (3\text{-}1)$$

Where x_1 and $u(x_1)$ are the weight of CTX and its uncertainty, respectively, and x_2 and $u(x_2)$ are the solvent volume and its uncertainty, respectively. The CTX solution was then sealed in a test tube and placed statically at −20.05 ± 0.04 °C controlled by a thermostatic oil-circulator bath (CF41, inherent error ±0.02 °C, Julabo, Germany). About 8 days later, a JLP formed (named J2) and adhered to the bottom of the tube. The JLP-to-crystal transition experiment was conducted at the same temperature. The crystals formed (C2) and then were separated by filtration, washed with EA and kept at -20.05 ± 0.04 °C. The cooling experiment was conducted at least six times.

3.2.2.2.Adsorption Method.

CTX amorphous powder was placed in a glass vial at 35.0 ± 0.8 °C and (85 ± 4)% relative humidity (RH) controlled by constant temperature and humidity chamber LHS-80HC-II

(inherent errors of temperature and RH are ±0.5 °C and ±3%, respectively, Shanghai Yiheng Instruments Co., Ltd., China). About 2 h later, the JLP (named J3) formed. The JLP-to-crystal transition was continued at the same conditions. When finished, the crystals (named C3) were dried at 40.4 ± 0.6 °C (inherent error ±0.1 °C) under vacuum. Different temperature and saturated solvent atmosphere were designed for JLP formation and crystallization research. Here, the CTX amorphous powder was obtained through the addition of CTX solution to a 20-fold greater volume of EA, filtration of the suspension, and then freeze-drying (Labconco, Free Zone, 2.5 L, USA) the products. The CTX solution was prepared as described above using DMF and EA as mixed solvents (VDMF/VEA = 2:1) and the concentration of CTX was 0.203 ± 0.001 g mL^{-1}. The adsorption experiment was performed at least three times with similar results.

3.2.3. Monitoring the JLP-to-Crystal Transition Process

3.2.3.1.X-ray Powder Diffraction

The nucleation and crystal growth during the J1-to-C1 transition process were tracked offline by an X-ray powder diffraction (XRPD) instrument (Rigaku D/MAX-2500, Rigaku, Japan). The XRPD data of the experimental samples were collected under the following conditions: scan speed, 8° min^{-1}; step size, 0.02°; scan range, 2−50 °; resolution, 0.01°; Cu Kα radiation, λ = 1.5406 Å. The uncertainty of the two theta value of the characteristic peak was 0.01°, which was evaluated according to the following equation: [24]

$$u = \frac{r_d}{\sqrt{3}} \tag{3-2}$$

Where u and r$_d$ are the uncertainty of the measurement and the resolution of the instrument, respectively.

3.2.3.2.Polarized Light Microscopy

To capture the emergence of the nuclei and photograph the crystals formed in the transition process, a hot-stage microscopy system was used to in-situ monitor the J1-to-C1 transition process. J1 was placed in the hot stage (LTS350, Linkam Scientific Instrument, Ltd., U.K.) in which the temperature was controlled at 20.0 ± 0.2 °C (inherent error ±0.1 °C). Images were acquired by polarized light microscopy (PLM) (BX51 with a polarizer filter, Olympus Optical Co. Ltd., Japan).

3.2.3.3.Raman Spectra

To reveal the structure change at the molecular level during the transition process, Raman spectrometer (Raman RXN2, Kaiser Optical Systems Inc., USA) was used to in-situ track the J1-to-C1 transition process. J1 was placed in a 30 mL jacketed glass crystallizer at 20.2 ± 0.2 °C (controlled by the thermostatic water-circulator bath 501 A with an inherent error of ±0.1 °C), and the Raman probe was immersed into J1. The spectral wavelength is 785 nm. The Raman shift data were collected at intervals of 30 s using the exposure time of 5 s with six accumulations and were recorded over a range of 200-1900 cm^{-1} with a resolution of 1 cm^{-1}. The uncertainty of the Raman shift of the characteristic peak was 1 cm^{-1}, which was evaluated according to equation 3-2. The monitoring experiment was performed at least six times with the same trend.

3.2.4.　Characterization

3.2.4.1.Thermogravimetric Analysis

Thermogravimetric analysis (TGA) of crystals was performed in a Mettler-Toledo TGA/DSC. (The inherent errors of temperature and weight are ±0.01 °C and ±0.001 mg, respectively.) Data were obtained from 22 to 400 °C at a constant heating rate of 10 °C/min under a dynamic nitrogen atmosphere (flow rate = 20 mL min^{-1}).

3.2.4.2.Karl Fischer Titration

The water content of the crystals was measured by volumetric Karl Fischer (KF) titration (V20/V30, Mettler-Toledo, inherent error ±0.01 mg).

3.2.4.3.Fourier Transform Infrared Spectra.

Fourier transform infrared spectra (FT-IR) spectra of crystals were recorded on a Bruker TENSOR 27 FT-IR spectrometer. The sample was ground together with KBr (anhydrous) using mortar pestle, and the range of the wavenumber was 4000-400 cm^{-1} with resolution 2 cm^{-1}. The uncertainty of the wavenumber of the characteristic peak evaluated according to equation 2-2 was 2 cm^{-1}.

3.2.4.4.Scanning Electron Microscopy.

Scanning electron microscopy (SEM) pictures of amorphous powder were taken by a Hitachi TM3000. The sample was ground to loose powder and coated with a gold layer (200-400 Å in thickness) using a magnetron sputter machine MPS-1S (Vacuum Device Inc.).

3.2.4.5.High-Performance Liquid Chromatography.

The solvent in the CTX solvate was determined on an Agilent 1200 with the Agilent C18 (250 mm × 4.6 mm, 5 μm). A water/methanol mixture (Vw/Vme =2:1) was used as mobile phase with a flow rate of 1.0 mL min^{-1}. The detection was performed under the wavelength 205 nm at 30 °C, and the inherent error was ±0.001 min. At least six tests were conducted for above characterizations, and the means or typical pictures were used for analysis.

3.3. Result and Discussion

3.3.1. JLP-to-Crystal Transition Phenomenon

Generally, drug crystals are crystallized out directly from corresponding solution when cooling or when the poor solvent is added. For CTX, it is apt to be trapped into JLP when its solution is supersaturated by cooling or anti-solvent method without seeding. The JLP can also form when the CTX amorphous powder was placed under certain temperature and relative humidity. It is an interesting phenomenon that the JLPs slowly transformed into crystals as shown in Figure **3**-**2**, Figure **3**-**3**, and Figure **3**-**4**. J1 completely transformed into C1 at 20.0 ± 0.3 °C in 7 h. J2 transformed into C2 at -20.05 ± 0.04 °C for 8 days, and it took 4 h for J3 to transform into C3. Crystal habits of C1-C3 are different, as shown in Figure **3**-**5**. C1 is needlelike and about 20-30 μm. C2 is sticklike and approximately 100 μm in size. C3 is plate-like, and its size is 150-200 μm. The CTX crystals obtained from JLP crystallization are obviously larger than those obtained by solution crystallization with seeding (no JLP occurs). On the other hand, there is no agitation in the JLP crystallization process. This would reduce crystal breakage and secondary nucleation due to the shearing force. In addition, most of the CTX molecules are enriched into JLP during the JLP formation. This leads to extremely high supersaturation in JLP, which favors crystal growth. The XRPD patterns of C1-C3 are described in Figure **3**-**6**. The top five strongest

peaks of C1, C3, and the CTX standard sample are same (C1: 9.02 ± 0.01, 16.60 ± 0.01, 20.98 ± 0.01, 22.02 ± 0.01, and $24.84 \pm 0.01°$; C3: 8.98 ± 0.01, 16.62 ± 0.01, 20.97 ± 0.01, 22.02 ± 0.01, and $24.82 \pm 0.01°$; and CTX standard sample: 9.03 ± 0.01, 16.61 ± 0.01, 20.97 ± 0.01, 22.02 ± 0.01, and $24.85 \pm 0.01°$), so they are concluded the same crystal form. The TGA curve of C1 (in Figure **3-7**) clearly shows a mass loss of (3.6 ± 0.1)% from 70 to 110 °C before decomposition. C3 has the same TGA characteristic as C1. The KF titration analysis manifested that C1 contains (3.5 ± 0.2)% water, which is basically consistent with the TGA analysis although there is a little different that probably due to the uncertainty of the moisture from the air and the inherent errors. It is reasonable to speculate that the mole ratio of CTX to water is 1:1, namely, C1 is monohydrate. The top five strongest peaks of C2 are 6.72 ± 0.01, 7.07 ± 0.01, 21.52 ± 0.01, 21.94 ± 0.01, and $24.57 \pm 0.01°$, which are evidently different from the others [25], so C2 is a new crystal form. TGA curve of C2 in Figure **3-7** shows an obvious weight loss around 110 °C before decomposition, which agrees with the characteristics of the DSC curve (appended Figure 0-1). This means C2 is also a solvate. The HPLC chromatograms in appended Figure 0-2 show that the retention time $(3.33 \pm 0.01$ min) of the solvent of C2 is basically consistent with that of DMF $(3.34 \pm 0.01$ min), which demonstrates that C2 is a DMF solvate. It is noteworthy that the CTX crystal forms discovered until now are all solvates [26–28]. The phenomenon indicates that solvent-CTX molecule interactions are much stronger and that the solvent directly participates into the construction of CTX crystal structure.
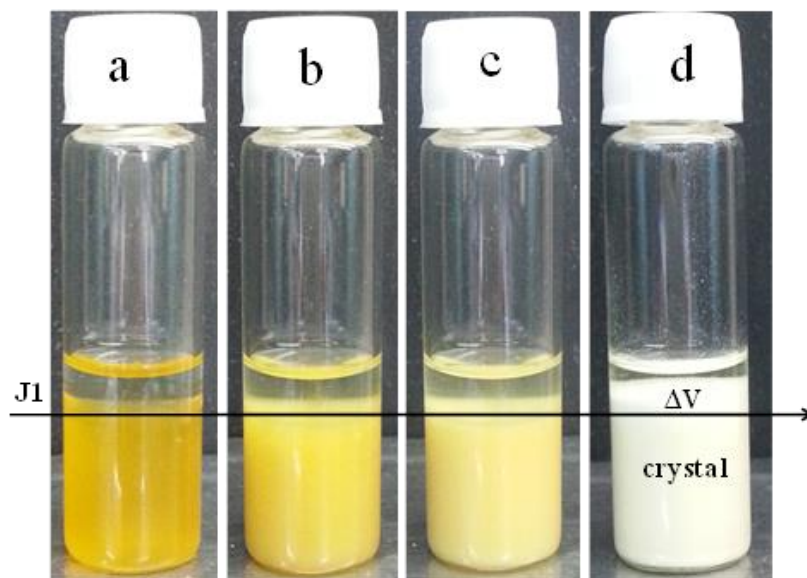
Figure 3-2: The appearance of the J1-to-C1 transition at different times: (a) 0h, (b) 2h, (c) 4h, (d) 7h
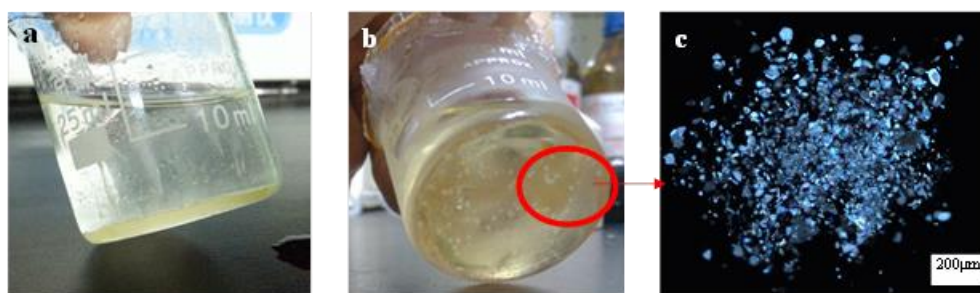
Figure 3-3: The phase transition from J2-to-C2: (a) the appearance of J2, (b) J2 partially transited into crystals, (c) PLM image of crystals formed in J2
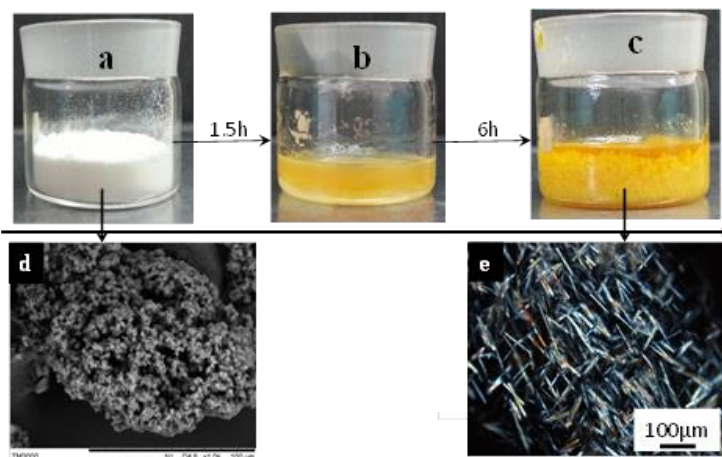
Figure 3-4: The phase transition from amorphous through J3 to C3:(a) the appearance of an amorphous powder, (b) the appearance of J3,(c) J3 partially transited into crystals, (d) SEM image of an amorphous powder, (e) PLM image of crystals formed in J3
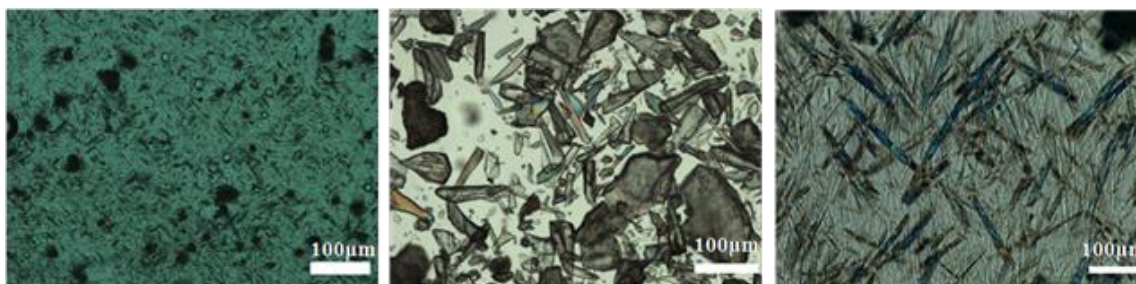
Figure 3-5: Images of CTX crystals obtained from JLP crystallization: (a), (b) and (c) are microscope images of C1，C2 and C3 respectively
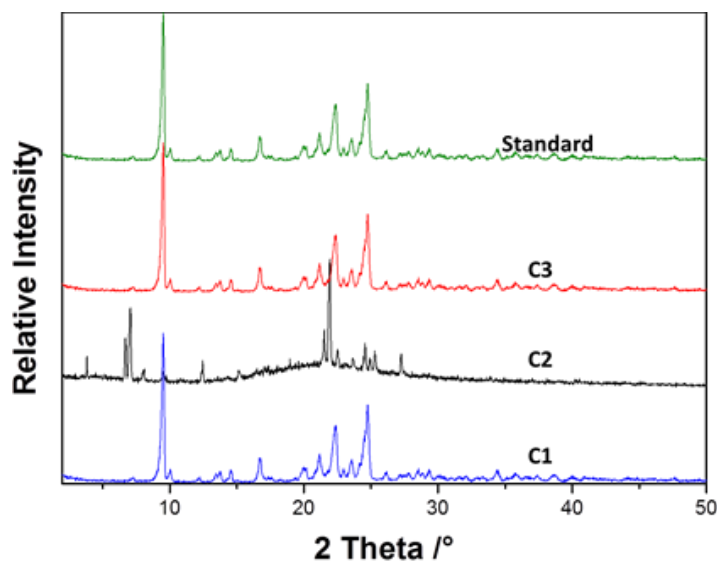
Figure 3-6: XRPD patterns of C1, C2, C3, and CTX standard

3.3.2.　　Effect of Solvent on JLP Formation and Crystallization

To investigate the effects of solvent on the formation and crystallization of JLP, CTX amorphous adsorption experiments were designed in which CTX amorphous powder was placed under different saturated solvent atmospheres. Considering that temperature would affect phase behavior, the experiments were first conducted at different temperatures under saturated steam to determine the temperature threshold. Table 3-1 clearly shows that JLP formation and crystallization became more and more difficult with the decrease in temperature. At 2.0 ± 0.4 °C, only part of amorphous phase transformed into JLP, and the JLP-to-crystal transition did not occur. The slow transformation is probably due to the slow kinetics at low temperature. Therefore, the amorphous adsorption experiments under different saturated solvent atmosphere were carried out at 20.2 ± 0.8 °C, and the results are listed in Table 3-2. JLP formation is the result of the solvation of CTX molecules. Solvation depends on the solvent-solute molecule interactions, which involve ion-dipole, dipole-dipole, and hydrogen bonding [29]. The polarity and the hydrogen bonding ability of the solvent can be evaluated by Kamlet-Taft parameters that include the polarizability parameter, π^*, the hydrogen-bond donor (HBD) acidity, α, and the hydrogen-bond acceptor (HBA) basicity, β. The values of the three parameters of the solvents used are also listed in Table 3-2 [29]. As π^* decreases, JLP formation became more and more difficult. When π^* decreases to 0.55, CTX cannot be solvated, and no JLP forms. This means that more polar solvents favor JLP formation. The hydrogen bonding ability of the solvent has no obvious influence. This can be explained by the chemical structure of CTX. There are Na+, carboxylate, and several strong polar groups, such as amine and acyl, in the CTX molecule. These are prone to form ion-dipole and dipole-dipole interactions with a polar solvent. Glycol is an exception most likely due to the poor diffusion caused by its high viscosity. From Table 3-2, it can be also seen that not all the JLPs formed would transform into crystals. For the JLPs formed in acetonitrile, acetone, and chloroform, for which α and β are both less than 0.5, crystallization did not occur. While in a solvent with α or β above 0.5 (except DMSO), JLP-to-crystal transition occurred. This implies that the hydrogen bonding ability of the solvent affects CTX crystal formation, and further research results are discussed in section 3.3. The JLP formed in DMSO did not crystallize because of the

high solubility of CTX in DMSO. The crystals crystallized under formamide, pyridine, and methanol atmosphere had different habits (as shown in appended Figure 0-3).
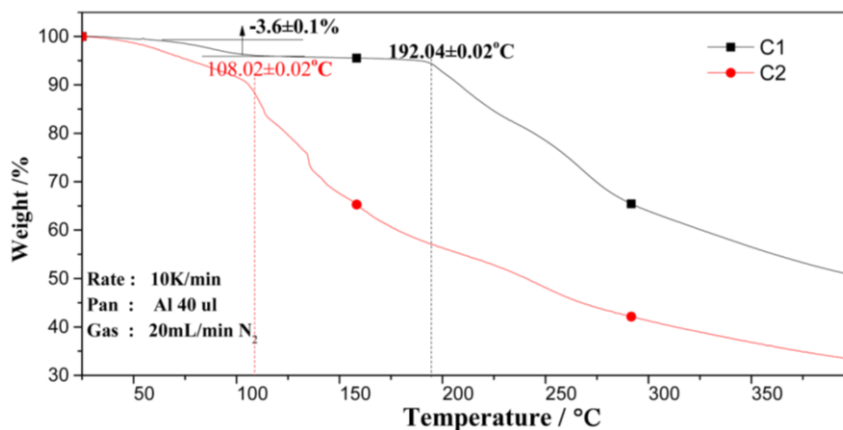
Figure 3-7: TGA curves of C1 and C2

Table 3-1: Results of adsorption experiments at different temperatures under saturated steam

Temperature (°C)	JLP formation [a]	JLP-to-crystal transition [b]
40.0±0.8	J	C(24hrs)
30.1±0.6	J	C(24hrs)
20.2±0.8	J	C(48hrs)
2.0±0.4	Jp	N

a: 'J/Jp' respectively means amorphous transforms into JLP completely or partially; b: 'C/N' respectively means JLP crystallization occurs or not, data in the bracket are the time required for crystallization.

Table 3-2: Results of adsorption experiments under different saturated solvents atmosphere at 20.3±0.8 °C [a]

Solvent	JLP formation [b]	JLP-to-crystal transition [c]	π^*	α	β	Molar solubility (10^2) [20, 30-31]
water	J	C	1.09	1.17	0.47	1.88
DMSO	J	N	1.00	0	0.76	7.38
formamide	J	Cp	0.97	0.71	0.48	6.44
glycol	N	N	0.92	0.9	0.52	-
DMF	J	C	0.88	0	0.69	5.70
pyridine	J	C	0.87	0	0.64	$<10^{-4}$
acetonitrile	Jp	N	0.75	0.19	0.4	-
acetone	Jp	N	0.71	0.08	0.43	0.09
chloroform	J	N	0.69	0.2	0.1	$<10^{-4}$
methanol	J	Cp	0.60	0.98	0.66	0.097
ethylene acetate	N	N	0.55	0	0.45	$<10^{-4}$
ethanol	N	N	0.54	0.86	0.75	0.03
IPA	N	N	0.48	0.76	0.84	$<10^{-4}$

a: 0.8 °C is the maximum uncertainty of this part adsorption experiments; b: 'J/Jp' respectively means amorphous transforms into JLP completely or partially, and 'N' means no JLP forms; c: 'C/Cp' respectively means JLP transforms into crystal completely or partially, and 'N' means JLP crystallization does not occur.

3.3.3.   Effect of Solvent on Crystal Formation.

To understand the process of crystal formation, J1-to-C1 transition process was chosen to be monitored for convenience. Initially, the JLP was yellow and adhesive. It did not show a regular shape and was moderately flowable as shown in Figure 3-8. The XRPD pattern (Figure 3-9) consisted of very broad and diffuse diffraction, which confirmed that no crystal was present in the JLP. After 1.5 h, the birefringent domain was first detected by PLM, which demonstrated the occurrence of nucleation. On the basis of the CTX solubility data [19, 32], the concentration of CTX in the JLP was approximately 43 times higher than

that in the saturated solution. Although the supersaturation is high, the nucleation rate is slow because of diffusion retardation. After 2 h, more domains were observed in the polarized light view due to crystal growth, which was consistent with the appearance of the characteristic diffraction peaks of CTX at 9.05 ± 0.01, 22.02 ± 0.01, and $24.87 \pm 0.01°$ (Figure 3-8 b and Figure 3-9 b). After 4 h, because of the increasing number of crystals formed, the color of the JLP changed into faint yellow. The size of the crystal reached approximately 20 µm, and the XRPD pattern showed more characteristic diffraction peaks. After 7 h, the JLP entirely transformed into white crystals with a size of 30 µm. The top five strongest peaks of the crystals are 9.02 ± 0.01, 16.60 ± 0.01, 20.98 ± 0.01, 22.02 ± 0.01, and $24.84 \pm 0.01°$, respectively, which demonstrated that the obtained crystals are C1.
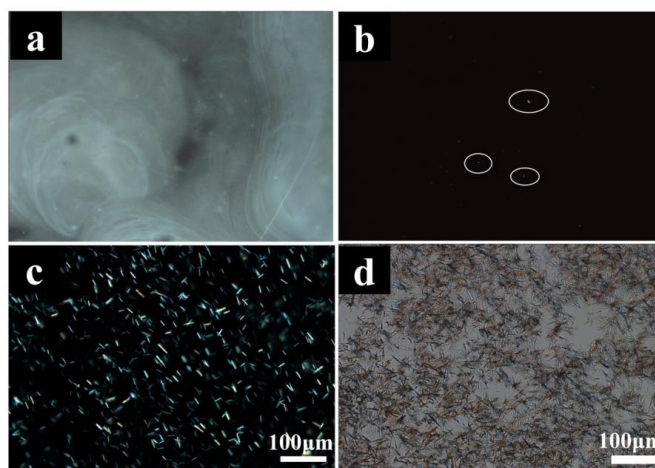
Figure 3-8: Microscopic images of the J1-to-C1 transition process: (a) 0h, (b) 2h, (c) 4h, (d) 7h. (a) and (d) are optical microscope images, (b) and (c) are PLM images
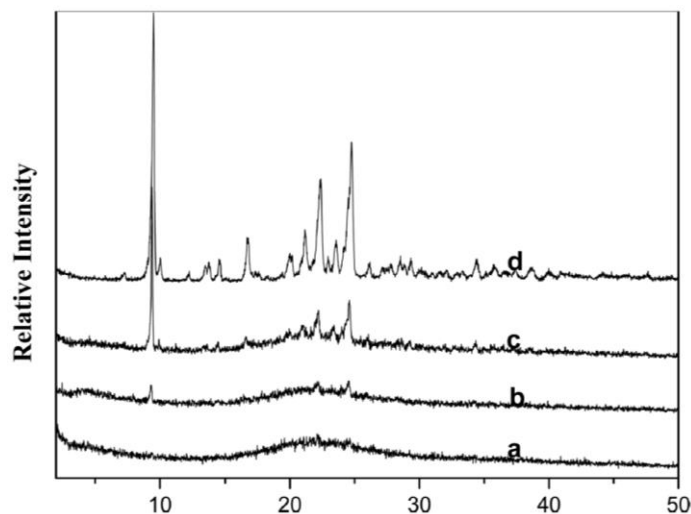
Figure 3-9: XRPD patterns at different times during the J1-to-C1 transition process: (a) 0 h, (b) 2 h, (c) 4 h, and (d) 7 h
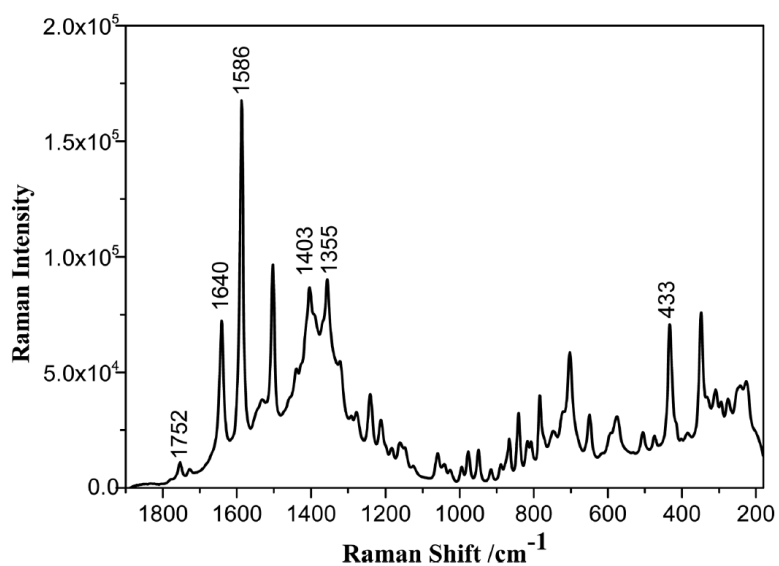
Figure 3-10: Raman spectrum of C1

The molecule interactions in the crystals are usually demonstrated by single-crystal structure analysis. Unfortunately, high-quality crystals for X-ray diffraction are difficult to obtain for cephalosporin antibiotics. Recently, Raman spectroscopy has been proven as a promising in-situ tool to probe molecule interactions. This is due to its low sensitivity to water and widespread applicability to both homogeneous and heterogeneous process. Particularly, it is powerful for studying hydrogen bonding [33, 34]. Hence, an in-situ Raman spectrometer was used to monitor the J1-to-C1 transition process to understand further the

change of molecule interactions during the formation of CTX monohydrate. The Raman spectra of C1 were measured as shown in Figure 3-10. The characteristic peaks were assigned to the corresponding groups. Given that the tension of lactam ring was stronger, the stretching vibration of C=O moved to a higher frequency and appeared at 1752 ± 1 cm^{-1}. Oxime group was ordinarily present from 1620 to 1640 cm^{-1}. The only peak in this range at 1640 ± 1 cm^{-1} was assigned to C=N of oxime group [35]. The strongest peak at 1586 ± 1 cm^{-1} corresponded to the stretching vibration of C=C [35]. The stretching vibration of COO- was observed along with the symmetric and asymmetric vibrations. The peaks at 1531 ± 1 and $1403 \pm 1/1355 \pm 1$ cm^{-1} were assigned to the asymmetric and symmetric stretching vibrations, respectively. The peak at 433 ± 1 cm^{-1} was due to the bending vibration of the six-membered thiazine ring. Detailed information on the Raman band assignment is shown in Table 3-3. The real-time change of Raman spectra is illustrated in Figure 3-11. Initially, the Raman spectra of JLP within 1000-1800 cm^{-1} region was broad and overlapping with a higher baseline, which is due to the hydration of the CTX molecules. The peak at 1347 ± 1 cm^{-1}, representing the symmetric stretching vibration of COO−, is much broader and stronger than the others, indicating that the polar interaction between water and COO− is much stronger than that between water and the other groups. This can be attributed to the strong electronegativity of COO−. The first change occurred after 130 min when the broadband at 1347 ± 1 cm^{-1} shifted to 1355 ± 1 cm^{-1} and gradually changed into two sharp peaks at 1403 ± 1 and 1355 ± 1 cm^{-1}, respectively. This indicates the polar interaction between water and COO− breaks. The break of the stronger interaction appeared first during the transition process suggests that a much more stronger interaction forms between water and COO− which would therefore play a leading role in crystal formation. As shown in Figure 3-12, the presence of a hydroxyl characteristic peak at the wavenumber of 3583 ± 2 cm^{-1} in the FT-IR spectrum of C1 demonstrates that hydroxyl forms intermolecular hydrogen bonding in the crystal [36]. Because there is no hydroxyl in CTX molecule, the hydroxyl presented here must come from water. From the perspectives of HBA, among the several HBAs such as COO−, C=N−, and C=O in the CTX molecule, COO− is the strongest one and has the most probability to form intermolecular hydrogen bond with water. In the meantime, on the aspect of HBD, the HBD acidity of water is stronger than that of −NH2 and −NH in CTX molecule, so it is reasonable for COO− to

accept an intermolecular H bond donated by a water molecule. Meanwhile, another peak at 433 ± 1 cm^{-1} appeared. The peak corresponds to the bending vibration of the six-membered thiazine ring. Its appearance is due to the dissociation of the polar interactions between water and the six-membered thiazine ring. The 1752 ± 1 cm^{-1} band appeared, and the peaks at 1640 ± 1 and 1586 ± 1 cm^{-1} were gradually enhanced. Those peaks correspond, respectively, to the vibration of C=O in lactam ring, C=N of the methoxy oxime, and C=C in the five- or six-membered ring. The increase of the peak intensity is owing to dehydration of the groups and construction of the crystal structure. The JLP-to-crystal transformation completed, and the Raman spectra became clear and sharp after 7 h. The top six strongest peaks of the crystals centered at 1640 ± 1, 1586 ± 1, 1531 ± 1, 1403 ± 1, 1355 ± 1, and 433 ± 1 cm^{-1}, respectively, are consistent with that of C1, demonstrating the obtained crystals are C1. From the above analysis, it can be seen that the formation of the thermodynamic metastable JLP is a purely dynamic-driven process. The volume of the crystals obtained larger than that of the initial JLP (as shown in Figure 3-2) demonstrated that entropy is the driving force for the JLP-to-crystal transition [37]. The ion-dipole and dipole-dipole interactions between water and CTX molecule are mainly responsible for JLP formation. The polar interactions are weaker, and they are not specific and oriented, which can be reflected by the moderate flowability of JLP. Driven by supersaturation, the H-bonding that is stronger, specific, and directional gradually forms between H_2O and COO-. Through the H-bonding, the water serves as a bridge to connect CTX molecules resulting in the development of the 3D periodic structure.

Table 3-3: Observed characteristic peaks of FT-IR and Raman and their assignments for

C1

Wavenumber of FT-IR [a] (cm^{-1})	Raman shift [b] (cm^{-1})	Assignments
3583		Hydroxy stretching vibration
3442/3342		Primary amine NH_2 stretching vibration
3262		Secondary amine N-H stretching vibration
3042		Aromatic heterocyclic C-H chain stretching vibration
1760	1752	C=O (in lactam ring) stretching vibration
1728		Acetoxyl -OCOCH$_3$ stretching vibration
1647	1640	C=N stretching vibration in methoxyoxime
	1586	C=C stretching vibration in five-membered and six-membered ring
1541	1531	Carboxylate radical COO$^-$ asymmetric stretching vibration
1416/1355	1403/1355	Carboxylate radical COO$^-$ symmetric stretching vibration
	817	Symmetric stretching vibration of thiazine ring
	748	Lactam ring stretching vibration
	433	Skeleton bending vibration of Thiazine ring
	274	C-S-C bending vibration
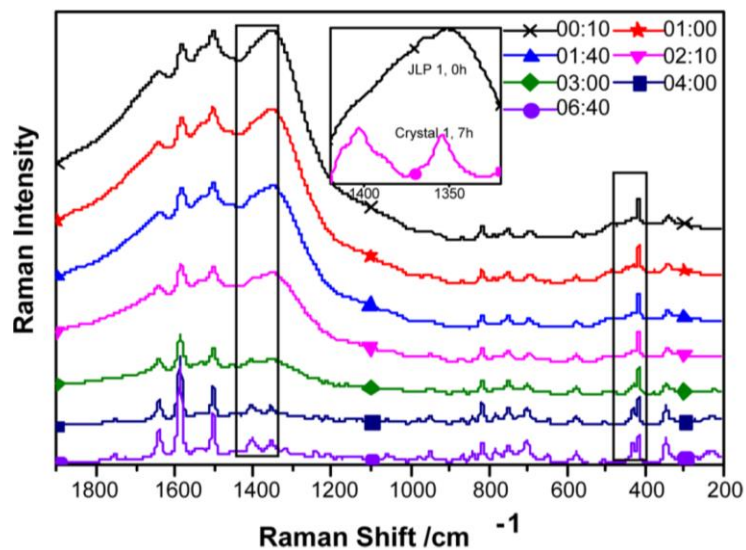
Figure 3-11: Raman spectra (background subtracted) during the J1-to-C1 transition process. Times (hours and minutes, hh: mm) in the legend represent the transition time
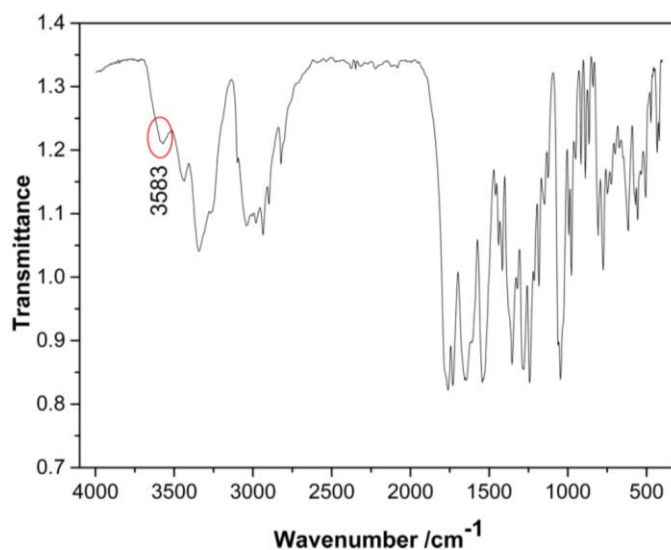
Figure 3-12: FT-IR spectrum of C1

3.4.   Conclusion

The effects of solvent on the formation and crystallization of JLP of CTX have been investigated in detail. The experiments involving 13 different solvents demonstrate that the polar interaction between the CTX and solvent contributes to the formation of JLP and that hydrogen-bonding plays an important role in the formation of CTX solvate crystal (shown in Figure 3-13). The H-bonding between the solvent and CTX molecule has been probed with the aid of FT-IR and in-situ Raman spectroscopy. The results show that the JLP, as a kinetic self-assembly state, forms first by the role of polar solvent in the supersaturated

solution (process a to b in the inset picture). It takes several hours for the CTX and solvent molecules to identify each other through hydrogen bonding and build a long-range order structure (b to c). From the view of thermodynamics, the whole process is a transition from a local energy minimum to an overall energy minimum. Solvent molecules act as a bridge to connect CTX molecules, so CTX crystals exist as a solvate. The facts suggest that the organization pattern of the CTX molecules can be modulated by introducing solvent molecules. The JLP crystallization makes it possible to optimize the form and habit of crystals that are difficult to crystallize out in solution. The results bring a better understanding of JLP-to-crystal transition of active pharmaceutical ingredients and may have good application prospects in drug crystal preparation. The latest research progress in gel-to-crystal transition prompts us that more attention should be paid to the kinetic study and molecular simulation of JLP crystallization process [38].
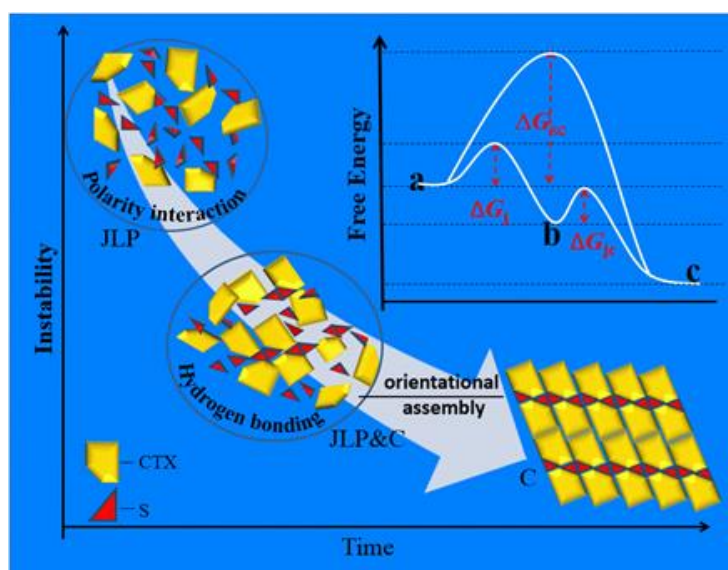
Figure 3-13: Schematic model for JLP-to-crystal transition mechanism. **C** and **S** represent crystal and solvent respectively, **a**, **b** and **c** represent supersaturated solution, JLP, and crystal respectively

3.5.   References

1. Zhao, F.; Ma, M. L.; Xu, B. Molecular hydrogels of therapeutic agents. Chem. Soc. Rev. 2009, 38, 883−891.

2. Sorensen, T. J. Oiling-Out and Crystallization of Vanillin from Aqueous Solutions. Chem. Eng. Technol. 2014, 37 (11), 1959−1963.

3. Ilevbare, G. A.; Taylor, L. S. Liquid-liquid phase separation in highly supersaturated aqueous solutions of poorly water-soluble drugs: implications for solubility enhancing formulations. Cryst. Growth Des. 2013, 13 (4), 1497−1509.

4. Lu, J.; Li, Y. P.; Wang, J.; Ren, G. B.; Rohani, S.; Ching, C. B. Crystallization of an active pharmaceutical ingredient that oils out. Sep. Purif. Technol. 2012, 96, 1−6.

5. Derdour, L. A. Method to crystallize substances that oil out. Chem. Eng. Res. Des. 2010, 88, 1174−1181.

6. Anderson, V. J.; Lekkerkerker, H. N. W. Insights into phase transition kinetics from colloid science. Nature 2002, 416, 811−815.

7. Wu, Y. P.; Wu, S.; Zou, G.; Zhang, Q. J. Solvent effects on structure, photoresponse and speed of gelation of a dicholesterollinked azobenzene organogel. Soft Matter 2011, 7, 9177−9183.

8. Vintiloiu, A.; Leroux, J. C. Organogels and their use in drug delivery-A review. J. Controlled Release 2008, 125, 179−192.

9. Kumar, D. K.; Steed, J. W. Supramolecular gel phase crystallization: orthogonal self-assembly under non-equilibrium conditions. Chem. Soc. Rev. 2014, 43, 2080.

10. Terech, P. N.; Sangeetha, M.; Maitra, U. Molecular Hydrogels from Bile Acid Analogues with Neutral Side Chains: Network Architectures and Viscoelastic

Properties. Junction Zones, Spherulites, and Crystallites: Phenomenological Aspects of the Gel Metastability. J. Phys. Chem. B 2006, 110, 15224−15233.

11. Kapoor, I.; Schon, E. M.; Bachl, J.; Kuhbeck, D.; Cativiela, C.; Saha, S.; Banerjee, R.; Roelens, S.; Marrero-Tellado, J. J.; Diaz, D. D. Competition between gelation and crystallization of a peculiar multicomponent liquid system based on ammonium salts. Soft Matter 2012, 8, 3446−3456.

12. Ouyang, J. B.; Wang, J. K.; Huang, X.; Gao, Y.; Bao, Y.; Wang, Y. L.; Yin, Q. X.; Hao, H. X. Gel formation and phase transformation during the crystallization of Valnemulin Hydrogen Tartrate. Ind. Eng. Chem. Res. 2014, 53 (43), 16859−16863.

13. Moffat, J. R.; Smith, D. K. Metastable two-component gel exploring the gel−crystal interface. Chem. Commun. 2008, 19, 2248−2250.

14. Cui, J. X.; Shen, Z. H.; Wan, X. H. Study on the gel to crystal transition of a novel sugar-appended gelator. Langmuir 2010, 26, 97−103.

15. Houton, K. A.; Morris, K. L.; Chen, L.; Schmidtmann, M.; Jones, J. T. A.; Serpell, L. C.; Lloyd, G. O.; Adams, D. J. On crystal versus fiber formation in dipeptide hydrogelator systems. Langmuir 2012, 28, 9797−9806.

16. Zhu, P. L.; Yan, X. H.; Su, Y.; Yang, Y.; Li, J. Solvent-induced structural transition of self-assembled dipeptide: from organogels to microcrystals. Chem. - Eur. J. 2010, 16, 3176−3183.

17. Xu, Y.; Kang, C. Q.; Chen, Y.; Bian, Z.; Qiu, X. P.; Gao, L. X.; Meng, Q. X. In-situ gel-to-crystal transition and synthesis of metal nanoparticles obtained by fluorination of a cyclic β-amino alcohol gelator. Chem. - Eur. J. 2012, 18, 16955−16961.

18. Braga, D.; D'Agostino, S.; D'Amen, E.; Grepioni, F. Polymorphs from supramolecular gels: four crystal forms of the same silver (I) supergelator crystallized directly from its gels. Chem. Commun. 2011, 47, 5154−5156.

19. Yin, Y. H.; Gao, Z. G.; Bao, Y.; Hou, B. H.; Hao, H. X.; Liu, D.; Wang, Y. L. Gelation phenomenon during anti-solvent crystallization of cefotaxime sodium. Ind. Eng. Chem. Res. 2014, 53, 1286−1292.

20. Zhang, H. T. Research on Crystallization Technique of Cefotaxime Sodium. Ph.D. thesis, Tianjin University, January 2008.

21. De Albuquerque, I.; Mazzotti, M. Crystallization process design using thermodynamics to avoid oiling out in a mixture of vanillin and water. Cryst. Growth Des. 2014, 14 (11), 5617−5625.

22. Ren, R. J.; Sun, D. Q.; Wei, T. T.; Zhang, S. X.; Gong, J. B. The Role of Diastereomer Impurity in Oiling-Out during the Resolution of trans-4-Methyl-2-piperidine Carboxylic Ethyl Ester Enantiomers by Crystallization. Org. Process Res. Dev. 2014, 18, 709−716.

23. Takasuga, M.; Ooshima, H. Control of crystal size during oiling out crystallization of an API. Cryst. Growth Des. 2014, 14 (11), 6006−6011.

24. Working Group 1 of the Joint Committee for Guides in Metrology. Evaluation of measurement data−guide to the expression of uncertainty in measurement; JCGM 100:2008 GUM 1995 with minor corrections; Joint Committee for Guides in Metrology, 2008.

25. Bao, Y.; Gao, Z. G.; Hou, B. H.; Zhou, L. N.; Hao, H. X.; Wang, Z.; Yin, Q. X.; Chen, W.; Xie, C. N, N-Dimethyl formamide solvate of Cefotaxime sodium and preparation method. China Patent 103804395, May 21, 2014.

26. Park, S. H. Study on Polymorphism of Cefotaxime Sodium, Cephradine, and Ceftriaxone Sodium. Ph.D. thesis, Duksung Women's University, August 2003.

27. Macher, I.; Widschwenter, G. Production of cefotaxime and new sodium salts. U.S. Patent 5831086, November 3, 1996.

28. Sohn, Y. T.; Kim, H. K. Dissolution of Crystal Forms of Cefotxime Sodium. J. Korean Pharm. Sci. 1998, 28, 81−85.

29. Reichardt, C.; Welton, T. Solvents and Solvent Effects in Organic Chemistry, 4th ed.; John Wiley & Sons: Weinheim, Germany, 2011; 448−481.

30. Pardillo-Fontdevila, E.; Acosta-Esquijarosa, J.; Nuevas-Paz, L.; Gago-Alvarez, A.; Jauregui-Haza, U. Solubility of cefotaxime sodium salt in seven solvents used in the pharmaceutical industry. J. Chem. Eng. Data 1998, 43 (1), 49−50.

31. Zhang, H. T.; Wang, J. K.; Chen, Y.; Zhang, M. J. Solubility of sodium cefotaxime in different solvents. J. Chem. Eng. Data 2007, 52 (3), 982−985.

32. Zhang, H. T.; Wang, J. K.; Chen, Y.; Nie, Q. Solubility of sodium cefotaxime in aqueous 2-propanol mixtures. J. Chem. Eng. Data 2006, 51, 2239−2241.

33. Huang, J. J.; Hao, H. X.; Wang, Y. L.; Bao, Y.; Ye, W.; Xie, C.; Yin, Q. X.; Sun, Z. H. Investigation on Main Reaction and Side Reaction Mechanism in the Synthetic Process of 1-(5-Bromothiophen 2-yl)-3-(4−3nitrophenyl)prop-2-en-1-one Using Raman Spectroscopy. Org. Process Res. Dev. 2014, 18 (12), 1686−1695.

34. Cui, P. L.; Zhang, X. W.; Yin, Q. X.; Gong, J. B. Evidence of Hydrogen-Bond Formation during Crystallization of Cefodizime Sodium from Induction-Time Measurements and In-Situ Raman Spectroscopy. Ind. Eng. Chem. Res. 2012, 51, 13663−13669.

35. Larkin. P. Infrared and Raman Spectroscopy: Principles and Spectral Interpretation; Elsevier: Amsterdam, 2011; pp 135−176.

36. Brinkley, R. L.; Gupta, R. B. Intra-and intermolecular hydrogen bonding of 2-methoxyethanol and 2-butoxyethanol in n-hexane. Ind. Eng. Chem. Res. 1998, 37, 4823−4827.

37. Frenkel, D. Entropy-driven phase transitions. Phys. A, 1999, 263, 26−38.

38. Liu, J.; Xu, F.; Sun, Z.; Pan, Y.; Tian, J.; Lin, H. C.; Li, X. A supramolecular gel based on a glycosylated amino acid derivative with the properties of gel to crystal transition. Soft Matter 2016, 12, 141.

Chapter 4

Motion-Based Multiple Object Tracking of Ultrasonic-Induced Nucleation: A Case Study of L-Glutamic Acid

4. Motion-Based Multiple Object Tracking of Ultrasonic-Induced Nucleation: A Case Study of L-glutamic Acid

Abstract

A robust nucleation tracking technology was proposed to track the nucleation process of L-glutamic acid in this study. Motion-based multiple object tracking (MMOT) model was introduced to crystallization, for the first time, to help to track the moving crystals A waterproof micro-camera combined with a home-designed vial adaptor was used to record the nucleation process video stream. Optimization of parameters in the MMOT model and a moving average (MA) based smoothing method helped to determine the starting point of nucleation. Results showed the newly developed technology performed better under the influence of ultrasonic irradiation which disabled the use of focused beam reflection measurement (FBRM).

4.1. Introduction

Nucleation from solution has aroused great interest over the past decades. Elucidations of the nucleation mechanism have enhanced our understanding of many basic mechanisms related to natural processes (e.g. protein crystallization) and industrial practices (e.g. functional materials, active pharmaceutical ingredients) [1–3]. Scientists have considered intermolecular forces in atomistic levels in the order of 10^{-10} m and time scales in the order 10^{-13} s with the help of advanced instruments [4]. However, in industrial crystallization, there is still a limitation in monitoring nucleation at the initial stage of critical nucleus formation [5]. Existing measuring techniques used to monitor nucleation include FBRM, turbidity, ultrasonic velocity, electrical conductivity, and light transmittance measurement of bulk solution [6]. The accuracy of nucleation monitoring devices affects the estimation nucleation kinetics i.e. induction time and metastable zone width (MSZW). In order to improve this accuracy, progress has been made using high-speed imaging, multivariate statistical process monitoring charts *etc.* [7–10]. Binary segmentation is the most common algorithm used in the segmentation of individual crystals in a single image. A multi-scale segmentation method was studied to extract crystals from the background of varied illumination [11]. Presles *et al*. proposed a restoration method to measure the particle size distribution of unfocused crystals from a segmented image [12]. While there have limitations

in the segmentation of overlap particles in a high solid concentration system. Accordingly, Ahmad *et al.* proposed a segmentation method that is based on salient corner detection and geometric grouping, which can separate the overlapping particles during the batch crystallization process at different solids concentrations [13]. These studies focused on particle size and shape to analyze the properties of crystals. Recently, the MMOT model has been widely used in the computer vision field, including activity recognition, traffic monitoring, automotive safety *etc.* MMOT algorithm is a motion-based detection method that is coupled with an adaptive background remover to find moving objects in successive frames. It can detect moving objects in a video stream, predict their locations in the next frame, and record the object count automatically, which shows its potential application in monitoring the occurrence and disappearance of nuclei in a bulk solution.

External factors such as ultrasound, microwave, magnetic field, and electric field have been studied to control crystal nucleation, which are very effective in some cases [14–17]. Ultrasonic irradiation creates sequential compression and expansion of the solution, which leads to the formation and growth of bubbles. Finally, the bubbles collapse and release energy, promoting nucleation within a short induction time and at a lower supersaturation level. Parameters e.g. ultrasound power, frequency, with or without pulses, have a significant influence on the nucleation process and crystal qualities [18,19]. Based on the authors' experience, techniques such as FBRM, light transmittance and turbidity measurement, have certain limitations for the measurement of the onset of nucleation, especially under the influence of external factors. With these traditional methods, it is difficult to locate the initial few nuclei. In this study, the MMOT was introduced to crystallization, for the first time, to monitor the nucleation of L-glutamic acid. To improve the accuracy of the system, the contrast ratio between foreground and background and the area of blob analysis (blobs are connected groups of foreground pixels that are considered as moving objects) were tuned to achieve the best tracking performance of nuclei. Results showed that ultrasonic irradiation shortened the induction time dramatically. The newly developed monitoring technology based on MMOT, which is much cheaper than the existing methods, showed improved accuracy and precision under the influence of ultrasonic irradiation, while FBRM showed poor performance because of the existence of bubbles.

4.2. Experimental and Methods

L-glutamic acid (LGA) was purchased from Alfa Aesar (99+%, β form, Ward Hill, MA) and used as a model compound in this study. A VCX 500 ultrasonic processor (Sonic & Materials Inc.) was inserted into a double jacketed crystallizer to generate ultrasound. During the nucleation process, a waterproof USB-based micro-camera coupled with a 3D printed vial adaptor was inserted into the solution to track the onset of nucleation as shown in Figure 4-1. A home-designed vial adaptor with a suspension flow channel, as shown in Figure 4-1, was connected to the end of the micro-camera to capture crystal images as the slurry flows through the vial adaptor. Figure 4-2 shows the experimental setup. Details of the technical specifications of the camera probe are listed in Table **4**-**1**. In the first step, a saturated solution (30.0 g/L and 40.0 g/L) was prepared in the double jacketed crystallizer. Then the solution was heated up to 80.0 ℃ and the temperature was maintained for 30 minutes to ensure complete crystal dissolution. Afterward, the nucleation temperature of the clear solution was reached as soon as possible by switching to another refrigerated circulator (FT50, Julabo, Germany) from heating to cooling. The ultrasound probe and micro-camera were turned on at the same time when the solution reached the nucleation temperature. The temperature was kept constant to study the nucleation kinetics until the crystals filled the video frame. The video recorded by micro-camera was parsed by MMOT in MATLAB (R2016b, MathWorks). The MMOT code that used in this application was appended in Table 0-1. For every experimental condition, at least six cycles of heat-hold-cool were repeated to obtain reliable data.
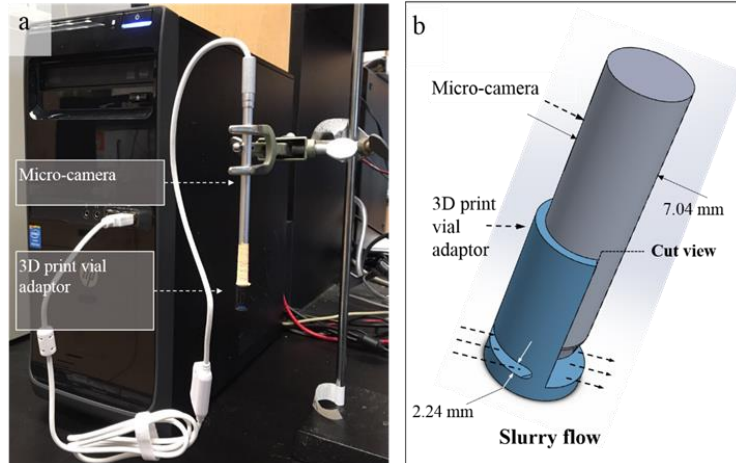
Figure 4-1: (a) Portable USB digital micro-camera setup; (b) Cut view of the 3D print vial adaptor. The slot is 2.24 mm in height and 7.04 mm in width

Table 4-1: Technical specifications of micro-camera used in this study

Image sensor	2 Mega Pixels
Field of view	10.8° (×200)
Depth of field	~50 microns (×200)
Camera resolution	1600*1200
Display speed	Max. 30 fps
Magnification	Max. 300
Light source	LED illumination
Interface	USB 2.0
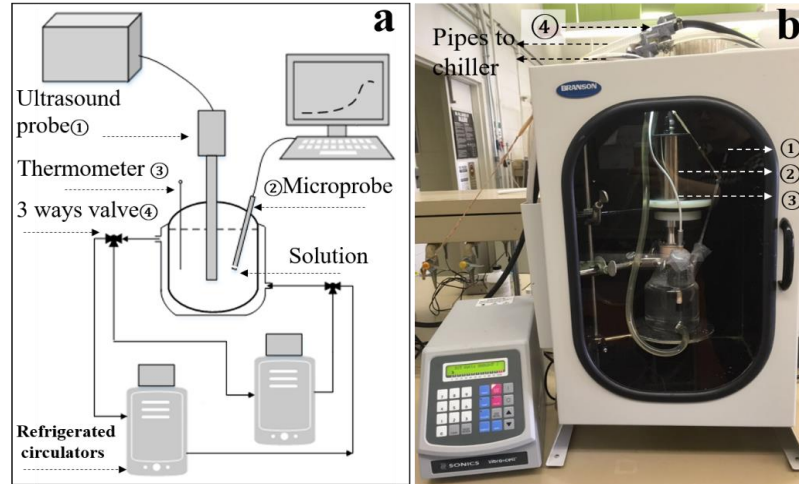
Figure 4-2: (a) Schematic of the experimental setup. (b) Experimental setup picture. Crash cooling of the solution was realized by switching three-way valves to reach the nucleation temperature as soon as possible. The micro-camera was coupled with MATLAB to measure crystal counts through the motion-based multiple object tracking model.

4.3.   Results and Discussions

Coupled with the vial adaptor, the micro-camera was inserted into the crystallizer to record the video stream of the whole nucleation process. The conditions with the solution concentration at 30 g/L, 40 g/L and the nucleation temperature at 35 °C, 45 °C were tested. Once the recording was finished, the video stream was parsed by the MMOT model (The code was attached in the supporting information) in MATLAB. The tracking model is solely based on motion, in which the background is subtracted and a Kalman filter is used to predict the assigned track's location in the next frame. The number of assigned objects is counted and then the trend between the crystals counts versus the time series is plotted to analyze the nucleation process. In this study, the crystals counts were smoothed by the MA model:

$$MA = \frac{c_m + c_{m-1} + \cdots + c_{m-(n-1)}}{n} = \frac{1}{n}\sum_{i=0}^{n-1} c_{m-i} \tag{4-1}$$

$$MA_{current} = MA_{prev} + \frac{c_m - c_{m-n}}{n} \tag{4-2}$$

Where c indicates the crystals counts along with time series, MA_{prev} indicates the previous averaged value. The moving period n was optimized to be 30 which is a good reflection of the trend of crystals counts in real time. In the MMOT model, there are two key parameters optimized in this study, foreground detector (pixel value) and blob analyzer (blob area).

The foreground detector can segment moving object from the background, in which the pixel value of 0 corresponds to background and the value of 1 corresponds to foreground. In blob analyzer, the detection area of connected groups (called 'blobs' or 'connected components') of foreground pixels determines the analytical size of moving objects. These parameters in nucleation tracking are related with the model compound (crystal luster, color etc.) and the type of micro-camera (magnification, resolution). The pixel value and blob analysis area were optimized to be 0.8 and 30, respectively. The starting point of the continuously increasing micro-camera counts was recognized as the occurrence of nucleation. The induction time was calculated as the period between when the ultrasound processor was turned on and the appearance of crystals. Take the video stream at 40 g/L and 35°C under ultrasonic irradiation as an example. Figure 4-3 shows detection results of the 95th second of the process after the ultrasonic processor was started. The real time tracking curve at 38 seconds was attached in appended information (Figure 0-4) for comparison.
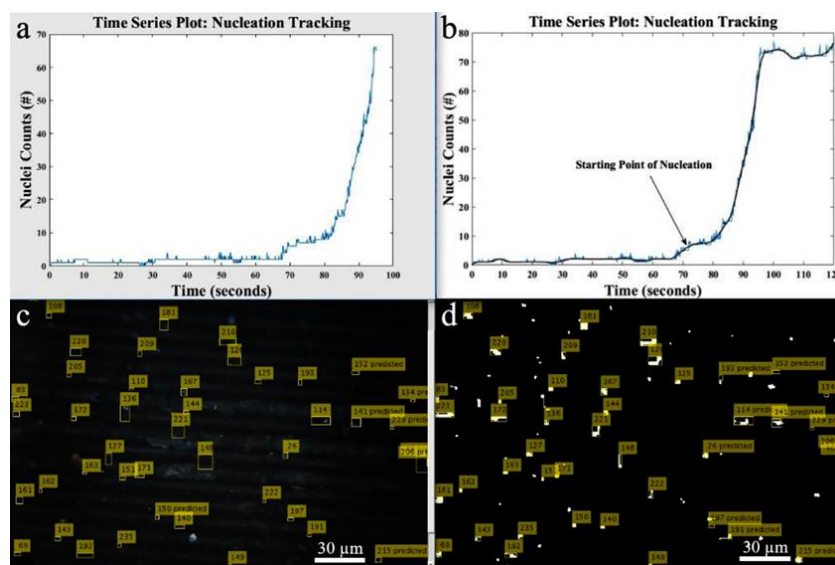
Figure 4-3: In-situ detection results under the conditions of 40 g/L and 35°C. (a) Plot at 95th second of crystals counts against time series using the MMOT model; (b) Plot of crystals counts against time based on nucleation tracking of the whole process: the blue line was drawn according to raw image data and the black line was smoothed by MATLAB using the MA model. (c) Detected objects at 95th second marked in an original video. (d) Detected objects at 95th second marked in the video after background subtraction

As shown in Figure 4-3 (c), there are large quantities of objects were detected at 95th second after the ultrasound processor was started, while only a few objects were detected

in the first 38 seconds (appended in Figure 0-4), which indicates no nucleation occurred. A continuously increasing crystal count was detected after the 72nd second in Figure 4-3 (a) that with the constant nucleation occurring in raw image Figure 4-3 (c), which confirmed the initial nucleation at 72nd second. Comparing the figures in 95s and 38s, conclusions can be drawn that the threshold of background noise is around 5, which can be ignored before the continuous increase of crystals counts. The noise is caused by the existence of caves on the surface of vial adaptor, and bubbles generated from the surface caves would affect the measurement at the initial stage. The average results were reported in Table 4-2.

Table 4-2: Comparison of induction time and crystal form of LGA with/without ultrasonic irradiation

Ultrasonic power (W)	Concentration (g/L)	Nucleation temperature (°C)	S_0, α (C_0/C^*)	S_0, β (C_0/C^*)	Induction time (s)	Standard deviation (s)	Crystal form
14	30	35	1.91	2.51	181.3	8.2	α
14	40	35	2.54	3.35	77.8	4.0	α
14	30	45	1.31	1.78	585.6	22.1	α, β
14	40	45	1.74	2.37	113.0	7.7	α, β
0	30	35	1.91	2.51	1824.3	100.9	α
0	40	35	2.54	3.35	381.3	40.8	α
0	30	45	1.31	1.78	3600.0	169.7	β
0	40	45	1.74	2.37	737.3	68.3	β

Note: Standard deviation was calculated by $Stdev = \sqrt{\frac{\sum_{i=1}^{n}(X_i - X)^2}{n-1}}$, and X means an average of all X_i (i=1, 2, 3…, n, n≥6); C_0 is initial concentration and C^* is the solubility at the same temperature, S_0 is supersaturation calculated by C_0/C^*. The solubility data come from the reference [20].

The smoothed curve helped to pick out the starting point of nucleation more accurate. From Table 4-2, the average induction time is 181.3 seconds under the conditions of 30 g/L, 35 °C and 14 W ultrasonic irradiation. Considering the external disturbance, the standard deviation was calculated from multiple experiments under the same conditions, the actual induction time determined to be 181.3 ± 8.2 s. The measurements under the other conditions e.g. nucleation temperature, initial concentration, and ultrasound power were run using the same procedures. Results were listed in Table 4-2, which showed the

acceleration of the nucleation process (5 to 10 times) by ultrasonic irradiation. The crystal polymorph was confirmed by the morphology of crystals in the micro-camera because an obvious difference of crystal morphology existed between the α form (prismatic) and β form (needlelike). At the nucleation temperature 45 ℃, ultrasound promoted the nucleation of the metastable form (α) as well as stable form (β), which was different with the nucleation process without ultrasound irradiation (β form).

One of the motivations for developing MMOT based nucleation tracking technology was the limitation of FBRM in nucleation tracking under the influence of ultrasonic irradiation. As shown in Figure 4-4 (a), FBRM probe and the micro-camera were used in the same experiment and the results showed that the FBRM counts cannot reflect the starting point of nucleation. In the early stage, the sharp rise of FBRM counts was caused by air bubbles that were generated by the caves on the surface of the vial. In addition, the FBRM counts (~20000) were affected by the formation, growth, and collapse of bubbles that were generated by ultrasound-induced sequential compression and expansion, which would mask the burst of nuclei (~1200). In contrast, the micro-camera counts clearly show the starting point of nucleation. To have a comprehensive comparison between FBRM and MMOT, experiments were conducted without ultrasonic irradiation under the condition of 40 g/L and 35 ℃. The results shown in Figure 4-4 (b) indicate a similar trend with a consistent starting point of nucleation around 380 seconds. To compare MMOT with traditional technologies, an H.E.L. turbidity probe (HEL, UK) was tested under the same conditions used in MMOT tracking. Results in Figure 4-5 indicate the turbidity meter has 20 seconds (a) and 60 seconds (b) delay in monitoring nucleation compared with the MMOT technology. The turbidity signal is laser based transmittance measurement, in which (b) has a slower response speed without ultrasonic irradiation and the baseline of (a) is higher than (b) because of the bubbles with ultrasonic irradiation. Therefore, the MMOT technology based on micro-camera can be used in the system with and without ultrasound irradiation. In the MMOT model, the foreground detector can effectively eliminate the influence of bubbles through optimizing the parameters of blob analysis. The MMOT technology is more accurate compared to the traditional technologies because nucleation can be detected by the presence of 10 or 20 crystals in the crystallization process. In addition, the MMOT based tracking technology can be potentially used to track the

disappearance of crystals that measure the solubility of crystal products. In further, blob analyzer can be developed to discern crystal shape to monitor the crystal's form and polymorphic transition phenomenon. The MMOT based tracking technology contains an upper limit of tracking. Similar to particle vision measurement (PVM) technology, the micro-camera cannot work when the crystals fill up the vial adaptor. The tracking limit of MMOT counts is about 100 in this study.
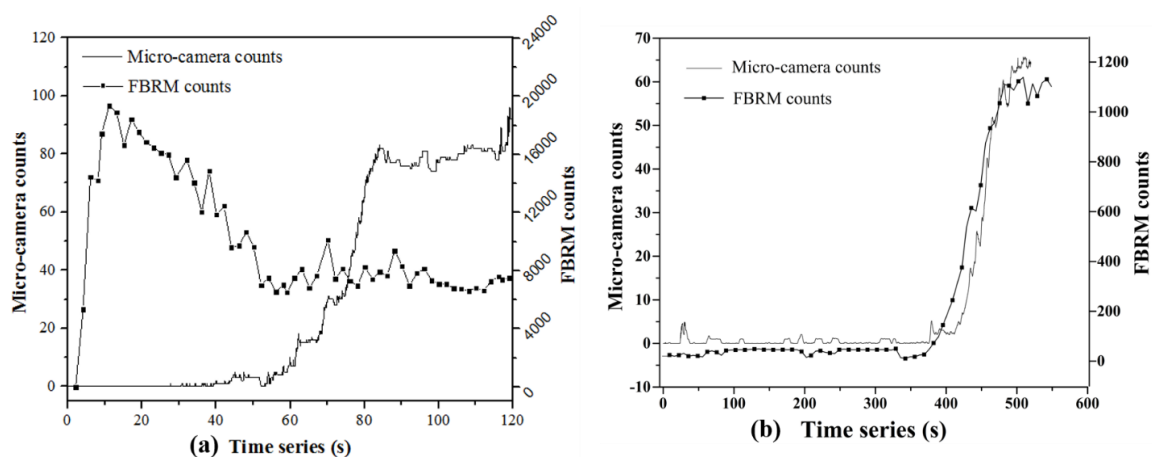
Figure 4-4: Comparison of nucleation tracking performance between FBRM probe and micro-camera probe under the conditions of (a) 30 g/L, 35 °C with 14 W ultrasonic irradiation (b) 40 g/L, 35 °C without ultrasonic irradiation
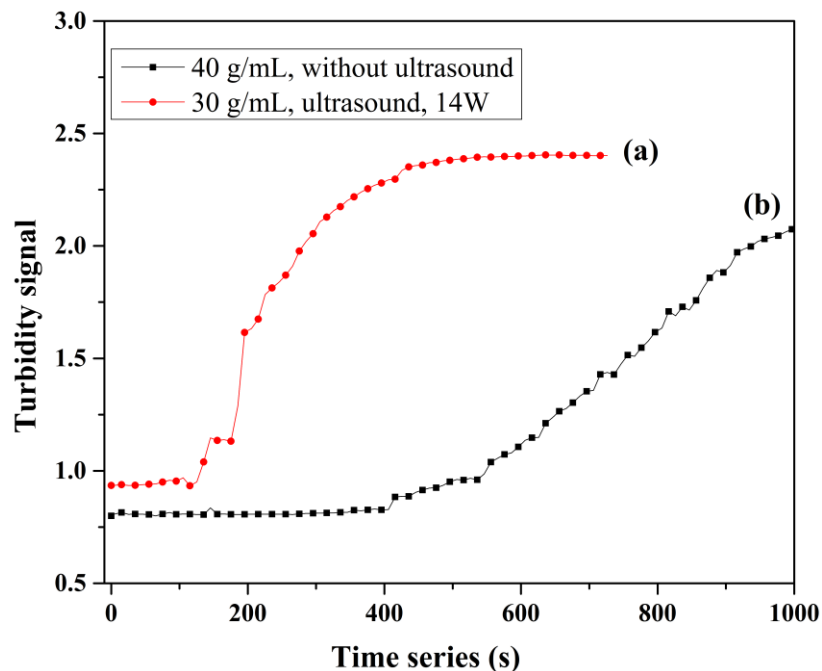
Figure 4-5: Induction time measurement using turbidity meter under conditions of (a) 14 W ultrasonic irradiation, 30 g/L and 35 °C; (b) 40 g/L and 35 °C without ultrasonic irradiation

4.4. Conclusions

In summary, nucleation process can be tracked by (i) cloudiness that measured by naked eyes or light transmittance, (ii) solution concentration measured by Fourier transform infrared (FTIR), (iii) particle counts in a certain size that can be measured by FBRM and MMOT technology. Fujiwara *et al.* estimated the accuracy of eyes, FTIR and FBRM in measuring of metastable zone width of paracetamol. The results indicated FBRM tracking gave the most accurate measurement among them [21]. In this study, the MMOT technology was first introduced to crystallization to detect the onset of nucleation process. Results show MMOT technology has almost same accurate with FBRM in cooling crystallization and can exactly track the nucleation process in which FBRM was disabled by ultrasonic irradiation. The crystal count measured by MMOT, which is different with FBRM count, agrees with the actual crystal count in the video frame. Compared with existing technologies, the newly developed method showed better economic performance. Furthermore, based on MMOT technology, potential applications can be extended to measure solubility, metastable zone width, particle size and even solution-mediated polymorphic transformation.

4.5.   References

1. Zhang, T.; Liu, X. *J Am Chem Soc* **2007**, *129*, 13520–13526.

2. Myerson, A. S.; Trout, B. L. *Science* **2013**, *341*.6148, 855–856.

3. Karthika, T.K; Radhakrishnan; P. Kalaichelvi *Crystal Growth & Design* **2016**, *16*, 6663–6681.

4. Zhang, J.; Chen, P.; Yuan, B.; Ji, W.; Cheng, Z.; Qiu, X. *Science* **2013**, *342*.6158, 611–614.

5. Myerson, A. S. *Handbook of Industry Crystallization, 2nd ed*; Butterworth-Heinemann, 2002.

6. Brandel, C.; Horst, J. *Faraday Discuss* **2015**, *179*, 199–214.

7. Bauerecker, S.; Ulbig, P.; Buch, V.; Vrbka, L.; Jungwirth, P. *J Phys Chem C* **2008**, *112*, 7631–7636.

8. Kawabata, K.; Takahashi, M.; Saitoh, K.; Asama, H.; Mishima, T.; Sugahara, M.; Miyano, M. *Acta Crystallogr Sect D Biological Crystallogr* **2006**, *62*, 239–245.

9. Pöllänen, K.; Häkkinen, A.; Reinikainen, S.-P.; Rantanen, J.; Minkkinen, P. *Chemometr Intell Lab* **2006**, *84*, 126–133.

10. Simon, L.; Oucherif, K.; Nagy, Z.; Hungerbuhler, K. *Chem Eng Sci* **2010**, *65*, 4983–4995.

11. Wan, J.; Ma, C.; Wang, X. *Particuology* **2008**, *6*, 9–15.

12. Presles, B.; Debayle, J.; Févotte, G.; Pinoli, J.-C. *J Electron Imaging* **2010**, *19*, 031207–031207–7.

13. Ahmad, O.; Debayle, J.; Gherras, N.; Presles, B.; Févotte, G.; Pinoli, J.-C. *J Electron Imaging* **2012**, *21*, 021115.

14. Jiang, S. An Examination of Sonocrystallization Kinetics of L-Glutamic Acid, University of Leeds, 2012.

15. Kacker, R.; Salvador, P. M.; Sturm, G. S.; Stefanidis, G. D.; Lakerveld, R.; Nagy, Z. K.; Kramer, H. J. *Crystal Growth & Design* **2016**, *16*, 440–446.

16. Hu, B.; Huang, K.; Zhang, P.; Zeng, X.; Han, Z.; Yu, S. *Sugar Tech* **2015**, *17*, 77–84.

17. Yin, D. C. *Prog Cryst Growth Ch* **2015**, *61*, 1–26.

18. Bhangu, S.; Ashokkumar, M.; Lee, J. *Crystal Growth & Design* **2016**, *16*, 1934–1941.

19. Jiang, M.; Papageorgiou, C.; Waetzig, J.; Hardy, A.; Langston, M.; Braatz, R. *Crystal Growth & Design* **2015**, *15*, 2486–2492.

20. Kee, N.; Tan, R.; Braatz, R. *Crystal Growth & Design* **2009**, *9*, 3044–3051.

21. Fujiwara, M.; Chow, P.; Ma, D.; Braatz, R. *Crystal Growth & Design* **2002**, *2*, 363–370.

Chapter 5

Image Analysis for In-Line Measurement of Multi-Dimensional Size, Shape and Polymorphic Transformation of L-glutamic Acid Using Deep Learning-Based Image Segmentation and Classification

5. Image Analysis for In-Line Measurement of Multi-Dimensional Size, Shape and Polymorphic Transformation of L-glutamic Acid Using Deep Learning-Based Image Segmentation and Classification

Abstract

In-situ tracking of the crystallization process through image segmentation has been developed and has encountered many challenges including improvement of in-situ images' quality, optimization of algorithms and increasing computation efficiency. In this study, a new method based on computer vision was proposed using the state-of-the-art deep learning technology to track crystal individuals. For the model compound L-glutamic acid (LGA), two polymorphic forms with different morphologies were segmented and classified during a seeded polymorphic transformation process. Information such as counts, size, surface area, crystal size distribution (CSD) and morphology of α- and β-form crystals were extracted for the individual crystals during the process. A comparative analysis was conducted with traditional process analytical technologies such as in-situ Raman and focus beam reflection measurement (FBRM). Results show high accuracy of segmentation and classification technique and reliable tracking of crystals evolution. The image processing speed of up to 10 frames per sec. (fps) makes the proposed approach suitable for in-situ tracking and control of crystallization and particulate processes. Our work in this study attempts to bridge the gap between the advanced imaging analysis technology that is available today and the specific needs of solution crystallization, to track, count and measure the individual crystals.

5.1. Introduction

Imaging in a crystallization process can be performed at two scales: one is using high-resolution technique on a molecular cluster level such as AFM, TEM, etc. to study the nucleation and growth mechanism of crystals. [1–3] The other is the imaging of bulk solution on a mesoscale level (micron to millimeter) to study the kinetics of nucleation and growth of crystals, monitor the crystal counts, crystal size, CSD, breakage, agglomeration etc. to control and optimize crystallization process. [4–6] In the process monitoring and optimization, imaging solution crystallization provides abundant information including

crystal morphology, crystal size, the degree of agglomeration, suspension density, crystal surface texture and multi-dimensional information of crystals. To improve the performance of real-time image analysis, great efforts have been invested in the design of in-situ cameras e.g. a flow cell camera device [7–9], stereo vision imaging system [6, 10–14], endoscopy–stroboscope [15–17], particle vision and measurement system (PVM, Mettler Toledo Inc.). In addition, the development of mathematical algorithms e.g. region-based segmentation (threshold, watershed), [18, 19] edge detection [20, 21] and clustering segmentation have advanced to some extent. Several papers studied the model compound LGA for crystals segmentation and classification, which realized the online imaging analysis and proved its feasibility of analyzing crystals evolution. [21-24] However, processing an image usually takes one to several seconds using traditional algorithms, and there is a big challenge in accuracy and transfer from a single image to conduct an in-situ analysis of the crystallization process.

For this purpose, we are motivated by a new image segmentation technology called Mask R-CNN (Regional Convolutional Neural Networks) which was released by FAIR (Facebook Artificial Intelligence Research) team in Oct. 2017. [25] Mask R-CNN is a state-of-the-art technology used in deep learning-based image analysis, which contains two stages: the first stage scans the image and generates proposals (areas likely to contain an object) with a light-weight neural network called Region Proposal Network (RPN) that reduces the detection scope and the computational load of the following stage. The second stage classifies and refines the proposals and generates pixel-wise masks. Mask R-CNN has been verified with high accuracy of classification and leads to a fast computation speed in various applications.[26-30] As shown in Figure 5-1, the objects were processed by the well trained neural network. Results were outputted as masks, bounding boxes, categories and the corresponding confidence limit for each object. Obviously, the Mask R-CNN recognizes and distinguishes (once trained) various objects such as a person, an elephant, a motorcycle, a bottle, etc., in addition to having the ability to segment overlapping objects and small objects in pixel-wise accuracy. Every object in the picture can be segmented and classified into corresponding categories and covered by a pixel-wise mask.
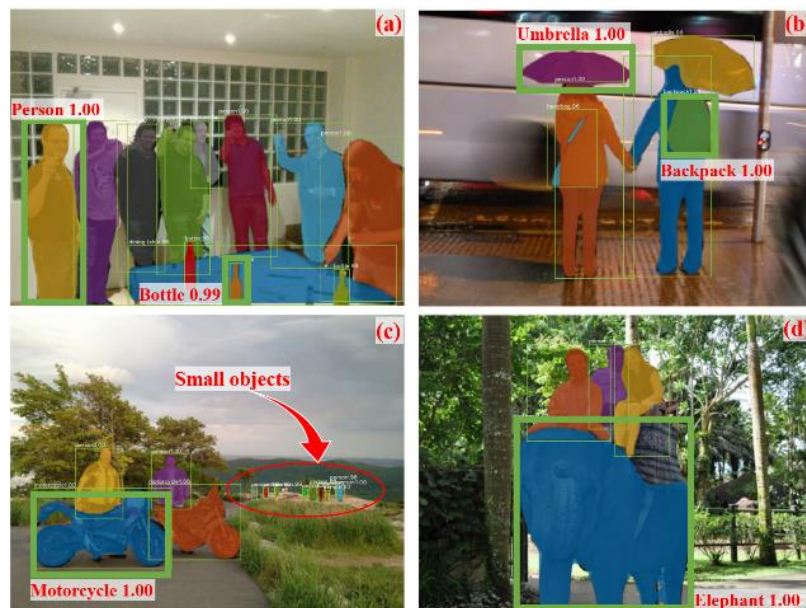
Figure 5-1: Mask R-CNN results on a test dataset. Results were outputted as a mask, bounding box, categories, and corresponding confidence. Figures were revised and reprinted with permission from reference [25]

In this study, we introduced Mask R-CNN to a microscopy field to analyze the solvent-mediated polymorphic transformation (SMPT) of LGA. Compared with traditional methods which usually take one to several seconds to process one image, an obvious improvement was achieved in the image processing step. The processing speed was accelerated up to 0.1 sec. per frame and a reliable segmentation of crystals (lower limit, 10 µm) and objects classification (α- and β-form crystals) were realized.

5.2.   Experimental Section

5.2.1.   Materials and Hardware

L-glutamic acid was purchased from Alfa Aesar (Ward Hill, MA) and used as received. Initial crystal form was β-form with purity 99+%. The α-form crystals were prepared by cooling crystallization in an aqueous solution and sieved to a size less than 355 µm. For the SMPT process, the saturated solution (equilibrium with α-form) with the concentration of 0.023 g/ml water was prepared at 45 °C. Then 3.0 g α-from crystal powder was added into 250 ml saturated solution in a double jacked crystallizer. In-situ Raman (Kaiser Optical Systems, Inc.), FBRM (S400, Mettler Toledo, USA) and the home-designed microscopy camera probe, as shown in Figure 5-2, were inserted in the crystallizer to monitor the SMPT

process. The camera probe used back laser lighting module coupled with an optical lens and a USB3.0 Vision Camera (Mako U-051B). The camera supports the maximum frame rate of 391 fps and the minimum exposure time of 44 microseconds. The captured pictures had a resolution of 800 × 600 with the pixel size of 1.3 μm × 1.3 μm. The β-form seeds were prepared through spontaneous SMPT at the same concentration (0.035 g/ml). The β-form crystal slurry was loaded as seeds at the 16th min with 2% percentage of the final β-from crystals' weight.
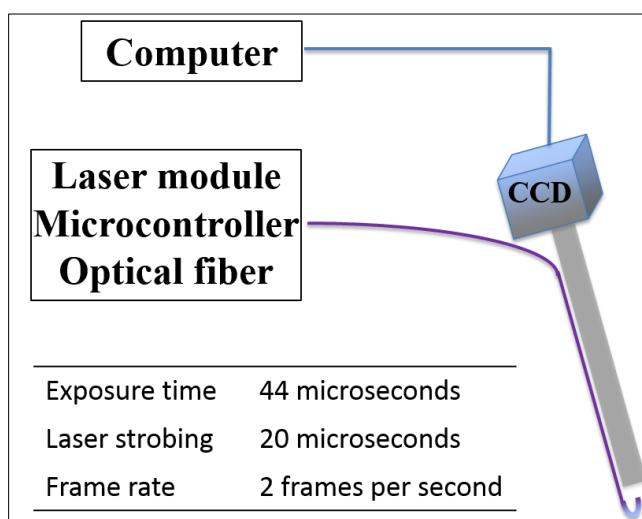
Figure 5-2: Schematic and specifications of home-designed camera probe

5.2.2. Implementation of Mask R-CNN

The implementation of this application and corresponding functions are listed in Table 5-1. In this application, we used the FAIR official Mask R-CNN implementation on the open-source framework Detectron (https://github.com/facebookresearch/Detectron), which is the state-of-the-art object detection system built on top of the deep learning framework – Caffe2. The parameters of the network were modified to enhance the detection. The training and inference were performed on a consumer hardware platform with i7-6700K CPU, 32GB DDR3 RAM, 256GB SSD, and GTX 1070 GPU. With the GPU acceleration, the training (Procedure 3) for 150K steps took 24 hours. The images processing speed was up to 10 fps. The training dataset is available on GitHub (https://github.com/wuyuanyi135/MicroVisionLabelling/tree/GlutamicAcidTransformation/Dataset).

Table 5-1: Implementation procedures of Mask R-CNN and corresponding functions

#	Procedures	Functions
1	Video recording	Record a video for the designed experiment
2	Labeling	Select images to label α- and β-form crystals for training
3	Training	Use the labeled images to train and valid the neural network
4	Images processing	Process the real-time video (images) and output masks
5	Masks processing	Extract information i.e. counts, size, surface area of every mask
6	Process analysis	Process and analyze process statistical data

5.3. Results and Discussions

5.3.1. Crystal Segmentation and Classification

As shown in Figure 5-3, the α- and β-form crystals of LGA which have prismatic and needlelike morphology, respectively, were segmented and classified by red and green masks during the SMPT process. Figure 5-3 (a) was captured at the initial stage which showed a very clear segmentation of α-form crystals. The masks were shown in the middle (masks overlaid) and right (masks only) column pictures. Figure 5-3 (b, c) represent the halfway and the ending stage performance of crystal segmentation and classification. As shown in Figure 5-3 (c), the deep learning-based segmentation can handle complex objects with overlapping, overexposure in a higher concentration. Several omissions can be found in Figure 5-3 (c), in addition to several mistakes like cutting and overlapping of crystals. It can be optimized by extending the training dataset and increase training steps to improve detection accuracy. The results of Mask R-CNN, in this case, were output as pixel-wise masks and the categories of crystal form would provide the necessary information to analyze the evolution of crystals in the SMPT process.
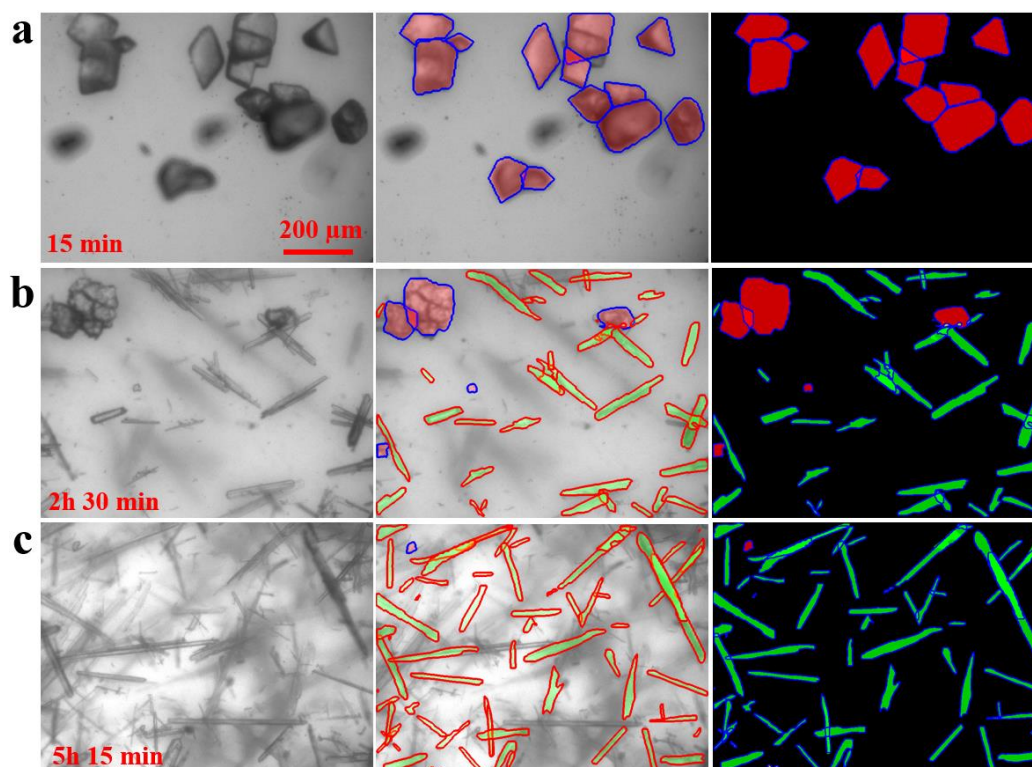
Figure 5-3: Mask R-CNN results on real-time tracking of polymorphic transformation. (a), (b) and (c) correspond to initial, halfway and end stage of the SMPT process. α- and β-form crystals were covered by red and green masks, respectively

5.3.2. Results Comparison with Traditional Technologies

For comparison, the SMPT process was first analyzed by other in-situ instruments including Raman and FBRM as well as offline measurement i.e. laser light scattering based CSDs of α- and β-form crystals. Results are shown in Figure 5-4, in which the data points of Figure 5-4 (a, b) were smoothed by averaging of 5 adjacent points. Figure 5-4 (a) shows the trends of FBRM counts of all crystals and square-weighted mean size against time. A sharp drop of mean size and a jump in crystal counts were noted at the time of seeding and then followed by a steady increase due to secondary nucleation and growth of β-form crystals. Compared with previous studies [31-33], the in-situ Raman monitoring of the seeded SMPT process, Figure 5-4 (b), indicates three stages, i: dissolving of α-form crystals (characteristic peak at 1010 cm^{-1}) and nucleation and growing of β-form crystals (characteristic peak at 970 cm^{-1}), ii: nucleation and growth of β form crystals that is driven by the difference in solubility of the two crystal forms, and iii: ripening of β-form crystals at steady state. The α-form crystals dissolved completely in the first stage. In Figure 5-4

(c), the counts-based chord length distributions (CLD) and square-weighted CLDs were plotted at the time points correlating to Figure 5-3. The α-form crystals powder and β-form crystals powder were measured by offline Malvern size analyzer, as shown in Figure 5-4 (d). The β-form crystals indicate bimodal distribution because of the breakage during the last stage of SMPT as well as the process of filtration, drying, and circulation of suspension in the measurement cell. The square-weighted CLDs agreed best with the mean particle size [34]. However, it could not show the needlelike morphology with a single broad peak. The bimodal counts-based CLD at 2h 30 min was caused by small crystals from secondary nucleation or attrition and breakage. At last, a broad distribution was shown both in CLD and squared weighted distribution. The FBRM is also limited to reflect the needlelike morphology during this process. At the end of this process, the focused beam scanning becomes difficult or has less probability to capture the chord length in the longer axis direction of the β-from crystals which have grown to hundreds of microns in length. Nevertheless, the real-time FBRM has been widely used both in industry and academic research because of its direct in-process measurement capability in a wide range of solids suspension densities.
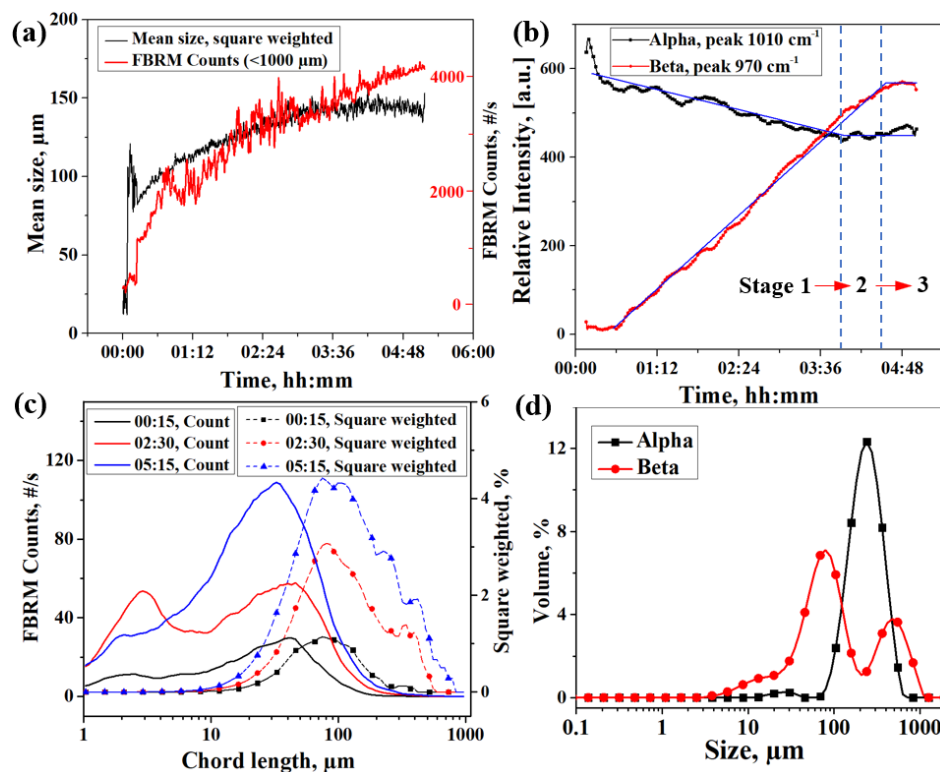
Figure 5-4: Monitoring of SMPT process of LGA, (a) mean size and crystal count measured by FBRM, (b) characteristic peaks tracking using *in-situ* Raman, (c) FBRM measured CSDs during transformation process, (d) Malvern Mastersizer measured CSDs of crystal powder before (α-form) and after (β-form) the transformation

5.3.3. Data Mining from Mask R-CNN Results

Image segmentation can extract more information about the crystals in a solution crystallization process. However, it still suffers from a number of bottlenecks including the accuracy and processing efficiency of images. The state-of-the-art deep learning-based object recognition applied to a microscopic field overcomes most of the challenges and provides further information such as classification, surface texture, breakage, agglomeration of the crystals. In this study, the crystal was not only successfully segmented but also classified into α- and β-forms (based on a significant morphology difference) and counted in number, size and surface area. The neural network was trained by more than two thousand labeled crystals in different stages of the SMPT process and resulted in a multi-dimensional dataset (counts, size, surface area, length and width of crystals). As shown in Figure 5-5, the SMPT process can be tracked by the counts of α- and β-form crystals. The counts were integrated from 120 images in one minute. The α-form crystals

completely dissolved at 3h 40 min that was implemented a little bit earlier than Raman tracking (3h 50 min). This was caused by the lower detection limit of about 10 µm. The counts of β-form crystals jumped at the 16th min corresponding to the loading of the seeds. The counts, as well as the area information (right y axis, calculated by pixels of mask, 1 pixel = 1.3 µm ×1.3 µm) of the two kinds of crystals, successfully reflected the three stages that proposed monitoring process by in-situ Raman. Compared with the crystal counts, the surface area of crystals reported a more accurate tracking. For α-form crystals, the baseline of counts is 45 which is 10% of its initial counts, while the baseline of surface area is 2.0 $\times 10^5$ µm^2 which are 4% of its initial surface area. The baseline is caused by false detection which can be fixed by extending the training dataset and increasing the training steps. The lower baseline of surface area tracking indicates that the detection errors mostly existed in the classification of small crystals. The breakage of β form crystals may have led to the error classification. In addition, the detection of counts and surface area of β-form crystals had a perfect overlap in the first stage. While the space between them in stages 2 and 3 was increased steadily. This is attributed to the attrition and breakage of β-form crystals because of a higher crystal concentration and bigger crystal size in the last stage. In contrast, the space between the curves of the counts and surface area of α-form crystals decreased with time. This is because the dissolution of big crystals in the initial stage resulted in a quick decrease of surface area but a slow reduction of counts. The data points in Figure 5-5 were smoothed by averaging of 5 adjacent points.
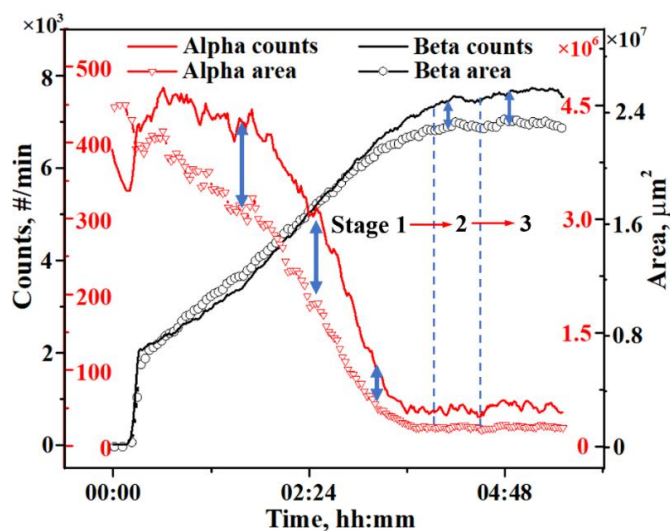
Figure 5-5: Measurement of crystals' counts and surface area of α- and β-form during the SMPT process

In Figure 5-6, crystal area distributions (CAD) corresponding to the square-weighting of FBRM readings were plotted as the surface area of α-and β-form crystals, respectively. Compared with the characteristic size of a crystal, especially for the needlelike shape, the surface area would be more representative to reflect the actual crystal size. Figure 5-6 (a, c) are statistical counts of α- and β-form crystals that correspond to a range of surface area bins, Figure 5-6 (b, d) are lognormal fitted curves of Figure 5-6 (a, c). For the dissolving of α-form crystals, the peak shifted to the left indicates the dissolving of big crystals. The red line at 5h 15 min is the detection error that caused by the misattribution of β- to α-form crystals in the final stage. The growth, as well as secondary nucleation, of β-form crystals, kept the peaks around at 1050 μm^2 with the increase of both big and small crystals, although it is not always centered at the same position. The mean value of surface area was tracked with time as shown in Figure 5-7. There is a consistent increase in the mean surface area before 1h 15 min, which indicates an obvious growth of β-form seeds. It was followed by a slow decrease till 3h 50 min. In addition to the increase of crystal density and growth of crystals, the secondary nucleation (attrition and breakage) of crystals played a dominant role in leveraging the mean surface area. Therefore, the mean area value decreased despite the growth of many crystals. In the last stage, a slight decrease of the mean surface area is noted after the supersaturation had been consumed because of the stirring induced breakage of big crystals.
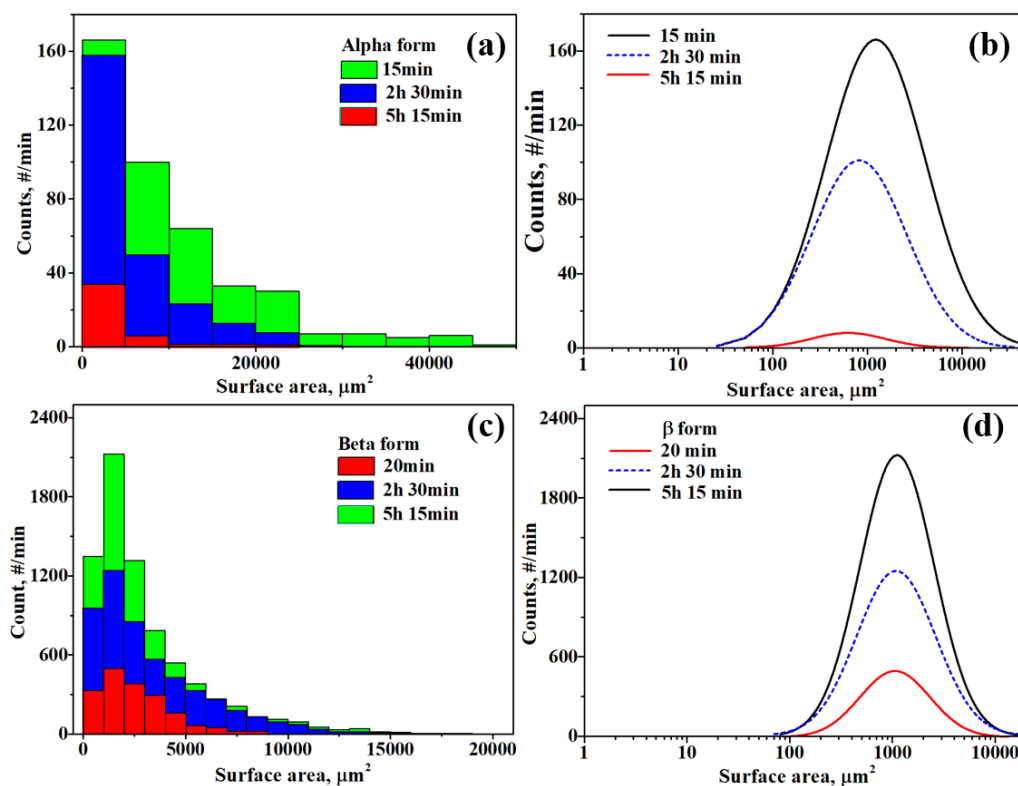
Figure 5-6: Crystal area distribution, (a) and (c) are counts of α- and β-form crystals corresponding to a range of surface area different size bins, (b) and (d) are lognormal fitted curves of (a) and (c)
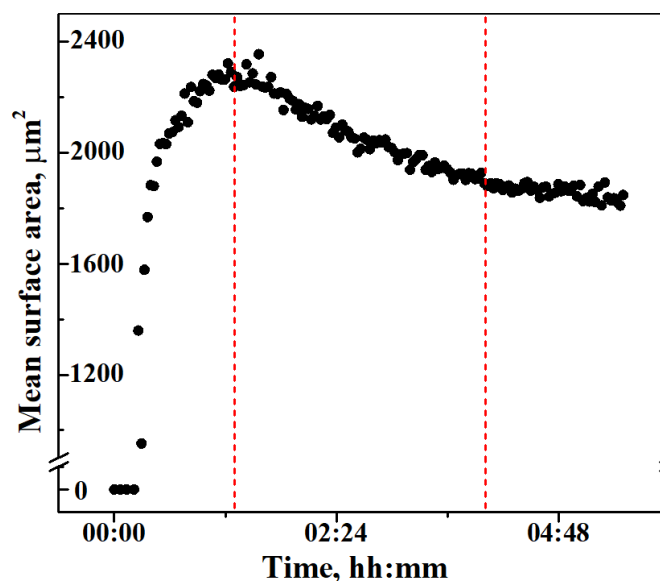
Figure 5-7: Mean surface area value change over time during the SMPT process

One of the main advantages of image analysis is the ability to extract multi-dimensional information from the crystallization process. For example, the needlelike crystals can be

detected in length and width. In this study, as shown in Figure 5-8 (a), every mask segmented by Mask R-CNN was fitted by an ellipse. Figure 5-8 (b) shows the examples of matching of crystals and ellipses. The ellipse's length in the x-axis direction was used as the characteristic size to analyze the CSDs of crystals. Instead of square-weighting, Figure 5-9 shows the direct statistical data of surface area versus crystal length and their corresponding fitted distributions of α- and β-form crystals, respectively. The data in Figure 5-9 (b, d) were lognormal distributions of probability density function (PDF) from Figure 5-9 (a, c), respectively. Unlike Figure 5-6 (b) in which the peak did not shift significantly, the distributions of surface area versus characteristic size (Figure 5-9 (a)) show an obvious dissolving of α-form crystals, and the peak moved from about 200 μm to 100 μm in Figure 5-9 (b). The unexpected surface area of the α-form crystals showed in the final stage due to false detection. For β-form crystals (Figure 5-9 (c, d)), there is an obvious growth of crystals in length compared the data at 20-min and 2h 30-min, but limited growth in length from 2h 30 min to 5h 15 min caused by attrition and breakage of crystals. Similar analysis along with crystal width (y-axis in Figure 5-8 (a)) can also be conducted to track the evolution of crystals in this direction. Compared with particle size monitoring by in-situ FBRM, Figure 5-4 (c), image analyses including Figure 5-6 and Figure 5-7 resulted in more information about the SMPT process like dissolving and growth of individual α- and β-form crystals.
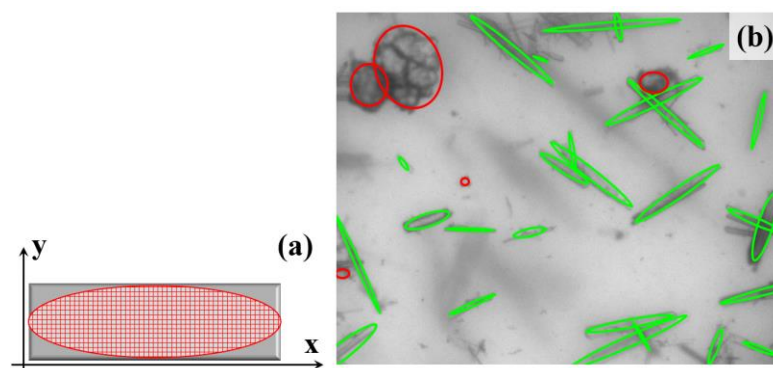
Figure 5-8: Schematic of elliptical matching of crystals (a), an example of matching of crystals and ellipses (b)
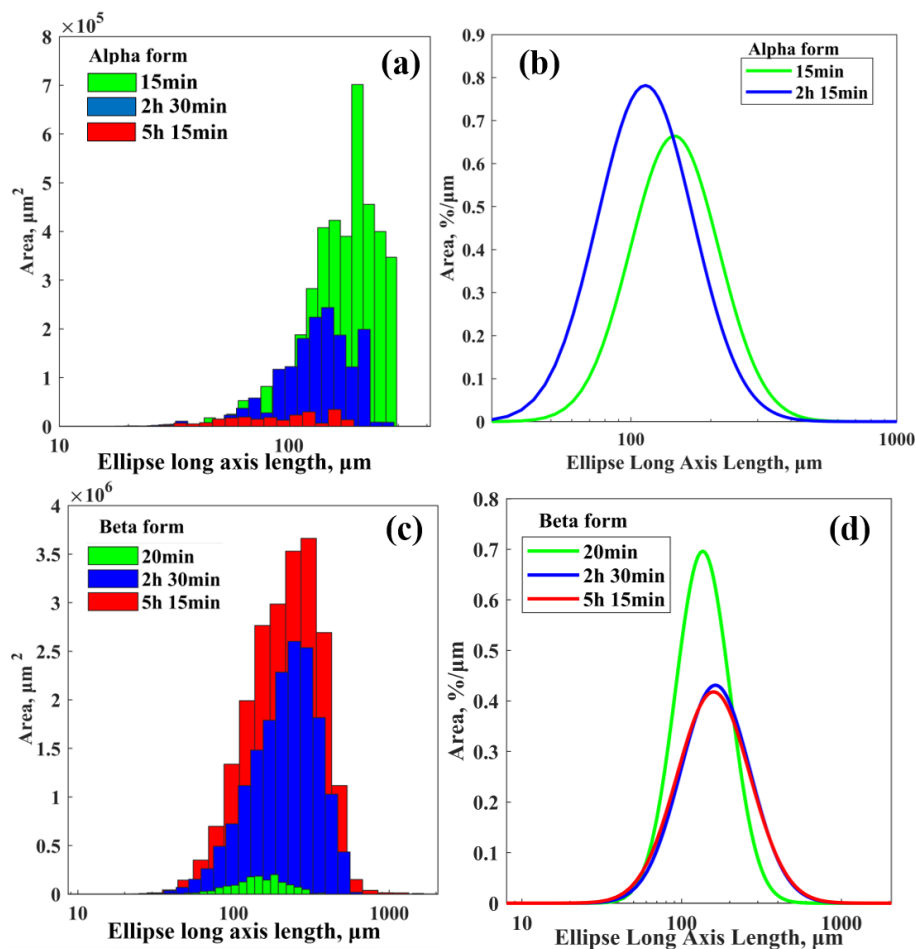
Figure 5-9: Surface area-based CSDs versus ellipse long axis length, (a) and (c) are statistical data of α- and β-form crystals at initial, halfway and end stages of the seeded SMPT process, (b) and (d) are fitted curves

Instead of chord length and square-weighting in FBRM, image analyses can provide the actual character size and the CAD data to calculate the process kinetics, e.g. dissolving rate, growth rate (for a specific face of crystal), size-dependent growth rate, and agglomeration. Therefore, the process simulation and optimization can be built from the image analysis in further steps. In addition, the polymorphic transformation monitoring based on image analysis is achievable only in the case that crystal form and its morphology have a one-to-one correspondence. This is due to some crystals exhibiting different morphologies of one polymorph, which makes it difficult for labeling and classification.

5.4.   Conclusions

Crystal segmentation was successfully realized using the state-of-the-art neural network, Mask R-CNN, in the SMPT process of LGA. Moreover, the segmented crystals were classified into two categories: α- (prismatic) and β-form (needlelike) crystals. The SMPT process was tracked by the change of crystal counts and surface area. Evolutions of α- and β-form crystals were analyzed by CAD and CSD in different stages, which showed more information in comparison to the *in-situ* FBRM. It is worth noting that the processing speed of images archived 10 fps in this study with a consumer GPU (NVIDIA GeForce GTX 1070), which makes it effective for real-time monitoring and analysis. While challenges always exist in the image capturing and processing for high crystals concentration. An in-process dilution module can be designed to enable in-situ imaging for most process solids suspension concentrations. Future improvement will be considered to enhance the labeling of the training dataset, which can help to improve the detection accuracy after extending the training dataset. For example, the image augmentation technique can be employed to extend the existing dataset by rotating, scaling, and adjusting the contrast of the images. For improving the detection limits, a high-quality camera would be recommended, and specific modification of neural network is required for adapting to the microscopic field.

5.5.   References

1. Dandekar, P.; Doherty, M. Imaging Crystallization. *Science* 2014, 344, 705–706.

2. Wu, S.; Yu, M.; Li, M.; Wang, L., Putnis, C. V.; Putnis, A. In-Situ Atomic Force Microscopy Imaging of Octacalcium Phosphate Crystallization and Its Modulation by Amelogenin's C-Terminus. *Cryst. Growth Des.* 2017, 17, 2194-2202.

3. Lupulescu, A. I.; Rimer, J. D. In-Situ Imaging of Silicalite-1 Surface Growth Reveals the Mechanism of Crystallization. *Science* 2014, 344, 729–732.

4. Simon, L. L.; Nagy, Z.; Hungerbuhler, K. Comparison of external bulk video imaging with focused beam reflectance measurement and ultra-violet visible spectroscopy for metastable zone identification in food and pharmaceutical crystallization processes. *Chem. Eng. Sci.* 2009, 64, 3344–3351.

5. Li, S.; Zhang, W.; Wang, L. Direct Nanoscale Imaging of Calcium Oxalate Crystallization on Brushite Reveals the Mechanisms Underlying Stone Formation. *Cryst. Growth Des.* 2015, 15, 3038–3045.

6. Kacker, R.; Maaß, S.; Emmerich, J.; Kramer, H. Application of inline imaging for monitoring crystallization process in a continuous oscillatory baffled crystallizer. *AIChE J.* 2018. Doi:10.1002/aic.16145.

7. Kempkes, M.; Vetter, T.; Mazzotti, M. Measurement of 3D particle size distributions by stereoscopic imaging. *Chem. Eng. Sci.* 2010, 65, 1362–1373.

8. Schorsch, S.; Vetter, T.; Mazzotti, M. Measuring multidimensional particle size distributions during crystallization. *Chem. Eng. Sci.* 2012, 77, 130–142.

9. Schorsch, S.; Ochsenbein, D.; Vetter, T.; Morari, M.; Mazzotti, M. High accuracy online measurement of multidimensional particle size distributions during crystallization. *Chem. Eng. Sci.* 2013, 105, 155–168.

10. Wang, X.; Roberts, K.; Ma, C. Y. Crystal growth measurement using 2D and 3D imaging and the perspectives for shape control. *Chem. Eng. Sci.* 2008, 63, 1173–1184.

11. Zhang, R.; Ma, C. Y.; Liu, J.J.; Zhang, Y.; Liu, Y. J.; Wang, X. Z. Stereo imaging camera model for 3D shape reconstruction of complex crystals and estimation of facet growth kinetics. *Chem. Eng. Sci.* 2017, 160, 171–182.

12. Wan, J.; Ma, C. Y.; Wang, X. Z. A method for analyzing on-line video images of crystallization at high-solid concentrations. *Particuology* 2008, 6, 9–15.

13. Huo, Y.; Liu, T.; Wang, X. Z.; Ma, C. Y.; Ni, X. W. On-line detection of particle agglomeration during solution crystallization by microscopic double-view image analysis. *Ind. Eng. Chem. Res.* 2017, 56, 11257-11269.

14. Anda, J. C. D.; Wang, X. Z.; Roberts, K. J. Multi-scale segmentation image analysis for the in-process monitoring of particle shape with batch crystallisers. *Chem. Eng. Sci.* 2005, 60, 1053–1065.

15. Simon, L. L.; Merz, T.; Dubuis, S.; Lieb, A.; Hungerbuhler, K. In-situ monitoring of pharmaceutical and specialty chemicals crystallization processes using endoscopy–stroboscopy and multivariate image analysis. *Chem. Eng. Res. Des.* 2012, 90, 1847–1855.

16. Simon, L. L.; Nagy, Z. K.; Hungerbuhler, K. Endoscopy-based in-situ bulk video imaging of batch crystallization processes. *Org. Process Res. Dev.* 2009, 13, 1254–1261.

17. Gao, Z.; Zhu, D.; Wu, Y.; Rohani, S.; Gong, J.; Wang, J. Motion-Based Multiple Object Tracking of Ultrasonic-Induced Nucleation: A Case Study of L-glutamic Acid. *Cryst. Growth Des.* 2017, 17, 5007-5011.

18. Sarkar, D.; Doan, X. T.; Ying, Z.; Srinivasan, R. In-situ particle size estimation for crystallization processes by multivariate image analysis. *Chem. Eng. Sci.* 2009, 64, 9–19.

19. Arnaout, T. E.; Cullen, P. J.; Sullivan, C. A novel backlight fiber optical probe and image algorithms for real-time size-shape analysis during crystallization. *Chem. Eng. Sci.* 2016, 149, 42–50.

20. Huo, Y.; Liu, T.; Liu, H.; Ma, C. Y.; Wang, X. Z. In-situ crystal morphology identification using imaging analysis with application to the L-glutamic acid crystallization. *Chem. Eng. Sci.* 2016, 148, 126–139.

21. Lu, Z. M.; Zhu, F. C.; Gao, X. Y.; Chen, B. C.; Gao, Z. G. In-situ particle segmentation approach based on average background modeling and graph-cut for the monitoring of l-glutamic acid crystallization. *Chemom. Intell. Lab. Syst.* 2018, 178, 11-23.

22. Anda, J. C. D.; Wang, X. Z.; Lai, X.; Roberts, K. J.; Jennings, K. H.; Wilkinson, M. J.; Watson, D.; Roberts, D. Real-time product morphology monitoring in crystallization using imaging technique. *AIChE J.* 2005, 51, 1406-1414.

23. Anda, J. C. D.; Wang, X. Z.; Roberts, K. J. Multi-scale segmentation image analysis for the in-process monitoring of particle shape with batch crystallisers. *Chem. Eng. Sci.* 2005, 60, 1053-1065.

24. Anda, J. C. D.; Wang, X. Z.; Lai, X.; Roberts, K. J. Classifying organic crystals via in-process image analysis and the use of monitoring charts to follow polymorphic and morphological changes. *J. Process Control* 2005, 15, 785-797.

25. He, K. M.; Gkioxari, G.; Dollár, P.; Girshick, R. Mask R-CNN. In Computer Vision (ICCV), 2017 IEEE International Conference, 2017, 2980-2988, DOI: 10.1109/ICCV.2017.322.

26. Bruno, A. E.; Charbonneau, P.; Newman, J.; Snell, E. H.; So, D. R.; Vanhoucke, V.; Watkins, C. J.; Williams, S.; Wilson, J. Classification of crystallization outcomes using deep convolutional neural networks. *arXiv preprint* 2018, arXiv:1803.10342.

27. Christiansen, E. M.; Yang, S. J.; Ando, D. M.; Javaherian, A.; Skibinski, G.; Lipnick, S.; Mount, E.; O'Neil, A,; Shah, K.; Lee, A. K,; Goyal, P.; Fedus, W.; Popin, R.; Esteva, A.; Berndl, M.; Rubin, L. L.; Nelson, P.; Finkbeiner, S. In Silico Labeling: Predicting Fluorescent Labels in Unlabeled Images. *Cell* 2018, 173, 792–803.

28. Ziatdinov, M.; Dyck, O.; Maksov, A.; Li, X.; Sang, X.; Xiao, K.; Unocic, R. R.; Vasudevan, R.; Jesse, S.; Kalinin, S. V. Deep Learning of Atomically Resolved Scanning Transmission Electron Microscopy Images: Chemical Identification and Tracking Local Transformations. *ACS Nano* 2017, 11, 12742−12752.

29. Staker, J.; Marshall, K.; Abel, R.; McQuaw, C. Molecular Structure Extraction From Documents Using Deep Learning. *arXiv preprint* 2018, arXiv:1802.04903.

30. Johnson, J. W. Adapting Mask R-CNN for Automatic Nucleus Segmentation. *arXiv preprint* 2018, arXiv:1805.00500.

31. Ono, T.; Horst, J. H.; Jansens, P. J. Quantitative measurement of the polymorphic transformation of L-glutamic acid using in-situ Raman spectroscopy. *Cryst. Growth Des.* 2004, 4, 465-469.

32. Schöll, J.; Bonalumi, D.; Vicum, L.; Mazzotti, M. In-situ monitoring, and modeling of the solvent-mediated polymorphic transformation of L-glutamic acid. *Cryst. Growth Des.* 2006, 6, 881-891.

33. Cornel, J.; Christian L.; Mazzotti, M. Experimental characterization and population balance modeling of the polymorph transformation of L-glutamic acid. *Cryst. Growth Des.* 2009, 9, 243-252.

34. Yu, W.; Erickson, K. Chord length characterization using focused beam reflectance measurement probe-methodologies and pitfalls. *Powder Technol.* 2008, 185, 24–30.

Chapter 6

Ultrasonic Irradiation and Seeding to Prevent Metastable Liquid-Liquid Phase Separation and Intensify Crystallization

6. Ultrasonic Irradiation and Seeding to Prevent Metastable Liquid-Liquid Phase Separation and Intensify Crystallization

Abstract

During the crystallization of complex pharmaceutical molecules, a liquid-liquid phase (LLP) separation phenomenon may occur that could hinder crystallization processes and adversely affect the crystal quality and process robustness. In this study, the LLP separation behavior of a vanillin and water mixture was investigated using a hot-stage microscope and a cooling crystallization process. Thermodynamic stability of phases and the crystallization phase diagram including the metastable zone width, nucleation, and LLP separation were developed. The impact of ultrasound and seeding on LLP separation was investigated and used to optimize the crystallization process. Our results show that the LLP separation may exist in both the stable and metastable zones of the crystallization phase diagram. Ultrasound can effectively promote nucleation, narrow the metastable zone of LLP separation, and inhibit LLP separation within the concentration range of 3.8-4.8 g/100 g water. Moreover, ultrasonic crystallization was optimized to produce small, uniformly sized crystals in a reproducible manner, whereas seeding crystallization was able to grow larger crystals without obvious agglomeration. In the case of a vanillin aqueous solution, both the ultrasonic induced and seeding crystallization strategies were able to prevent LLP separation and improve process performance. These results would be of significant use in the crystallization of other pharmaceutical molecules in which LLP separation occurs.

6.1.   Introduction

Liquid-liquid phase (LLP) separation involves separating a liquid mixture into two liquid phases by changing the mixture's temperature, pressure, or composition. The LLP separation is normally enthalpy-driven to form a dense and a dilute liquid phase with differences in composition and density [1]. Many studies have been reported on the mechanisms and applications of the LLP separation phenomenon in colloidal systems, proteins and polymer solutions [2–4]. With the increase in the molecular weight of pharmaceutical molecules, the LLP separation phenomenon has become more of a

common occurrence in the study of pharmaceutical crystallization processes, which is also referred to as the oiling out process or phase demixing [5–10].

The LLP separation phenomenon is usually not desired in pharmaceutical crystallization which requires robust, high-efficiency processes and tight control over the crystal purity and morphology. Several studies reported the effect of LLP separation (oil droplets) on crystallization processes. Veesler *et al.* reported an LLP separation system and concluded that the changes of composition, supersaturation, and viscosity in both liquid phases hindered the crystallization process and required a long time to reach equilibrium [11]. Ten Wolde *et al.* proposed that the nucleation rate increases by many orders of magnitude in the presence of metastable LLP separation [12]. In this case, a dense fluid cluster formed before nucleation, which corresponded to the theory of two-step nucleation mechanism [13]. Du *et al.* compared the crystal products with and without LLP separation in crystallization processes and indicated a lower purity and yield in the presence of LLP separation [14]. Albuquerque *et al.* and Lu *et al.* studied the phase diagram with the metastable zone of LLP separation and designed a crystallization trajectory to avoid LLP separation [8, 15]. Instead of avoiding LLP separation, Takasuga *et al.* found out that the LLP separation crystallization favored formation of large size crystals and higher yield [16, 17]. Veesler *et al.* and Bonnett *et al.* took advantage of the formation of oil droplets, and successfully prepared spherical agglomerated particles, which can improve downstream processing for some systems [18, 19]. Moreover, Ilevbare *et al.* pointed out that the LLP separation of poorly soluble drugs could benefit solubility enhancing formulation [20]. Therefore, the design and optimization of a crystallization process in the presence of a metastable LLP separation are highly dependent on the characteristics of the compound.

In this research, the crystallization process of vanillin in aqueous solution was investigated. It has been shown that the crystal products have better quality in direct crystallization processes compared to an LLP separation process [14]. To prevent the occurrence of the metastable LLP separation, ultrasonic irradiation was used, for the first time to the best of our knowledge, to optimize the crystallization process. Many studies have proven that ultrasound can promote nucleation and narrow metastable zone width (MZW) in aqueous solutions [21–23]. The collapse of cavitation bubbles generated by ultrasound can induce spontaneous nucleation and break up crystals for further growth. Based on this

consideration, the effect of ultrasound irradiation on metastable LLP separation was examined. Albuquerque *et al.* developed a crystallization trajectory to avoid LLP separation in the mixture of vanillin and water [8], where the operating range was limited to a low concentration range which diminished process efficiency. Ultrasonic crystallization is expected to expand the operation range to improve process robustness, efficiency as well as product quality. In addition, seeding as one of the most widely used techniques in industrial crystallization was used to suppress LLP separation. Via a controlled seeding strategy, LLP separation could be prevented to optimize a crystallization process [15, 24–26]. Different seeding recipes were evaluated by in-situ focused beam reflectance (FBRM) probe and offline crystal size analysis.

First, using hot-stage microscopy, the dissolution, and LLP separation phenomena during heating and cooling cycles were tracked, respectively. Then, the phase diagram was measured to investigate the effect of ultrasound on preventing LLP separation. The design of ultrasonic crystallization will be discussed in this section. Third, the seeding technique was examined to prevent LLP separation and optimize the crystallization process. Finally, conclusions were drawn to evaluate the effect of ultrasonic crystallization and seeding strategy in the LLP separation system.

6.2.   Experimental Section

6.2.1.   Materials

Vanillin (molecular formula $C_8H_8O_3$) is a phenolic aldehyde with melting point 81-83 °C. It was purchased from Sigma-Aldrich (St. Louis, MO, USA) with 99+% purity and used without further purification. Distilled water was used as the solvent in the crystallization experiments.

6.2.2.   Hot-stage Microscopy

Thermal microscopic experiments were performed on a Zeiss Axioskop-40 microscope (Zeiss, Thornwood, NY) using a Linkam hot-stage (LTS 350, Linkam Scientific, Tadworth, Surrey, UK). The temperature was controlled by a TMS 94 temperature controller with a precision of 0.1 °C. Samples with the concentration of 4.8 g/100 g water were heated up to 65 °C and then cooled down until the crystallization occurred with a

constant rate of 0.1°C/min. The micrographs were recorded every second using the software Eclipse and MATLAB (version 2017b) at 50× and 500× magnification. Several experiments were carefully conducted to capture the onset of nucleation with the existence of oil droplets.

6.2.3.   Phase Diagram Measurement

The solubility of vanillin in pure water over a temperature range from 20 to 81 °C was measured dynamically by using FBRM technology (S400, Mettler Toledo, USA). A certain amount of vanillin (0.3-7.3 g, with increments of 0.5 g, ± 0.001 g), was added into a double jacketed crystallizer holding 50 ± 0.01g water. Then, the FBRM was used to monitor the particle counts during heating. The detection range of FBRM is over the chord length of 0.1 to 1000 microns. A constant heating rate of 0.2 °C/min was used by Julabo FT50 (±0.01 °C) constant temperature water heater. A clear solution monitored by FBRM counts was recorded as the saturation temperature. Correspondingly, to measure the width of the metastable zone, a sharp increase in FBRM counts was designated as the onset of nucleation or LLP separation process, during the cooling down of the solution (0.2 °C/min) [27]. The heating/cooling loop was repeated at least three times until a consistent result was obtained at each concentration and the averaged data, as well as corresponding standard deviation, were reported in the measurements.

6.2.4.   Ultrasonic Crystallization

A VCX 500 ultrasonic processor (Sonic and Materials Inc.) was used to generate ultrasonic irradiation in the crystallization process. The frequency of the processor was 20 kHz and the energy input was set at 20 watts per 50g water. Three kinds of operation methods were utilized in the optimization of the crystallization process: initial irradiation, pulsed and continuous ultrasonic irradiation. The ultrasound was stopped once the nucleation was detected while using initial ultrasonic crystallization. The pulsed ultrasonic crystallization was conducted with an interval of 30 seconds in between pulses. The processes were monitored by FBRM and then the products were dried (45°C, 12h, Yamoto DKN 400 Constant Temperature Oven) and analyzed by Malvern 2000 (Malvern Instruments Ltd. UK) for size distribution. Consideration should be given to control the temperature while using ultrasound irradiation, and space should be kept between the FBRM and ultrasound

probes in the crystallizer to reduce the impact of bubbles, produced by the ultrasound, on the FBRM tracking. Otherwise, the ultrasound would disable the detection of FBRM and interfere with the measurement process [23].

6.2.5.   Seeding Crystallization

Seeding crystallization was optimized by varying the time of seed addition i.e. before or after LLP separation. The seeds were dry-milled powder and a certain amount of seeds (1 wt %) were fed to trigger nucleation. The optimization processes were recorded by a microscope as well as in-situ FBRM. Finally, the crystal products were characterized by Malvern 2000 to determine the CSD.

6.3.   Results and Discussion

6.3.1.   Hot-stage Microscopy Monitoring

Svärd *et al.* reported a molten hydrate around 51 °C upon heating the mixture of vanillin and water [28]. The melting point of pure vanillin ranges from 81 to 83 °C. The vanillin water mixture differs from pure vanillin, and here the two liquid phases are in equilibrium. Our results agree with the above reports and that the aqueous solution of vanillin exhibits an LLP separation during the crystallization process with a metastable LLP separation zone [29]. The stable and metastable two liquid phases were captured using hot-stage microscopy upon heating and cooling, respectively. The solution with a concentration of 4.8 g/100 g water was selected to track the phase transition. As shown in Figure 6-1, on the second cycle of heating/cooling, *a*, *b* and *c* displayed the melting process during heating up. Instead of dissolving into the water directly, the vanillin formed the dihydrate first which has a melting point around 51 °C, and then the second liquid phase appeared in the solution. The oil droplet in Figure 6-1 *c* is a molten dehydrate, which is the discontinuous phase in the bulk solution. Finally, the molten hydrate would dissolve with further heating and a clear solution would be obtained at the saturation temperature.
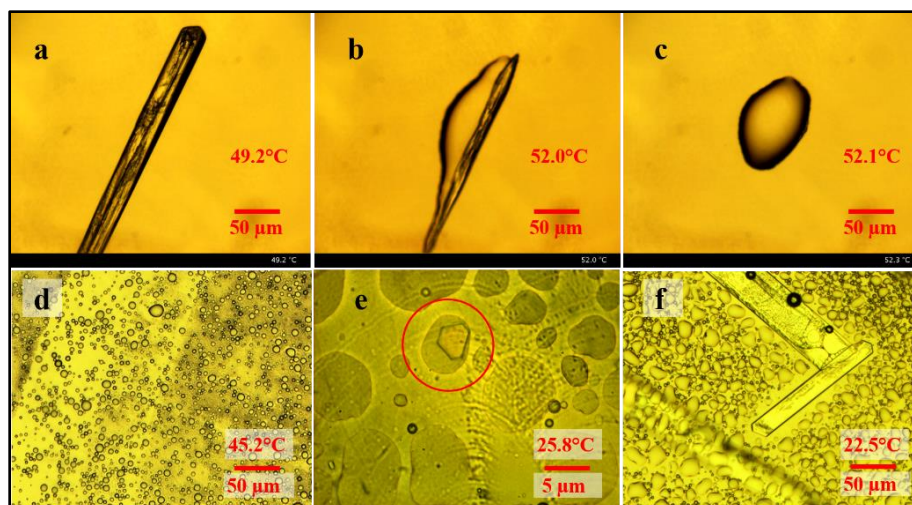
Figure 6-1: In-situ microscope graphs of molten dihydrate during heating up (*a, b, c*) and metastable two liquid phases and crystallization during cooling down (*d, e, f*)

Upon cooling down (Figure 6-1, *d, e, f*), the clear solution started LLP separation around 45.5 °C which is already in the metastable zone for the existence of two liquid phases. The oil droplets were very small (1~2 microns) at the beginning and then gradually grew bigger. During the cooling period, the droplets tended to coalesce into larger droplets, which is consistent with other reports [25]. However, in the case of vanillin and water mixture, we found that nucleation occurred in the oil droplets first, which differs from a previous study reporting that the nucleation occurred in the continuous liquid phase [30]. As shown in Figure 6-1 *e*, the crystals were first observed inside the oil droplets (shown by a red circle) and grew inside the droplets. Crystals then grew out of the oil droplets at the expense of the supersaturated solute in the continuous phase and adjacent droplets (Figure 6-1 *f*). During this process, secondary nucleation (i.e. needle breeding) may have happened in the hot-stage cell as well as in bulk solution with agitation. The difference between our observation and previous work [30] may be attributed to the rapid growth rate of crystals, which makes it hard to capture the starting point of nucleation. The operation trajectory of hot-stage experiments is highlighted in the phase diagram shown in Figure 6-4 *b*.

6.3.2. Phase Diagram Measurement

For consistency in the measurement of the phase diagram data, FBRM technology was used to measure the solubility curve first. The FBRM offers a good choice for the measurement of metastable zone width and the further optimization of crystallization.

Figure 6-2 shows the examples of measuring saturation temperature, LLP separation point and the onset of nucleation in the oil droplets. As we can see in Figure 6-2 *a*, there is a clear drop in the total counts by FBRM at the saturation temperature T_{C0} with a concentration of 2.8 g/100 g water. In Figure 6-2 *b*, a jump of total counts by FBRM was observed when LLP separation occurred during the cooling process. As temperature decreased, the oil droplets merged together slowly, corresponding to a decrease of total counts by FBRM and an increase of the mean size. This was followed by a sharp jump in the mean size and a drop of total counts by FBRM that correspond to the transition of oil droplets to crystals. The nuclei burst out of the oil droplets and agglomerated together, inducing a jump in the mean size. The measured data (Figure 6-3) without ultrasound agree with the reported solubility data (15-50 °C) and the metastable zone width (15-35 °C) [30, 31]. Figure 3 shows the phase diagram during cooling crystallization process with and without ultrasound irradiation. Accordingly, the thermodynamic phase diagram is drawn in Figure 6-4, in which the stable and metastable zones are highlighted to illustrate the operation limitation of ultrasound irradiation.
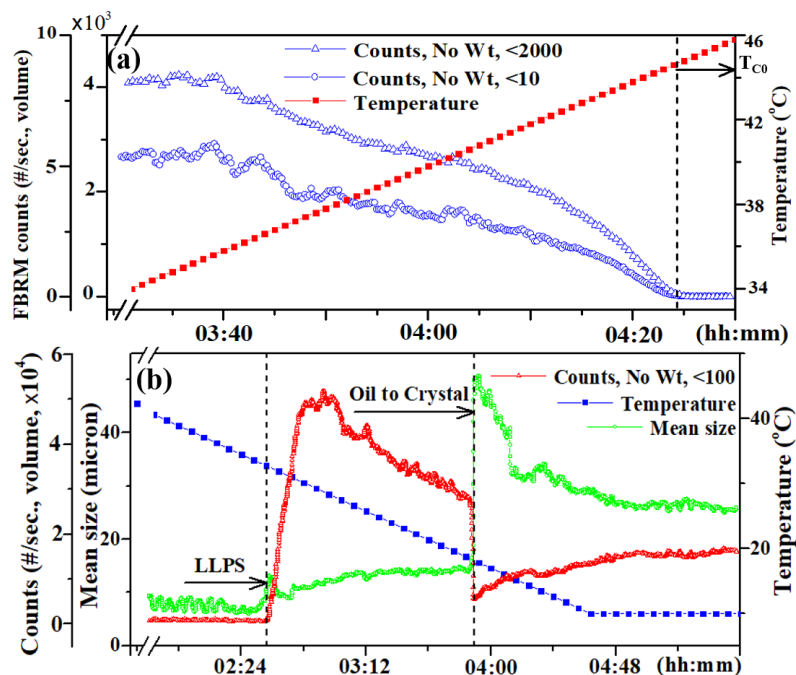
Figure 6-2: Phase diagram measurement examples using FBRM. (a) Heating up to determine the saturation temperature T_{C0} of the solution 2.8 g/100 g water, (b) Cooling down to determine LLP separation temperature and corresponding nucleation temperature of the solution 4.2 g/100 g water
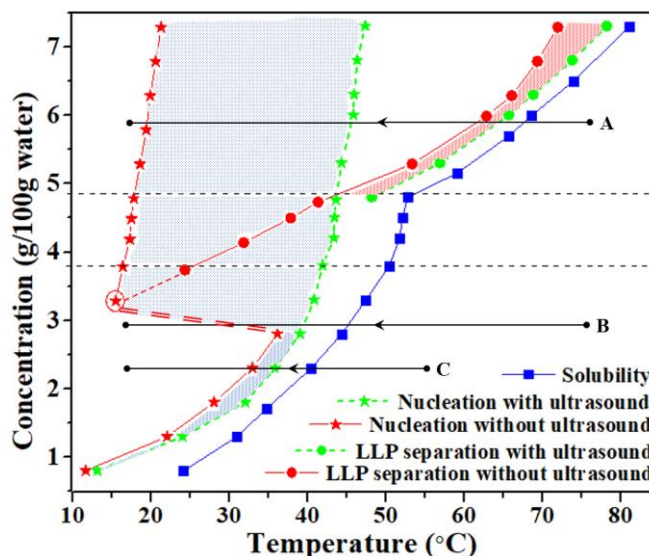
Figure 6-3: Crystallization phase diagram during the cooling crystallization process. (1) Solubility curve in blue, (2) Metastable zone with ultrasound in green, LLP separation curve with circle and nucleation curve with star, (3) Metastable zone without ultrasound in red, LLP separation curve with circle and nucleation curve with star

As shown in Figure 6-3, the solubility curve and the metastable zones width with and without ultrasound ranges from 20 to 81 °C. The data points in Figure 6-3 are reported in the appended Table 0-2 including standard deviation. Without using ultrasound, there are three regions in the metastable zone: direct nucleation (below 2.8 g/100 g water), LLP separation nucleation (above 3.8 g/100 g water) and in the middle, competition between LLP separation and direct nucleation. In the LLP separation nucleation region, LLP separation occurs first and then is followed by nucleation along with decreasing of temperature. When the solution was cooled down with a high concentration (e.g. point A), an undercooled liquid phase was formed as a metastable state which can be explained by Ostwald's rule [7, 32]. Compared with a lower concentration that would be obtained without LLP separation (e.g. point C), the onset of nucleation was hindered by oil droplets, resulting in a sluggish crystallization process. The competition between LLP separation and direct nucleation in the middle concentration range was found to be of notable significance. The LLP separation did not occur at the concentration of 3.3 g/100 g water, while its nucleation onset was 16.5 °C which is much lower than the direct nucleation region (i.e. 2.8 g/100 g water with a nucleation onset temperature of 38.0 °C). A possible reason is that the concentration 3.3 g/100 g water is right on the crossover point of the extensions of LLP separation (red dashed line) and nucleation curves as labeled in Figure

6-3. There is an equilibrating competition between the two, however, nucleation overcomes LLP separation. Several experiments were performed in the concentration range 2.8 and 3.3 g/100 g water demonstrating large errors in the measurements (shown with dashed line in Figure 6-3 and Figure 6-4), due to the discontinuity in the nucleation curves. Nevertheless, the mechanism at a molecular level is still unclear. The solvent properties (polarity, hydrogen-bond character etc.), the functional groups of the solute compound, as well as the forces between solvent-solute molecules and solute-solute molecules are generally recognized as the competitive factors during this process.

Using ultrasound, the cooling crystallization process was intensified in three ways: i-narrowing the nucleation metastable zone (blue shading in Figure 6-3), ii- narrowing the LLP separation metastable zone (red shading in Figure 6-3), and iii- preventing the LLP separation process (between two lines at 3.8 and 4.8 g/100 g water in Figure 6-3). The upper limit of direct nucleation improved from 3.8 to 4.8 g/100 g water, while using ultrasonic crystallization. To quantify the effectiveness of ultrasound, the metastable zone of nucleation ΔT_{max} and LLP separation $\Delta T_{max,1}$ can be calculated by:

$$\Delta T_{max} = T^* - T_{nuc} \tag{6-1}$$

$$\Delta T_{max,1} = T^* - T_{oil} \tag{6-2}$$

Where T^* is the solubility temperature, T_{nuc} and T_{oil} represent the nucleation and LLP separation temperatures, respectively, at a certain concentration. Using points A and C as an example, the effect of ultrasound is shown in Table 6-1. The ultrasound irradiation narrowed more than 50% the MSZW for nucleation and almost half for LLP separation. Moreover, ultrasonic irradiation can clearly prevent LLP separation and improve the oiling limit from 3.8 to 4.8 g/100 g water. Thus, ultrasonic crystallization expanded the operation region and made room for improving process efficiency and robustness.

Table 6-1: Effectiveness of ultrasound on metastable zones of nucleation and LLP separation

Concentration	ΔT_{max}		$\Delta T_{max,1}$	
	with/without ultrasound, °C	Zone percentage	with/without ultrasound, °C	Zone percentage
Point A in Figure 3, 5.8 g/100g water	19.8/47.4	41.2%	0.7/1.3	53.8%
Point C in Figure 3, 1.8 g/100g water	2.7/6.7	40.3%	NA	NA
Note: There is no LLP separation for point C, 'NA': not available				

From the results discussed above, can LLP separation be completely eliminated by ultrasound irradiation? Can the phase diagram be changed using ultrasound irradiation and what are its limitations? The answers are illustrated in Figure 6-4, which is the thermodynamic phase diagram of vanillin aqueous solution with highlighted metastable zones in the cooling crystallization process. The fitted equations of the curves in Figure 6-4 and corresponding R-squared value are listed in the appended Table 0-3. It is obvious that external forces are not able to change the thermodynamic stable zone (i.e. L_1+L_2 in Figure 6-4 ***a***). Where L_1 represents the continuous liquid phase and L_2 is the dispersed phase. A conclusion can be drawn that the shaded area is the effective zone for ultrasound irradiation. In fact, the ultrasonic irradiation acted as a vigorous agitation method to speed up the process to reach steady state. As shown in Figure 6-4 ***a***, compared with the metastable zone within the red curves, the ultrasound had greatly narrowed the metastable zone in blue shading. The competition between LLP separation and nucleation is shown with dashed line. The enlarged zone in Figure 6-4 ***b*** indicates the limitations of ultrasound effectiveness and the hot-stage experimental trajectory. When cooling down, the solution would go through metastable L_1 or $L_1 + L_2$ zones. If the input energy of ultrasound is

increased continually, the MSZW will be narrowed further, while it will never cross the boundary between L_1+S and L_1 or L_1+L_2.
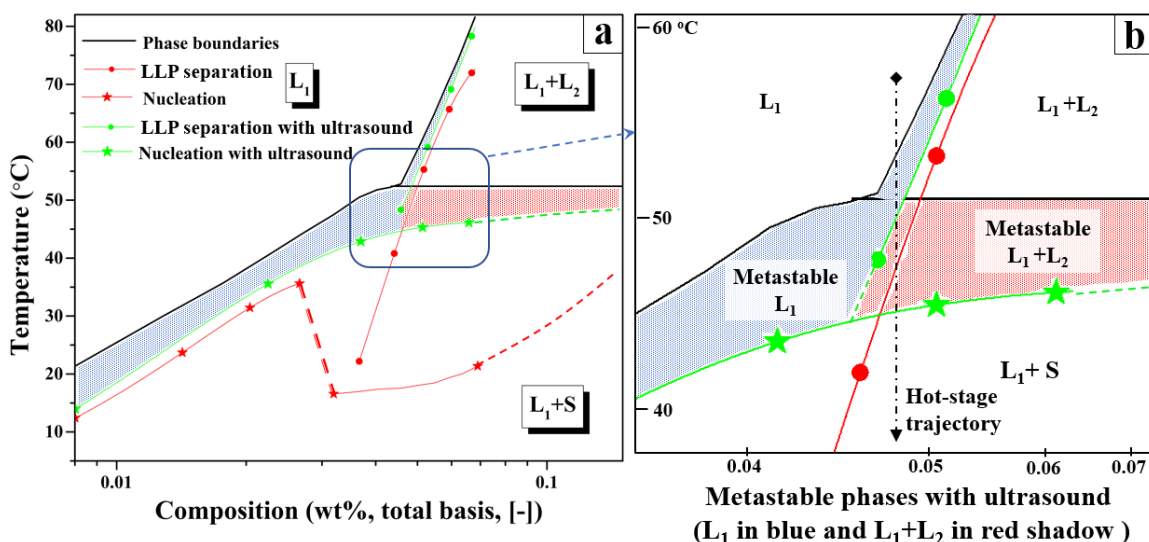
Figure 6-4: Thermodynamic phase diagram of vanillin and water mixture. (1) Black curves are stable phase's boundaries; (2) green curves are ultrasonic metastable zone limits; (3) Red curves are metastable zone without ultrasound; (4) Dashed lines are extensions of the fitted curves

6.3.3.   Crystallization Process Optimization Using Ultrasound and Seeding

6.3.3.1. Ultrasonic crystallization

As shown in Table 6-2, three kinds of implementing ultrasound irradiation were considered: initial irradiation, pulsed and continuous ultrasonic irradiations to optimize the crystallization processes [33,34]. For consistency, the intensity of ultrasound was used as 20 watts per 50 g water throughout the experiments. In general, big crystals are preferred to benefit downstream processing of crystals. The initial and pulsed ultrasonic crystallization is usually used to produce big crystals. Under such conditions, the vanillin crystals are plate or needlelike and prone to agglomeration while the ultrasound irradiation is stopped. Instead of pursuing big crystals, continuous ultrasonic crystallization was used to produce small, uniformly sized crystals without obvious agglomeration. Small particles have the potential to increase the dissolution rate and the saturated solubility which could benefit poorly soluble drugs [35].

Table 6-2: Schematic of ultrasonic crystallization and performed experiments

Schematic of ultrasonic crystallization	Ultrasonic crystallization Run #
	Initial ultrasound Run #1
	Pulsed ultrasound Run #2
	Continuous ultrasound Run #3
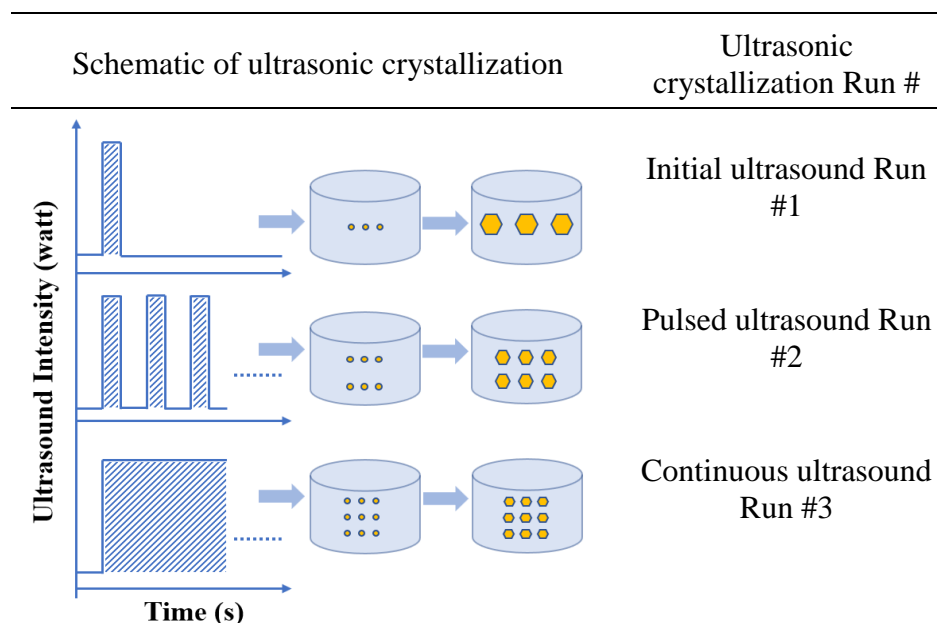
Figure 6-5 monitors the continuous ultrasonic crystallization process at an initial concentration of 4.2 g/100 g water, which results in LLP separation and hinders nucleation without ultrasound. Figure 6-5 *a* shows that ultrasonic irradiation could help generate more nuclei ($\times 10^4$) than seeding or direct nucleation without ultrasound ($\times 10^3$). The squared-weighted chord length distribution can reflect the dynamic growth of crystals [36], as shown in Figure 6-5 *b*. The size distribution was nearly unchanged, and the number of crystals increased during the cooling down period. New crystals were generated during the cooling process at the expense of supersaturation. The ultrasound irradiation generated cavitation to break crystals and promote secondary nucleation and help to prevent agglomeration of crystals at high surface tension [37]. Therefore, small, narrow sized crystals were obtained, as shown in Figure 6-5 *c*. The final crystals were dried and characterized by Marven 2000 with a mean size 21.9 µm as is shown in Figure 6-6, which shows a narrowed CSD. The pulsed ultrasonic crystallization (30 s ultrasound irradiation with 30 s interval) produced almost the same sized crystals, while a peak appeared at 500 µm indicating slight agglomeration. For initial ultrasonic crystallization (30 s), significant agglomeration occurred as shown in 6-6 *b*. The comparison between the three methods of implementing ultrasound verified the effectiveness of ultrasonic irradiation to prevent agglomeration in the vanillin-water mixture. Stopping or pulsing the ultrasound would result in the agglomeration of crystals. During the crystallization process, ultrasonic irradiation could

effectively prevent fouling of surfaces and encrustation of crystals in the vanillin-water mixture, while it was a challenge in traditional mixing crystallization, especially for LLP separation systems. In addition, during the measurement of the phase diagram data, the ultrasonic crystallization processes showed a smaller standard deviation compared with the processes without ultrasound, indicating a more robust process using ultrasonic irradiation. The spontaneous nucleation and subsequent growth caused by process disturbances would generally produce a poor-quality product and challenge the scale-up of the process.
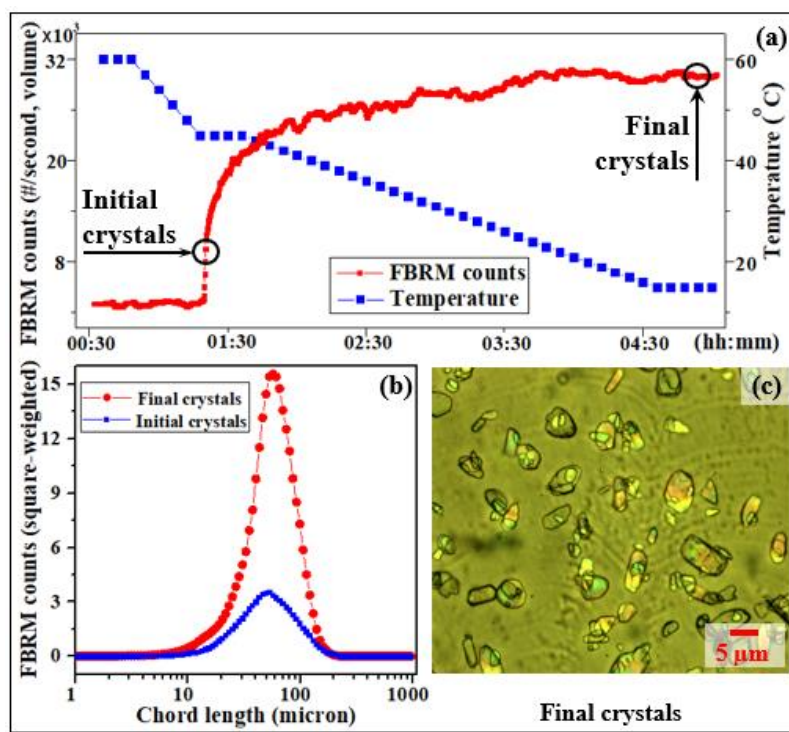
Figure 6-5: Ultrasonic crystallization process tracking Run 3. (a) *In-situ* FBRM counts tracking versus time, (b) *In-situ* FBRM chord length measurement of initial nucleation and final crystals, (c) Microphotographs of initial nucleation and final crystal formation
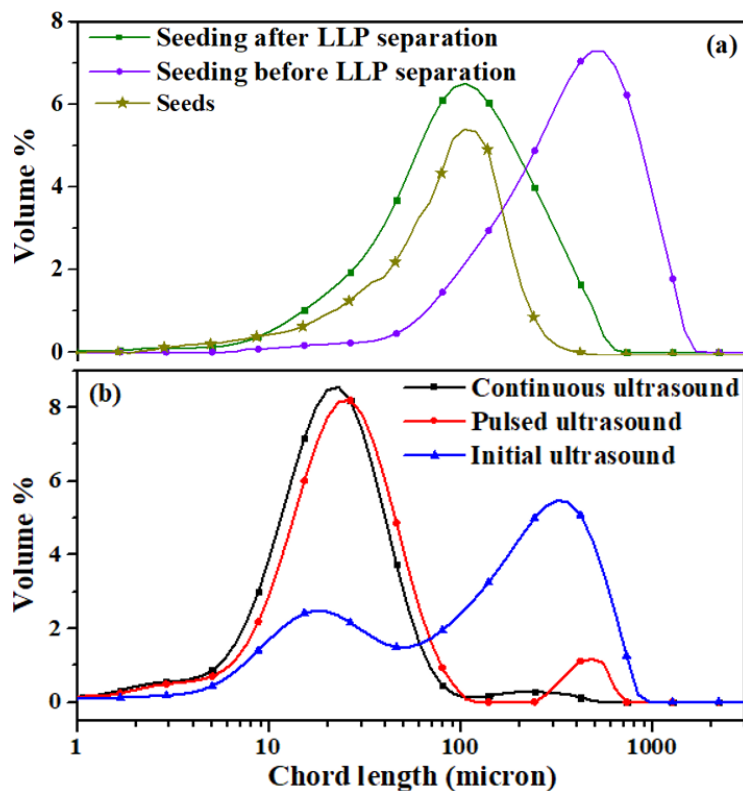
Figure 6-6: Crystal size distribution of crystal products using seeding crystallization and ultrasonic crystallization

6.3.3.2. Seeding Crystallization

It has been verified that seeding can prevent LLP separation and improve product quality as well as the performance of crystallization processes [14, 25, 38]. Two sets of experiments were conducted to study the performance of seeding in the LLP separation system. One involved seeding before LLP separation occurred and the other, for comparison, implemented seeding after LLP separation. The initial concentration, cooling rate as well as seeding amount were kept consistent as shown in Table 6-3. The CSD measured by Marven 2000 is shown in Figure 6-5 *a*.

Table 6-3: Seeding crystallization experiments

Run #	Seeding time*	Concentration	Cooling rate	Seeds amount
4	Before LLP separation, (45 °C)	4.2 g/100 g water	0.2 °C /min	1 wt%
5	After LLP separation, (30 °C)	4.2 g/100 g water	0.2 °C /min	1 wt%

*Note: the LLP separation temperature is 32 °C for the concentration 4.2 g/100 g water.

Figure 6-7 shows the crystallization process of seeding before LLP separation. There was a sharp increase of crystal counts (secondary nucleation) after the seeding as is shown in the inserted picture in Figure 6-7 *a*. Compared with the continuous ultrasonic crystallization process in Figure 6-5, the seeding process generated fewer crystals ($\times 10^3$) for further growth, which allowed the crystals to grow larger. The evolution of square-weighted chord distribution (Figure 6-7 *b*) from seeds to final crystals, indicated a full growth of crystals (to hundreds of microns) and the existence of some small crystals. As shown in Figure 6-7 *d*, slight agglomeration can be found because of the plate-like morphology and the crystals fragility, which induced secondary nucleation. There was a significant improvement compared with the LLP separation crystallization process, which showed significant agglomeration of crystals. The seeding after LLP separation also induced agglomeration of crystals and a broad peak was detected in the laser diffraction measurement (Figure 6-5 *a*). In the experiments of seeding after LLP separation, where the solution was at high supersaturation leading to a high local concentration in the oil droplets, excessive nuclei were generated (secondary nucleation) which resulted in agglomeration. In contrast, seeding before LLP separation could effectively control nucleation by preventing LLP separation to improve product the quality of crystals and enhance process performance. A comprehensive study of seeding recipes such as the loading amount, timing, properties of seeds and the cooling trajectory is needed to get the best performance of vanillin-water mixture crystallization.
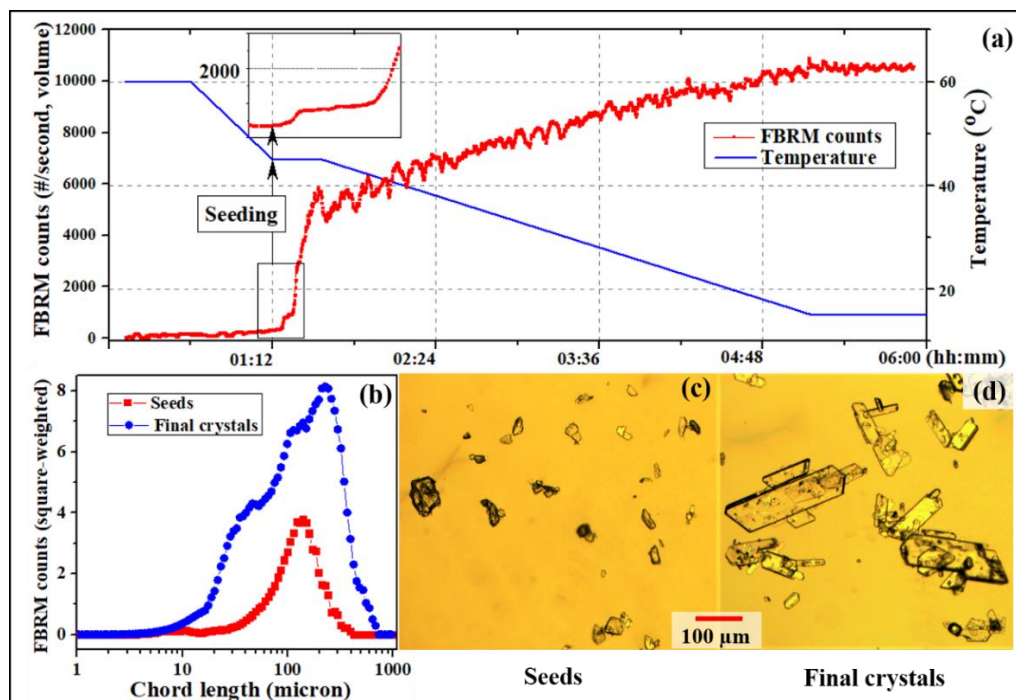
Figure 6-7: Tracking of seeding crystallization process, run 4 (a) *In-situ* FBRM counts tracking versus time, (b) *In-situ* FBRM chord length measurement of seeds and final crystals, (c, d) Microphotographs of seeds and crystal products

6.4. Conclusion

The LLP separation phenomenon of vanillin in aqueous solution was studied in a heating-cooling cycle using a microscope hot-stage. Results showed an oil phase both in the heating up and cooling down periods that corresponded to the stable and metastable LLP separation. It has been found that nucleation first occurs in the oil droplets during the cooling process, indicating that the oil droplet acted as a precursor to crystallization. In bulk cooling crystallization experiments, the crystallization phase diagrams and thermodynamic phase diagram were developed using in-situ FBRM which was also used to track and optimize the ultrasonic crystallization and seeding crystallization processes. The stable zone and metastable zone of LLP separation were determined with and without ultrasonic irradiation. Ultrasonic irradiation can narrow the MSZW of nucleation and LLP separation to one half compared with the process without ultrasound. Within the concentration of 3.8-4.8 g/100 g water, the LLP separation was completely inhibited by ultrasound, proceeding with direct nucleation. The intensification of agitation accelerated the process to reach steady state and made room for optimization of the crystallization

process. Using continuous ultrasonic irradiation, small, uniformly sized crystals were obtained, and crystals were found to be obviously agglomerated under initial and pulsed ultrasonic irradiation. In addition, the ultrasonic crystallization process showed the ability to prevent fouling of surfaces and encrustation of crystals. Seeding also proved its effectiveness to prevent LLP separation and grow large crystals. The agglomeration was also visibly reduced in the experiment of seeding before LLP separation. In the case of vanillin aqueous crystallization, conclusions can be drawn that both ultrasound and seeding can prevent LLP separation and improve the process robustness and product quality. Further screening of parameters of ultrasonic crystallization (i.e. ultrasound frequency, power, amplitude, pulse space) and seeding crystallization (time of addition, seed properties, loading amount, etc.) are required to achieve the best performance in LLP separation of a given system.

6.5. References

1. Aasland, S.; McMillan, P. F. Density-driven liquid-liquid phase separation in the system AI$_2$O$_3$–Y$_2$O$_3$ *Nature* 1994, *369 (6482)*, 633–636.

2. Vela, S. D.; Braun, M. K.; Dörr, A.; Greco, A.; Möller, J.; Fu, Z.; Zhang, F.; Schreiber, F. Kinetics of liquid-liquid phase separation in protein solutions exhibiting LCST phase behavior studied by time-resolved USAXS and VSANS *Soft Matter* 2016, *12*, 9334–9341.

3. Dumetz, A. C.; Chockla, A. M.; Kaler, E. W.; Lenhoff, A. M. Protein Phase Behavior in Aqueous Solutions: Crystallization, Liquid-Liquid Phase Separation, Gels, and Aggregates *Biophs. J.* 2008, *94*, 570–583.

4. Wang, Y.; Latypov, R. F.; Lomakin, A.; Meyer, J. A.; Kerwin, B. A.; Vunnum, S.; Benedek, G. B. Quantitative Evaluation of Colloidal Stability of Antibody Solutions using PEG-Induced Liquid-Liquid Phase Separation *Mol. Pharm.* 2014, *11*, 1391–1402.

5. Li, X.; Yin, Q.; Zhang, M.; Hou, B.; Bao, Y.; Gong, J.; Hao, H.; Wang, Y.; Wang, J.; Wang, Z. Antisolvent Crystallization of Erythromycin Ethylsuccinate in the Presence of Liquid-Liquid Phase Separation *Ind. Eng. Chem. Res.* 2016, *55*, 766–776.

6. Lafferrère, L.; Hoff, C.; Veesler, S. Study of liquid-liquid demixing from drug solution *J. Cryst. Growth* 2004, *269*, 550–557.

7. Lu, J.; Li, Y.; Wang, J.; Ren, G.; Rohani, S.; Ching, C. Crystallization of an active pharmaceutical ingredient that oils out *Sep. Purif. Technol.* 2012, *96*, 1–6.

8. Albuquerque, I. de; Mazzotti, M. Crystallization Process Design Using Thermodynamics To Avoid Oiling Out in a Mixture of Vanillin and Water *Cryst. Growth Des.* 2014, *14*, 5617–5625.

9. Sun, M.; Du, S.; Chen, M.; Rohani, S.; Zhang, H.; Liu, Y.; Sun, P.; Wang, Y.; Shi, P.; Xu, S.; Gong, J. Oiling-Out Investigation and Morphology Control of β-Alanine Based on Ternary Phase Diagrams *Cryst. Growth Des.* 2018,*18*, 818–826.

10. Codan, L.; Bäbler, M.; Mazzotti, M. Phase Diagram of a Chiral Substance Exhibiting Oiling Out in Cyclohexane *Cryst. Growth Des.* 2010, *10*, 4005–4013.

11. Veesler, S.; Lafferrère, L.; Garcia, E.; Hoff, C. Phase Transitions in Supersaturated Drug Solution *Org. Process Res. Dev.* 2003, *7*, 983–989.

12. Wolde, P.; Frenkel, D. Enhancement of Protein Crystal Nucleation by Critical Density Fluctuations *Science* 1997, *277*, 1975–1978.

13. Vekilov, P. Nucleation *Cryst. Growth Des.* 2010, *10*, 5007–5019.

14. Du, Y.; Wang, H.; Du, S.; Wang, Y.; Huang, C.; Qin, Y.; Gong, J. The liquid-liquid phase separation and crystallization of vanillin in 1-propanol/water solution *Fluid Phase Equilib.* 2016, *409*, 84–91.

15. Lu, J.; Li, Y.; Wang, J.; Li, Z.; Rohani, S.; Ching, C. Study on the Oiling-out and Crystallization for the Purification of Idebenone *Org. Process Res. Dev.* 2012, *16*, 442–446.

16. Takasuga, M.; Ooshima, H. Control of Crystal Size during Oiling Out Crystallization of an API *Cryst. Growth Des.* 2014, *14*, 6006–6011.

17. Takasuga, M.; Ooshima, H. Control of Crystal Aspect Ratio and Size by Changing Solvent Composition in Oiling Out Crystallization of an Active Pharmaceutical Ingredient *Cryst. Growth Des.* 2015, *15*, 5834–5838.

18. Bonnett, P.; Carpenter, K.; Dawson, S.; Davey, R. Solution crystallisation via a submerged liquid-liquid phase boundary: oiling out *Chem. Commun.* 2003, 6, 698–699.

19. Veesler, S.; Revalor, E.; Bottini, O; Hoff, C. Crystallization in the Presence of a Liquid-Liquid Phase Separation *Org. Process Res. Dev.* 2006, *10*, 841–845.

20. Ilevbare, G.; Taylor, L. Liquid-Liquid Phase Separation in Highly Supersaturated Aqueous Solutions of Poorly Water-Soluble Drugs: Implications for Solubility Enhancing Formulations *Cryst. Growth Des.* 2013, *13*, 1497–1509.

21. Gracin, S.; Uusi-Penttilä, M.; Rasmuson Å. Ultrasound on the Nucleation of Polymorphs of p-Aminobenzoic Acid *Cryst. Growth Des.* 2005, *5*, 1787-1794.

22. Bhangu, S.; Ashokkumar, M.; Lee, J. Ultrasound Assisted Crystallization of Paracetamol: Crystal Size Distribution and Polymorph Control *Cryst. Growth Des.* 2016, *16*, 1934–1941.

23. Gao, Z.; Zhu, D.; Wu, Y.; Rohani, S.; Gong, J.; Wang, J. Motion-Based Multiple Object Tracking of Ultrasonic-Induced Nucleation: A Case Study of l-Glutamic Acid *Cryst. Growth Des.* 2017, *17*, 5007-5011.

24. Daver, S.; Rodeville, N.; Pineau, F.; Arlabosse, J. M.; Moureou, C.; Muller, F.; Pierre, R.; Bouquet, K.; Dumais, L.; Boiteau, J. G.; Cardinaud, I. Process Development and Crystallization in Oiling-Out System of a Novel Topical Antiandrogen *Org. Process Res. Dev.* 2017, *21*, 231-240.

25. Deneau, E.; Steele, G. An In-Line Study of Oiling Out and Crystallization *Org. Process Res. Dev.* 2005, *9*, 943–950.

26. Lafferrère, L.; Hoff, C.; Veesler, S. Phase Transitions in Supersaturated Drug Solution *Cryst. Growth Des.* 2004, *4*, 1175–1180.

27. Barrett, P.; Glennon, B. Characterizing the Metastable Zone Width and Solubility Curve Using Lasentec FBRM and PVM *Chem. Eng. Res. Des.* 2002, *80*, 799–805.

28. Svärd, M.; Gracin, S.; Rasmuson, Å. Oiling out or molten hydrate-liquid-liquid phase separation in the system vanillin–water *J Pharm Sci* 2007, *96*, 2390–2398.

29. Derdour, L. A method to crystallize substances that oil out *Chem. Eng. Res. Des.* 2010, *88*, 1174–1181.

30. Parimaladevi, P.; Kavitha, C.; Srinivasan, K. Investigation of the effect of liquid-liquid phase separation (LLPS) on nucleation and different growth stages of vanillin and bulk growth of defect-free single crystals from aqueous solution – a new approach *CrystEngComm* 2014, *16*, 2565–2569.

31. Cartwright, L.C. Vanilla-like Synthetics, Solubility and Volatility of Propenyl Guaethyl, Bourbonal, Vanillin, and Coumarin *J. Agric. Food Chem.* 1953, *1*, 312-314.

32. Threlfall, T. Structural and Thermodynamic Explanations of Ostwald's Rule *Org. Process Res. Dev.* 2003, *7*, 1017–1027.

33. Ruecroft, G.; Hipkiss, D.; Ly, T.; Maxted, N.; Cains, P. Sonocrystallization: The Use of Ultrasound for Improved Industrial Crystallization *Org. Process Res. Dev.* 2005, *9*, 923–932.

34. Jiang, M.; Papageorgiou, C.; Waetzig, J.; Hardy, A.; Langston, M.; Braatz, R. Indirect Ultrasonication in Continuous Slug-Flow Crystallization *Cryst. Growth Des.* 2015, *15*, 2486–2492.

35. Junyaprasert, V.; Morakul, B. Nanocrystals for enhancement of oral bioavailability of poorly water-soluble drugs *Asian J. Pharm. Sci.* 2015, *10*, 13–23.

36. Bakar, M.; Nagy, Z.; Saleemi, A.; Rielly, C. The Impact of Direct Nucleation Control on Crystal Size Distribution in Pharmaceutical Crystallization Processes *Cryst. Growth Des.* 2009, *9*, 1378–1384.

37. Narducci, O.; Jones, A. G.; Kougoulos, E. Continuous crystallization of adipic acid with ultrasound *Chem. Eng. Sci.* 2011, *66*, 1069–1076.

38. Duffy, D.; Cremin, N.; Napier, M.; Robinson, S.; Barrett, M.; Hao, H.; Glennon, B. In-situ monitoring, control and optimization of a liquid-liquid phase separation crystallization *Chem. Eng. Sci.* 2012, *77*, 112–121.

Chapter 7

Continuous Crystallization of α-form L-Glutamic Acid in an MSMPR-Tubular Crystallizer System

7. Continuous Crystallization of α-form L-Glutamic Acid in an MSMPR-Tubular Crystallizer System

Abstract

Continuous crystallization of active pharmaceutical ingredients is of prime significance. A continuous mixed suspension mixed product removal (MSMPR)-tubular crystallizer geometry is designed and optimized to produce the metastable α-form crystals of L-glutamic acid with uniform mean size of 130 microns. The MSMPR is used to produce well-tuned seed crystals that undergo further growth in a series of tubular crystallizers. The effects of the initial supersaturation, stirring speed, and nucleation temperature and residence time were optimized in the MSMPR crystallizer to tune the supply of continuous seeds by using the principal component analysis and in-situ particle tracking measurement. The continuous seeds of the desired metastable polymorphic form with specific size ranging from 5.0 to 15.0 microns and number density ranging from 500 to 1500 counts, were transferred to a series of three coiled tubular crystallizers for further growth. In addition, the cooling strategy in the tubular crystallizers was utilized to further optimize the quality of the final crystal product. The crystal size distribution (CSD) in the MSMPR-tubular crystallizer system was compared with a single MSMPR with the same residence time and found to be superior. Finally, a potential scale-up strategy of the MSMPR-tubular crystallizer system was proposed for further study.

7.1.   Introduction

With the growing interest in the continuous manufacturing in the pharmaceutical industry, tubular crystallizers have recently attracted much attention because of their high efficiency, narrow residence time distribution, less crystal-crystal and crystal-crystallizer collision, and inhibiting unfavorable secondary nucleation [1-6]. The tubular crystallizer has promising ability to optimize crystal properties and facilitate transfer to continuous manufacturing [7,8]. Alvarez and Myerson employed a static mixer and multiple anti-solvent addition point strategies in a continuous tubular crystallizer and obtained small crystals with a narrow CSD [4]. Hohmann *et al*. reviewed various continuous crystallization processes and pointed out that a separate continuous seeds preparation device can be connected to a tubular crystallizer [9]. Ni et *al.* have successfully developed and commercialized a continuous

oscillatory baffled crystallizer (OBC) to enhance process efficiency and optimize CSD [10-13]. Challenges exist due to the blockage and encrustation occurring in the tubular crystallizer [14]. For better control and elimination of the potential risks, seeding has been employed as one of the effective strategies in the crystallization process to improve product quality and enhance the robustness of crystallization processes [15-17]. Seeding contributes to the crystallization process in catalyzing the nucleation at a lower supersaturation level than needed for primary nucleation [18, 19]. The characteristics of seeds include size, size distribution, polymorphism, specific surface area and number density that directly affect the final product quality [7, 8].

Tubular crystallizers are often seeded and merely used for the growth of the seed crystals. In a crystallization system, the nucleation plays a crucial role in controlling process robustness and product quality. The metastable zone width and the induction time should be studied for building a robust and efficient process [20, 21]. More significantly, failure to control the nucleation may lead to the burst of nuclei, oiling out and gelation phenomena [22, 23]. In the present practice, seeds are prepared offline through milling, sieving, etc. Few papers have reported online methods for continuous seeds preparation [16, 21, 24, 25]. Eder *et al*. successfully developed a continuously seeded tubular crystallizer to control the crystallization process of acetylsalicylic acid [26]. Woo *et al.* successfully optimized the jets velocities in a jet crystallizer to produce continuous seeds and further grow the seeds in a batch crystallizer to the desired crystal size [16]. Qamar *et al.* studied the effect of different seeding strategies that included continuous seeding and periodic seeding combined or not combined with continuous fines removal [17]. Continuous seeding strategy contributes to the optimization of crystals' quality and enhances the process efficiency in the development of advanced crystallization technology.

In this paper, an MSMPR crystallizer was used to generate a continuous supply of seeds that would further grow in a downward-flowing helically coiled tubular crystallizer assembly. Though it is not possible to clearly separate nucleation and growth processes, highly uniform fine crystals can be generated in the MSMPR crystallizer that act as seeds supplied to the tubular crystallizer for further growth. The continuous supply of seeds produced larger crystals with uniform size distribution and desirable polymorphic identity. L-glutamic acid was used as the model compound in this study. It has two polymorphic

forms with a possible transformation from the metastable form to the stable form as verified and shown in Figure 7-1 [27, 28]. The metastable α-form is preferred for downstream processing because of prismatic morphology [39, 30]. A continuous stream of fine-tuned seeds of α-form was prepared in an MSMPR crystallizer by optimizing the initial supersaturation S_0, nucleation temperature T_n, stirring speed N, feed flowrate f and residence time R_t. Operational parameters to modify seeds' properties were identified in this work. Seeds were continuously transferred to a series of tubular crystallizers to grow the product with a uniform mean crystal size of 130 μm and the desirable polymorphic identity.
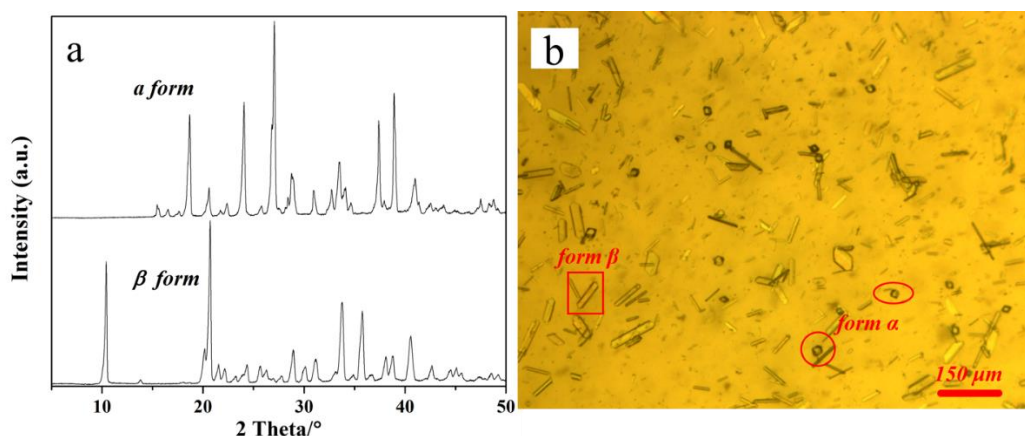
Figure 7-1: (a) XRPD patterns of α- and β-forms of L-glutamic acid standards; (b) Polymorphic transformation of form α (prismatic morphology) to form β (needlelike) after 8 hours at 45℃ with initial concentration 0.03 gmL^{-1}

7.2. Experimental Section

7.2.1. Experimental Procedure

7.2.1.1.Crystallization in the MSMPR-Tubular Crystallizer System

Continuous seeds preparation in the MSMPR crystallizer. The saturated solution with a solute concentration that ranged from 20.0 to 50.0 g/L was prepared at different temperatures in a double-jacketed feed tank as shown in Figure 7-2 (a). The saturated solution was pumped (Masterflex, L/S model, Cole-palmer Inc., Barrington, IL, USA) into the MSMPR crystallizer (total volume of 250 mL) which was equipped with a magnetic stirrer (Cimarec+, Thermo Fisher Scientific, USA) and a circulating constant temperature water bath (FT50, Julabo, Germany). A Focused Beam Reflectance Measurement (FBRM) probe (S400, Mettler Toledo, USA) was inserted into the MSMPR crystallizer to measure

the size/chord length and number density of the seeds. In the first step, 50, 100 or 150 mL of solution was pumped into the MSMPR crystallizer followed by vigorous stirring. Once the nucleation started, indicated with a sharp increase in the FBRM counts, the input and output pumps were simultaneously started. The timing of the start of continuous flow could affect the properties of seeds. Nucleation temperature T_n, stirring speed N, effective volume V_e, flowrate f and the mean residence time R_t in the MSMPR crystallizer were adjusted to generate a continuous supply of seeds with controlled size distribution and polymorphic identity. After arriving at the set-point temperature, at least three residence times were required to reach the steady-state operation in the MSMPR crystallizer.
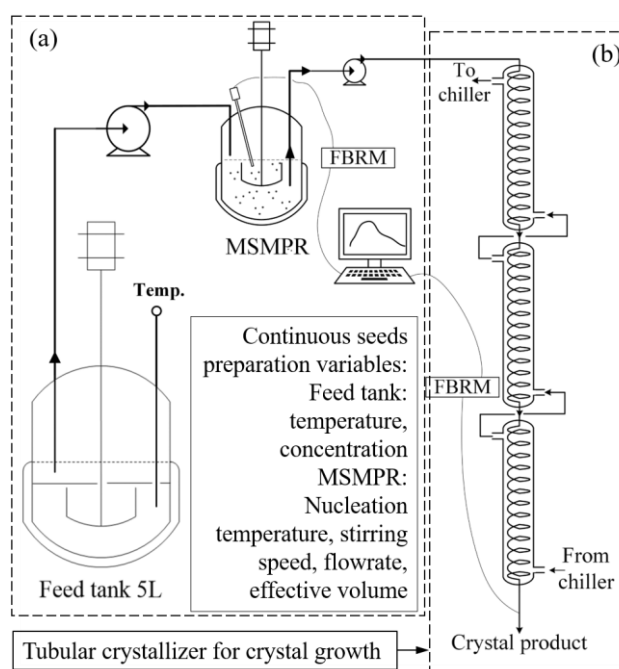
Figure 7-2: Schematic of (a) continuous seeds preparation setup and its operation parameters; (b) tubular crystallizer system

Crystal growth in the downstream tubular crystallizers. The continuous stream of finely-tuned seeds prepared in the upstream MSMPR crystallizer was transferred to a series of three double jacketed tubular crystallizers for further growth. The inlet temperature of cooling water was set to be 15 °C, and the cooling water was supplied to the jacket of the third tubular crystallizer and moving upward in a counter-current fashion. The cooling water was to cool down the crystal suspension within the tubular crystallizers from 35°C to 15°C. The flow rate of the suspension introduced to the tubular crystallizers was the same as the effluent flow rate of the MSMPR crystallizer. The size distribution of the crystalline

product at the outlet of the third tubular crystallizer was measured by *in-situ* FBRM. A 3D printed connector (Figure 0-5) was optimized to connect to the outlet of the tubular crystallizer. The angle between the probe and the slurry flow was optimized to be 45° to ensure impinge the flow onto the probe screen surface and avoid particle accumulation. The dried crystalline products were characterized by scanning electron microscopy (SEM, Hitachi S-2600) and particle size analyzer (Mastersizer 2000, Malvern Instruments Ltd. UK). The tubular crystallizers and all the pump tubing were washed with distilled water and preheated before the continuous operation.

7.2.1.2. Crystallization in a Single MSMPR Crystallizer

The performance of the MSMPR-tubular crystallizer system was compared with the performance of a single MSMPR crystallizer with a residence time equal to the combined residence times of the MSMPR-tubular crystallizer configuration. The experimental procedure in the single MSMPR was the same as described in the continuous seeds preparation section of the MSMPR-tubular crystallizer system. Instead of transferring the seeds to the tubular crystallizers, the finely-tuned seeds were further grown in the same MSMPR crystallizer. Once the steady-state was achieved in the MSMPR, the cooling water was switched to 15 °C using a second constant temperature water bath, through a three-way valve, for further growth. The solution volume was adjusted to 138 ± 2 mL along with an inlet saturated solution flow rate of 30 mL/min to keep the same residence time as in the MSMPR-tubular crystallizer system. Optical microscopy images of the real-time crystals were taken when the process reached the steady state. The CSD was characterized by an in-situ FBRM in the crystallizer and laser light scattering measurement of dried samples. All experiments were repeated at least three times to ensure reproducibility.

7.2.2. Materials

L-glutamic acid was purchased from Alfa Aesar (Ward Hill, MA) and used as received. Initial crystal form was β-form with purity 99+%. The solubility data from literature were verified and used [28]. Distilled water was used as the solvent in all experiments.

7.2.3.   Product Characterization

The polymorphism of the raw material and crystalline product was identified by powder X-ray diffraction (XRPD) using a Rigaku-MiniFlex powder diffractometer (Rigaku, Japan), and Cu$K\alpha$ (λ for $K\alpha$ = 1.54059 Å) over the range of $5° < 2\theta < 50°$ (with a step size of 0.02°). The MSMPR crystallizer was a double-jacketed glass vessel that had a total volume of 250 mL. It was equipped with a magnetic stirrer in the form of a rod-like stirring bar (10.0 × 38.0 mm). The tubular crystallizer consisted of three helically coiled double-jacketed glass tubes with an inner diameter of 0.5 cm and 7.0 m in total length. The total volume of the tubular crystallizer was about 137.4 mL, and the residence time was 4.6 min at a flow rate of 30 mL/min. The properties of the seeds in the MSMPR crystallizer and the crystal product at the outlet of the third tubular crystallizer were tracked using the in-situ FBRM. Optical microscopy images of the real-time crystals were taken by Zeiss Axioskop 40 microscope (Carl Zeiss, Germany). The crystalline product samples were dried at 60 °C overnight in an oven (Yamoto DKN 400, Scientific Co., Ltd, Yamato, Japan). Further characterization was conducted using scanning electron microscopy and laser light scattering particle size analysis.

7.3.   Results and Discussion

7.3.1.   Continuous Seeds Preparation and Characterization

The primary nucleation of L-glutamic acid takes more than 10 minutes in moderate conditions (supersaturation, mixing intensity etc.) [27, 31]. Therefore, the nucleation process of L-glutamic acid was performed in an MSMPR crystallizer with vigorous mixing to accelerate nucleation. Once the nucleation occurred in the MSMPR crystallizer, seeds were generated continuously for further growth in the downstream tubular crystallizers until the feed tank was almost depleted. Operational parameters of MSMPR crystallizer i.e. T_n, S_0, N, f and V_e were optimized within their operating range as listed in Table 1. Two objective functions were considered: i) maximizing the seeds size/chord length, and ii) controlling the seeds number density measured as FBRM counts. In the process of nucleation, uniform seeds size helps to generate uniform product crystals and a suitable number density of seeds could suppress secondary nucleation in the tubular crystallizer.

Table 7-1: Operational parameters of MSMPR crystallizer and operation limits during the continuous seeds preparation procedure

Control parameters	Operating range
Initial Supersaturation S_0	1.5-4.5
Nucleation Temperature T_n (°C)	25-45
Stirring Speed N (rpm)	300-900
Flow rate f (mL*min^{-1})	30-50
Effective Volume V_e (mL)	50-150
Residence Time $R_t = V_e/f$ (min)	1-5

Table 7-2: Typical experimental conditions and corresponding results in continuous seeds preparation processes

Run #	T_n (°C)	S_0	N (rpm)	f (mL /min)	V_e (mL)	R_t (min)	Mean size (µm)	FBRM counts #	Stdv (µm/#)	Crystal form
1	25.0	4.5	300	30	50	1.67	11.7	2864	1.6/378	α
2	25.0	4.0	300	30	100	3.33	23.4	3446	2.8/354	α
3	25.0	3.0	300	50	50	1	5.6	547	1.1/143	α
4	25.0	2.5	600	30	50	1.67	10.4	840	1.9/112	α
5	25.0	2.5	600	50	100	2	14.2	941	1.6/162	α
6	35.0	3.0	600	30	100	3.33	30.8	4560	2.5/224	α
7	35.0	2.5	600	30	50	1.67	9.2	545	1.8/92	α
8	35.0	2.0	600	50	150	3	15.6	620	1.6/78	α
9	35.0	1.6	600	30	50	1.67	8.7	422	1.0/51	α
10	35.0	1.6	900	30	50	1.67	6.8	522	1.2/150	α
11	35.0	1.6	900	50	100	2	10.1	640	1.4/149	α
12	35.0	1.6	900	50	150	3	13.2	965	1.5/178	α
13	45.0	2.5	600	30	50	1.67	13.4	829	1.3/146	α & β
14	45.0	2.0	900	30	100	3.33	19.6	903	2.1/194	α & β
15	45.0	1.5	900	30	150	5	23.4	1143	2.6/312	α & β

Notes: Supersaturation was calculated by $S_0 = \frac{C_0}{C^*}$, where C_0 is initial concentration and C^* is the saturated concentration at nucleation temperature; R_t was calculated by V_e/f; Stdv (µm/#) means stathe ndard deviation of mean size and FBRM counts. Each run was carried out at least three times and the reported mean size and FBRM counts represent the corresponding average values.

Typical experimental conditions and corresponding results are listed in Table 7-2. The mean size and number density of seeds were tracked by *in-situ* FBRM and the polymorphic form was confirmed by crystal morphology because of the clear difference in the habit of the two forms of L-glutamic acid, i.e. prismatic (α-form) and needle-like (β-form). This was confirmed by XRPD characterization. As shown in Table 7-2, the temperature played a key role in governing the polymorphism of seeds during the nucleation process. The results agree with a previous study that shows the nucleation rate of α-form decreases with the increase of temperature [32]. Further experiments were performed setting the nucleation temperature below 45 °C, and α-form seeds were generated without any polymorphic transformation during the experimental period. It was reported that high mixing intensity would help to drive the polymorphic transformation from the metastable α to the stable form β [10]. During the experiments with vigorous mixing, e.g. Runs 10-12, there was no transformation observed in the MSMPR crystallizer. This was due to a relatively short mean residence time (1-5 min) of seeds remaining in the MSMPR. Vigorous mixing enhanced the breakage of the seeds due to the collisions between the seed crystals, stirrer and vessel wall. The seeds became smaller in size with increased mixing intensity, e.g. in Runs 9 and 10. The mean residence time, by contrast, had a significant effect on the seeds size distribution. Figure 7-3 shows the seeds prepared under different operational parameters. There was a broad peak in the seeds size distribution in Figure 7-3 (a-1). This was because the mean residence time of Run 6 was longer than other runs. The mean residence time R_t was calculated as V_e/f, and V_e and f had a direct impact on the mean size and seeds number density. As shown in Runs 7, 8 and 10-12, there was an obvious increase in both the mean size and the number density of seeds with an increase in the effective crystallizer volume. Instead, an increase in the flow rate decreased the nucleation in the MSMPR and the crystal growth in the following tubular crystallizers. The secondary nucleation can be expressed in terms of a constant, K_N; N, the agitation rate; M, the suspension density; S, the supersaturation; and i, j, n, the exponents. V_e and f contribute to the suspension density of crystals that affects the nucleation kinetics. At higher supersaturations, a remarkable increase in the number density was noted compared to Runs 1, 4 and 6, 8.

$$B = K_N \cdot N^i \cdot M^j \cdot S^n \tag{7-1}$$
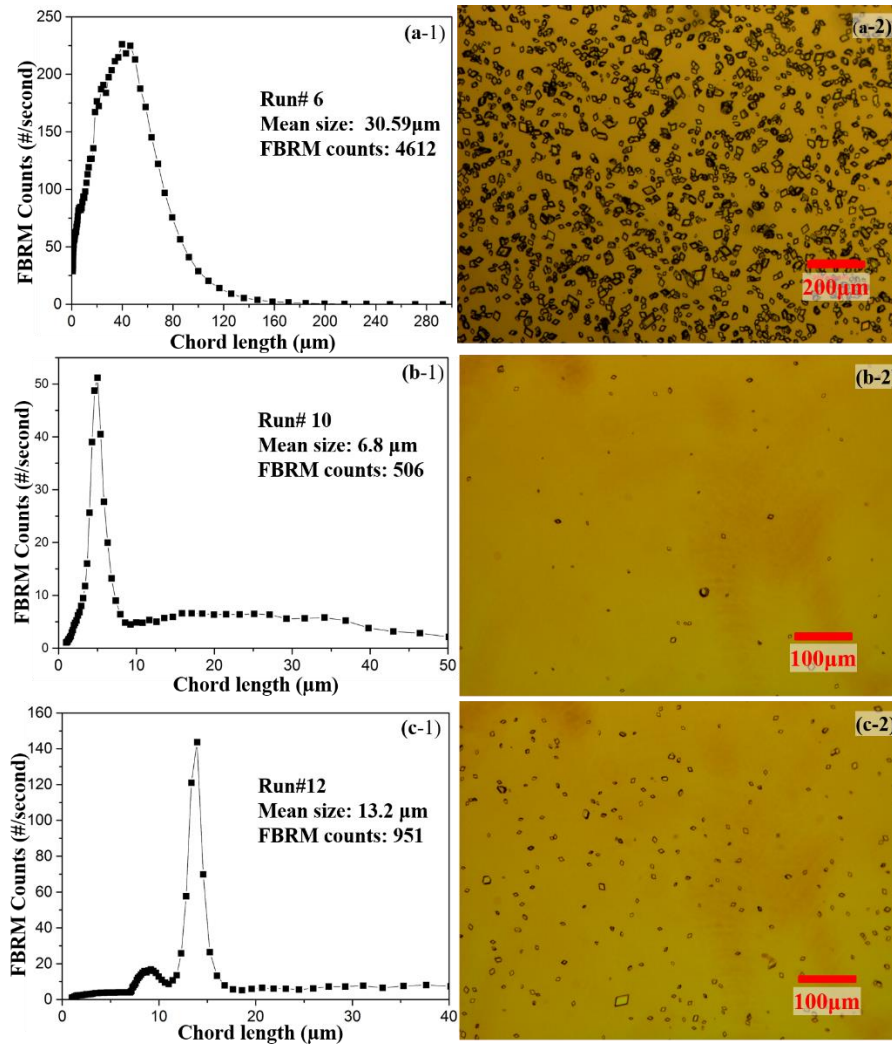
Figure 7-3: Microscopy images and FBRM tracking of continuously-prepared seeds in Run 6, 10, 12, respectively. (a-1), (b-1), (c-1) are seeds size distributions detected by *in-situ* FBRM at steady-state, (a-2), (b-2), (c-2) are the corresponding microscopy images

As shown in Figure 7-3, in-situ FBRM tracking indicated a narrow size distribution of seeds when parameters were optimized, e.g. see Figure 7-3 (b-1) and (c-1). The corresponding micrographs were taken as soon as the sample was taken out of the MSMPR crystallizer. As the number density in the MSMPR increased, agglomeration increased, e.g. Figure 7-3 (a-1), which resulted in the worst size distribution for the downstream tubular crystallizers. A moderate number density was crucial to control particle size distribution through suppressing the secondary nucleation and consuming supersaturation by crystal growth in the downstream tubular crystallizers.

7.3.2. Principal Component Analysis and Verification

It is hard to control all the six variables in the MSMPR system. In this study, the principal component analysis (PCA) was used to reduce the number of variables. The principal components are linear regression of original variables. The PCA was performed in Minitab 17.3 (Minitab Inc., State College PA, USA). The experiments were divided into two groups. One group of experiments was selected with a range of mean crystal size from 5.0 to 15.0 microns, and the other group of experiments was selected with a range of FBRM counts from 500 to 1000 counts. The details of the operational parameters and results are included in the appended Table 0-4 and Table 0-5. The regression coefficients are listed in support information (appended Table 0-6 and Table 0-7). The principal components were arranged in decreasing order of corresponding eigenvalues. The first principal component, which played the most important role in the nucleation process, was a linear combination of variables given by:

$$PC1 = 0.265T_n - 0.442S_0 + 0.461N + 0.239f + 0.494V_e + 0.470R_t \qquad (7\text{-}2)$$

The V_e accounted for the largest proportion in the first principal component, followed by N. S_0 became a negative coefficient which means an opposite effect on the mean size of seeds compared with V_e and N. The PCA analysis of twelve experiments on the score plot is shown in appended Figure 0-6. With the increase of effective volume, e.g. 100 mL, 150 mL, V_e became a larger score value and a more important factor that affected the mean size. Above all, V_e was the most effective factor to tune the mean size (ranging from 5.0 to 15.0 microns), followed by the second factor, N. The S_0 had the opposite effect compared with V_e and N. The score plots of N and S_0 versus the first two principal components are also presented in appended Figure 0-7.

Twelve experiments were grouped according to the FBRM counts that ranged from 500 to 1500 counts. PCA was performed to compress the variables to a smaller number of sensitive variables to control the number density of seeds. Unlike the analysis of seeds' size, both of the first two principal components accounted for large variability in number density. V_e (R_t) played an important role in the first principal component, and N was the most sensitive factor in the second principal component. A higher stirring speed contributed to a larger score value as analyzed in appended Figure 0-7. Compared with the analysis of

the mean size, N was the factor that showed more sensitivity to the number density and less sensitivity to the mean size.

As concluded above, V_e (R_t) was the most effective factor to tune the mean size and the number density of seeds and N was the factor to tune the number density and exerted less effect on the mean size. An operational scheme (which parameter affects which property and in which direction) for the continuous seeds preparation was summarized based on the principal components analysis in Table 7-3. An increase in V_e increased the mean size and the number density and was the most influential factor to tune seeds' properties. N was selected as the second factor to control the number density. For example, in the experiment of Size-/Counts+ (Table 7-3), V_e was decreased to reduce the mean size which was accompanied by a decrease in the number density. Increasing N was the second factor to regain the number density.

Table 7-3: Operational guidance for continuous seeds preparation

Output Variables	S_0	V_e (R_t)	T_n	N
Size-/Counts+	-	++	+	+
Size+/Counts-	-	++	+	--
Size-/Counts+	+	--	-	++
Size-/Counts-	+	--	-	+

Notes: +/- indicate the desired increase/decrease of mean size and FBRM counts or the increase/decrease of operation parameters. ++/-- indicate the most effective control factors.

7.3.3. Crystal Growth in Tubular Crystallizers

The finely-tuned seeds with the desired mean size, polymorphic form, and number density were continuously fed to the tubular crystallizers for further growth. The MSMPR-tubular crystallizer system is shown in

Table **7-2**. Every experiment was run at steady-state for about one hour until the feed tank was almost depleted.

In the MSMPR-tubular crystallizer system, the residence time distribution of crystals is narrower compared with a single MSMPR crystallizer with the same total mean residence time. As analyzed in Figure 7-4, peak 1 represents the CSD corresponding to the initial seeds that will be broadened over time in the following growth process in a single MSMPR as shown by peak 2. Instead, in the MSMPR-tubular crystallizer system, the residence time

of crystals is narrowed, peak 3, resulting in a more uniform CSD of the final crystal product.
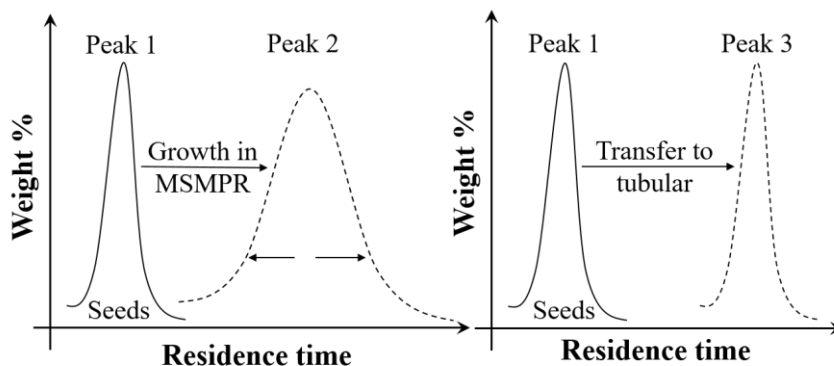
Figure 7-4: Qualitative schematic analysis of the effect of difference in the residence time in a single MSMPR and in the MSMPR-tubular crystallizer system on the crystal size distribution

In the direct nucleation control (DNC), the number density that significantly impacts the CSD must be controlled [33, 34]. There is a competition between the growth and secondary nucleation in a tubular crystallizer. A suitable number density of seeds that consume the supersaturation by crystal growth instead of generating overmuch nuclei by secondary nucleation is preferred to realize the optimization of CSD. A smaller or higher number density will result in an imbalance in crystal size and count. The seeds from Run 7 (9.2 ± 1.8 μm/545 ± 92) were selected as the optimum case and were transferred to the tubular crystallizers for further growth. The tubular crystallizer was placed vertically, as shown in Figure 7-2, to prevent the clogging issue. The cooling water entered at 15 °C and slowly flowed upward through the jackets of the three tubular crystallizers. Figure 7-5 shows the pictures and the size distribution of the final product of the single MSMPR and the MSMPR-tubular crystallizer system. The α-form crystals around 130 microns with uniform size were produced without polymorphic transformation during the process. However, there were some small crystals in the system, as indicated in Figure 7-5 a, which resulted in a peak around 25 microns in the FBRM tracking, Figure 7 5 (b). A slight breakage of crystal, marked by the contour in 7-5 (c), indicated a slight attrition due to crystal-crystal and crystal-crystallizer collision, which is expected in a plug flow tubular crystallizer. The final product from the MSMPR-tubular crystallizer system had a narrower

CSD with a mean crystal size of 130 microns compared to the single MSMPR crystallizer as is shown in Figure 7-5 (d).
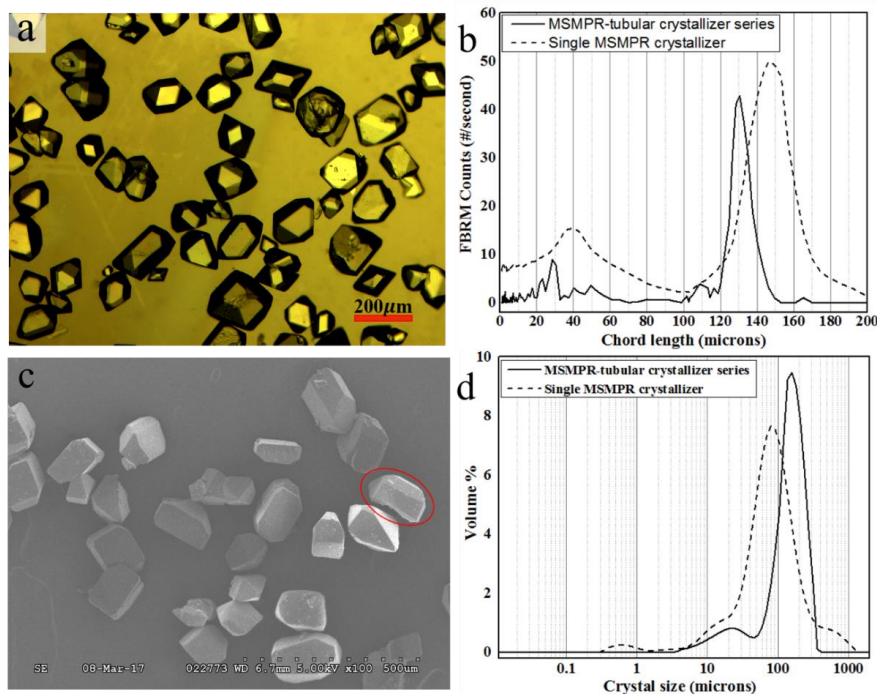
Figure 7-5: (a) Microscopy picture of crystals from MSMPR-Tubular system, (b) CSDs by in-situ FBRM monitoring in the MSMPR-tubular system and single MSMPR crystallizer, (c) SEM picture of the dried crystals from the MSMPR-Tubular system, and (d) CSDs of the dried crystals obtained in the MSMPR-tubular and the single MSMPR crystallizer

7.3.4. Crystallization in a Single Stage MSMPR Crystallizer

To compare the performance of the MSMPR-tubular crystallizer system with a conventional single stage MSMPR crystallizer, the experiments, with the same stirring speed in generating seeds and a similar cooling profile and residence time for crystal growth, were employed in a single MSMPR crystallizer. When the seeds (as in Run 7) were produced steadily in the MSMPR crystallizer, the temperature of the cooling water and the MSMPR working volume were adjusted to keep the same cooling profile and mean residence time similar to the MSMPR-tubular crystallizer system. Figure 7-6 (a) provides the schematic of the experimental setup of the single MSMPR crystallizer. When the process reached steady-state in the single MSMPR crystallizer, in-situ FBRM was used to measure the CSD in the suspension and Mastersizer 2000 was used to measure the size

distribution of the dried samples. Typical results were shown in Figure 7-5 (b, d). The CSD of the single MSMPR was much broader, monitored by both *in-situ* FBRM and light scattering measurement, and showed an obvious increase in the agglomeration and breakage of crystals, Figure 7-6 (b). The results show the advantage of the MSMPR-tubular system to produce uniform crystals with a unique polymorphic form. Further optimization of the cooling profile or using a longer tubular crystallizer produces a larger mean size with uniform size distribution.
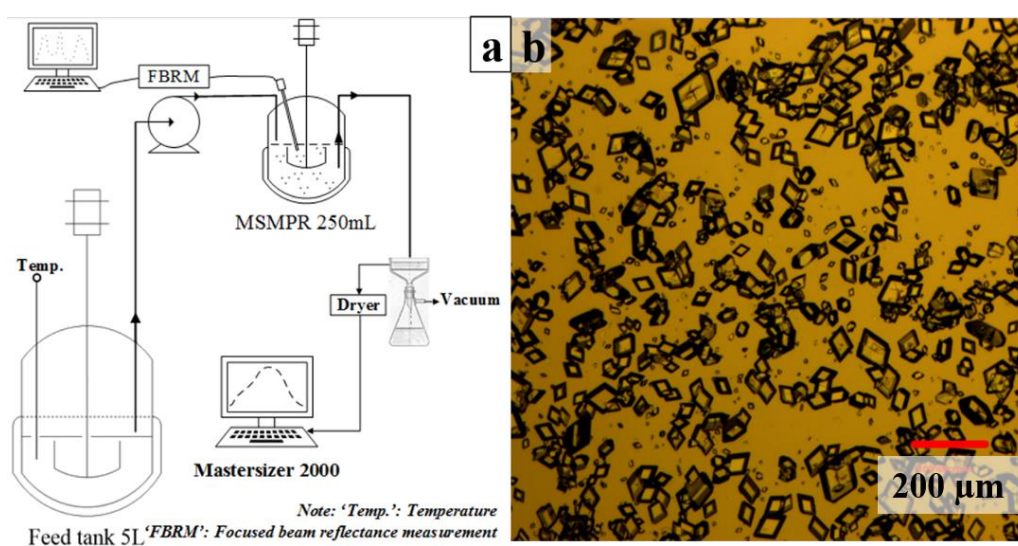
Figure 7-6: (a) Schematic setup of a single stage MSMPR crystallization process; (b) Microscopy image of the crystals produced in a single stage MSMPR crystallizer

7.4. Conclusions

The combination of an MSMPR and tubular crystallizers separated the nucleation and growth processes, and successfully produced the preferred α-form crystals of L-glutamic acid with a large mean size and a uniform size distribution. The MSMPR parameters were fine-tuned to produce a continuous supply of seeds with a desirable form, size and number density. With the help of the PCA analysis, the optimum MSMPR volume and stirring speed were identified as the most effective factors to tune the seeds' properties. The continuous stream of seeds was sent to the downstream tubular crystallizers for further growth, in which the number density would affect the competition between the growth and secondary nucleation processes. A moderate cooling profile along the tubular crystallizer

length suppressed the secondary nucleation and produced large crystals around 130 microns with uniform size.

Compared with a single MSMPR crystallizer, the proposed MSMPR-tubular crystallizer system has three advantages: 1) Finely-tuned supply of a continuous stream of seeds produced in the MSMPR with controllable form, size and number density improved the seeds' quality as well as process efficiency. 2) Moderate mixing in the tubular crystallizer reduced the breakage of crystals. 3) Narrow residence time distribution of the suspension in the entire process was ensured.

Although both the MSMPR and tubular crystallizer are conventional geometries in the crystallization literature, a combination of both to produce a uniform product CSD with the desired polymorphic form has not been reported, to the best of our knowledge. Finally, a potential scale-up strategy is shown in Figure 7-7. The process can be scaled up by using multiple tubular crystallizers in parallel, similar to a long shell-and-tube heat exchanger geometry. Segmental baffles can be installed on the shell side to optimize heat transfer and realize a uniform temperature profile for all tubular crystallizers. The filtrate at the end of the process can be used for recycling. Furthermore, an intermittent injection of an air stream into the coiled tube could be helpful in the scale-up of the proposed MSMPR-tubular crystallizer geometry to real application [35].
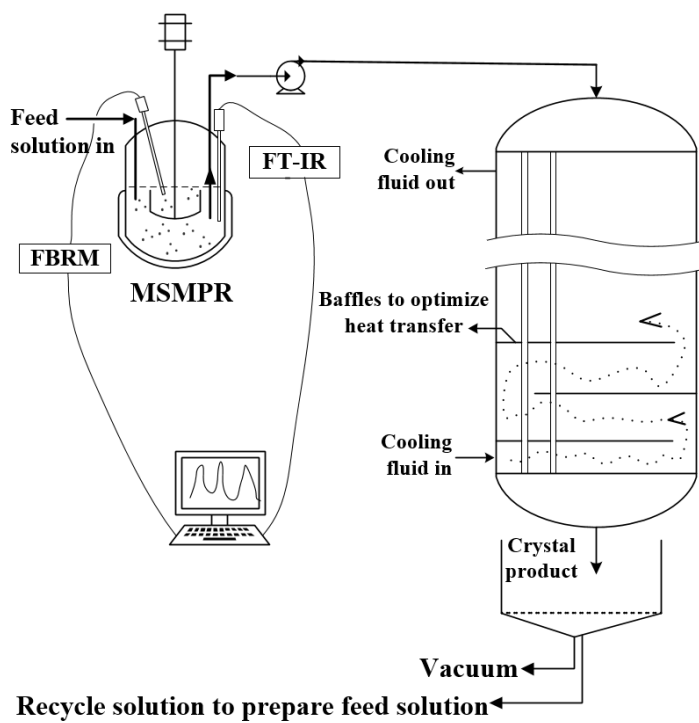
Figure 7-7: Schematic diagram of a potential scale-up strategy of the proposed MSMPR-Tubular crystallizer series

7.5. References

1. Raphael, M., Rohani, S., Sunflower protein precipitation in a tubular precipitator. *Can. J. Chem. Eng.* (1999), 77, 540–554.

2. Raphael, M., Rohani, S., Sosulski, F., Isoelectric precipitation of sunflower protein in a tubular precipitator. *Can. J. Chem. Eng.* (1995), 73, 470-483.

3. Raphael, M., Rohani, S., Sosulski, F. Recent Studies on Recovery of Oilseed Protein by Precipitation, Chapter 16, Separation and Purification by Crystallization, Ed. G. Botsaris and K. Toyokura, ACS Series, (1997) 188-209.

4. Alvarez, A.J., Myerson, A.S., Continuous Plug Flow Crystallization of Pharmaceutical Compounds. *Cryst. Growth Des.* (2010), 10, 2219–2228.

5. Majumder, A., Nagy, Z.K., Fines removal in a continuous plug flow crystallizer by optimal spatial temperature profiles with controlled dissolution. *AIChE J.* (2013), 59, 4582–4594.

6. Zhao, Y., Kamaraju, V., Hou, G., Power, G., Donnellan, P., Glennon, B., Kinetic identification and experimental validation of continuous plug flow crystallisation. *Chem. Eng. Sci.* (2015), 133, 106–115.

7. Aamir, E., Nagy, Z.K., Rielly, C.D., Evaluation of the Effect of Seed Preparation Method on the Product Crystal Size Distribution for Batch Cooling Crystallization Processes. *Cryst. Growth Des.* (2010), 10, 4728–4740.

8. Eder, R.J.P., Schmitt, E., Grill, J., Radl, S., Gruber-Woelfler, H., Khinast, J., Seed loading effects on the mean crystal size of acetylsalicylic acid in a continuous-flow crystallization device. *Cryst. Res. Technol.* (2011), 46, 227–237.

9. Hohmann, L., Gorny, R., Klaas, O., Ahlert, J., Wohlgemuth, K.; Kockmann, N. Design of a Continuous Tubular Cooling Crystallizer for Process Development on Lab-Scale. *Cryst. Res. Technol.* (2016), 39, 1268–1280.

10. Ni, X.W., Valentine, A., Liao, A., Sermage, S.B.C., Thomson, G.B., Roberts, K.J., On the Crystal Polymorphic Forms of l-Glutamic Acid Following Temperature Programmed Crystallization in a Batch Oscillatory Baffled Crystallizer. *Cryst. Growth Des.* (2004), 4, 1129–1135.

11. Lawton, S., Steele, G., Shering, P., Zhao, L., Laird, I., Ni, X.W., Continuous Crystallization of Pharmaceuticals Using a Continuous Oscillatory Baffled Crystallizer. *Org. Process Res. Dev.* (2009), 13, 1357–1363.

12. Ricardo, R., Ni, X.W., Evaluation and Establishment of a Cleaning Protocol for the Production of Vanisal Sodium and Aspirin Using a Continuous Oscillatory Baffled Reactor. *Org. Process Res. Dev.* (2009), 13, 1080–1087.

13. Ni, X.W., Callahan, C.J., Device for inducing nucleation. US Patent, (2012) US. 9,682,332 B2.

14. Wang, T., Lu, H., Wang, J., Xiao, Y., Zhou, Y., Bao, Y., Hao, H. Recent progress of continuous crystallization. *J. Ind. Eng. Chem.* (2017), 54, 14-29.

15. Aamir, E., Nagy, Z.K., Rielly, C.D., Optimal seed recipe design for crystal size distribution control for batch cooling crystallisation processes. *Chem. Eng. Sci.* (2010), 65, 3602–3614.

16. Woo, X.Y., Tan, R.B.H., Braatz, R.D., Precise tailoring of the crystal size distribution by controlled growth and continuous seeding from impinging jet crystallizers. *CrystEngComm.* (2011), 13, 2006–2014.

17. Qamar, S., Elsner, M.P., Hussain, I., Seidel-Morgenstern, A., Seeding strategies and residence time characteristics of continuous preferential crystallization. *Chem. Eng. Sci.* (2012), 71, 5–17.

18. Myerson, A.S., Handbook of Industry Crystallization, 2ed edition, Butterworth-Heinemann, 2002.

19. Agrawal, S.G., Paterson, A.H.J., Secondary Nucleation: Mechanisms and Models. *Chem. Eng. Commun.* (2015), 202, 698–706.

20. Zhang, G.P., Rohani, S., On-line optimal control of a seeded batch cooling crystallizer. *Chem. Eng. Sci.* (2003), 58, 1887–1896.

21. Jiang, M., Wong, M.H., Zhu, Z., Zhang, J., Zhou, L., Wang, K., Versypt, A.N.F., Si, T., Hasenberg, L.M., Li, Y.E., Braatz, R.D., Towards achieving a flattop crystal size distribution by continuous seeding and controlled growth. *Chem. Eng. Sci.* (2012), 77, 2–9.

22. Lu, J., Li, Y., Wang, J., Li, Z., Rohani, S., Ching, C., Study on the Oiling-out and Crystallization for the Purification of Idebenone. *Org. Process Res. Dev.* (2012), 16, 442-446.

23. Gao, Z., Li, L., Bao, Y., Wang, Z., Hao, H., Yin, Q., Wang, J., From Jellylike Phase to Crystal: Effect of Solvent on Self-Assembly of Cefotamixe Sodium. *Ind. Eng. Chem. Res.* (2016), 55, 3075-3083.

24. Wong, S.Y., Cui, Y., Myerson, A.S., Contact Secondary Nucleation as a Means of Creating Seeds for Continuous Tubular Crystallizers. *Cryst. Growth Des.* (2013), 13, 2514–2521.

25. Ferguson, S., Morris, G., Hao, H., Barrett, M., Glennon, B., Automated self-seeding of batch crystallizations via plug flow seed generation. *Chem. Eng. Res. Des.* (2014), 92, 2534–2541.

26. Eder, R.J.P., Radl, S., Schmitt, E., Innerhofer, S., Maier, M., Gruber-Woelfler, H., Khinast, J.G., Continuously Seeded, Continuously Operated Tubular Crystallizer for the Production of Active Pharmaceutical Ingredients. *Cryst. Growth Des.* (2010), 10, 2247–2257.

27. Lindenberg, C., Mazzotti, M., Effect of temperature on the nucleation kinetics of α L-glutamic acid. *J. Cryst. Growth.* (2009), 311, 1178–1184.

28. Sheikholeslamzadeh, E., Rohani, S., Modeling and Optimal Control of Solution Mediated Polymorphic Transformation of L-Glutamic Acid. *Ind. Eng. Chem. Res.* (2013), 52, 2633–2641.

29. Kee, N.C.S., Tan, R.B.H., Braatz, R.D., Selective Crystallization of the Metastable α-Form of l-Glutamic Acid using Concentration Feedback Control. *Cryst. Growth Des.* (2009), 9, 3044–3051.

30. Lai, T.C., Ferguson, S., Palmer, L., Trout, B.L., Myerson, A.S., Continuous Crystallization and Polymorph Dynamics in the L-Glutamic Acid System. *Org. Process Res. Dev.* (2014), 18, 1382–1390.

31. Schöll, J., Vicum, L., Müller, M., Mazzotti, M., Precipitation of L-Glutamic Acid: Determination of Nucleation Kinetics. *Cryst. Res. Technol.* (2006), 29, 257–264.

32. Kitamura, M., Polymorphism in the crystallization of L-glutamic acid. *J. Cryst. Growth.* (1989), 96, 541–546.

33. Bakar, M.R.A., Nagy, Z.K., Saleemi, A.N., Rielly, C.D., The Impact of Direct Nucleation Control on Crystal Size Distribution in Pharmaceutical Crystallization Processes. *Cryst. Growth Des.* (2009), 9, 1378–1384.

34. Yang, Y., Song, L., Nagy, Z., Automated Direct Nucleation Control in Continuous Mixed Suspension Mixed Product Removal Cooling Crystallization. *Cryst. Growth Des.* (2015), 15, 5839–5848.

35. Neugebauer, P., Khinast, J.G., Continuous Crystallization of Proteins in a Tubular Plug-Flow Crystallizer. *Cryst. Growth Des.* (2015), 15, 1089–1095.

Chapter 8

Conclusions and Future Work Recommendations

8. Conclusions and Future Work Recommendations

Abstract

The studies in this thesis demonstrated the feasibility of optimizing a crystallization process based on the fine-tuning of the nucleation step. Different pharmaceutical compounds with non-classical nucleation phenomena were investigated using well known in-line and off-line analysis techniques. The validated results of the nucleation mechanism, process monitoring methodologies, and optimization routes are specific for the chosen pharmaceutical compound systems. The conclusions and suggestions for the future study are given below.

8.1. Conclusions

In the section of non-classical nucleation mechanism study, a self-induced pre-nucleation clusters mechanism was proposed during anti-solvent crystallization process of Candesartan cilexetil (CC). According to the analysis of the in-situ process tracking as well as the solid-state characterization in different stages, the pre-nucleation clusters would act as a nucleation inducer in the bulk solution. At a high agitation level, the anti-solvent addition induced cloudy particles that dissolved before the occurrence of nucleation. Therefore, the solution eventually would go through homogeneous nucleation pathway. Inversely, at low levels of agitation, the cloudy particles would act as the nucleation inducer. In the study of cefotaxime sodium (CTX), 13 solvents were screened to investigate the interactions between CTX and solvent molecules. The H-bonding between the solvent and CTX molecule has been proved with the aid of FT-IR and in-situ Raman spectroscopy, which helped to explain the transformation from jellylike phase to crystals in molecular level. The results rendered a better understanding of JLP-to-crystal transition of active pharmaceutical ingredients and may have good application prospects in the pharmaceutical industry.

In order to help better understand the onset of nucleation, and the following crystallization process, two novel monitoring methods were developed. A motion-based multiple objects tracking (MMOT) technology was first introduced to crystallization to detect the onset of nucleation process. It was shown that the MMOT technology has same accuracy as the

FBRM in cooling crystallization and can track the nucleation process in the presence of ultrasonic irradiation. Under the latter circumstance, the FBRM failed to correctly detect the onset of nucleation. A better economic performance was demonstrated with the MMOT technology, and based on this detection method, potential applications can be extended to measure solubility, metastable zone width, particle size, and even solution-mediated polymorphic transformation. For in-line tracking of the entire crystallization process, a deep learning-based real-time image analysis technology was developed using the state-of-the-art neural network Mask R-CNN. Pixel-wise crystal segmentation was realized at a high image processing speed up to 10 frames per second. Crystal classification was first realized in the crystallization process of L-glutamic acid system, in which the segmented crystals were classified into two categories: α- (prismatic) and β-form (needlelike) crystals. Compared with the traditional measurement technology e.g. FBRM, the Mask R-CNN could provide much more process information such as crystal counts, surface area, crystal size, aspect ratio, etc.

Based on the study of non-classical nucleation phenomena and advanced process tracking technologies, the optimization of oiling out system was carried out to promote nucleation and narrow the metastable zone width. In the case of vanillin, the stable zone and metastable zone of liquid-liquid separation were determined with and without ultrasonic irradiation. Ultrasonic irradiation can narrow the metastable zone width of nucleation and prevent the LLP separation to one half compared with the process without ultrasound, and at a certain concentration, it can completely inhibit oiling out by leading to direct nucleation. In addition, the ultrasonic crystallization process showed the ability to prevent fouling of surfaces and encrustation of crystals. Seeding also proved its effectiveness to prevent oiling out resulting the growth of large crystals. In the oiling out system, conclusions can be drawn that both ultrasound and seeding can prevent liquid-liquid phase separation and improve the process robustness and product quality.

Future studies of the nucleation optimization and the entire crystallization process led to the development of an innovative combination of an MSMPR and tubular crystallizer which allowed separating the nucleation and growth processes and fine-tune the operational parameters during a crystallization process. In the MSMPR crystallizer stage,

the optimum MSMPR volume and stirring speed were identified as the most effective factors to tune the seeds' properties with the aid of principal component analysis. The continuous stream of seeds was sent to the downstream tubular crystallizers for further growth, in which the number density would affect the competition between the growth and secondary nucleation processes to determine the final crystal product. At last, the combined MSMPR-tubular system successfully produced the preferred α-form crystals of L-glutamic acid with a large mean size and a uniform size distribution. A moderate cooling profile along the tubular crystallizer length suppressed the secondary nucleation and produced large crystals around 130 microns with uniform size.

8.2. Future Work Recommendations

8.2.1. Visualize and experimentaly validate non-classical nucleation theory

There are great opportunities to further study the nucleation mechanism which is fundamental variable to control the properties of a new crystalline material and design high-efficiency crystallization process, especially for non-classical nucleation phenomena. In this thesis, we proposed the mechanisms of self-induced nucleation and jellylike phase mediated nucleation, in addition to the most popular non-classical nucleation mechanism of the two-step nucleation theory (TNT). The TNT helps to explain the origin of crystals and the difference between the experimental of nucleation kinetics and theoretical prediction using classical nucleation theory [1-4]. The intermediate phase or clusters are usually several hundred nanometers and to track by experimentally. Future research can be carried out to look for the experimental evidence of the two-step nucleation theory in small organic molecules and protein crystallization as depicted in Figure 8-1. The nanoscale dynamic tracking is facilitated by the dynamic lighting scattering and nanoparticle tracking analysis can be tracked by measuring the particle counts, size, and visualize the Brownian motion of nanoparticles in the solution crystallization process. In addition, the static advanced characterization facilities e.g. transmission electron microscopy (TEM), atomic force microscope (AFM), could assist to provide effective evidence of the mechanism of nucleation in future study. The experimental evidence for the two-step nucleation will

contribute to the development of the two-step nucleation theory as well as the understanding of solution crystallization process [5].
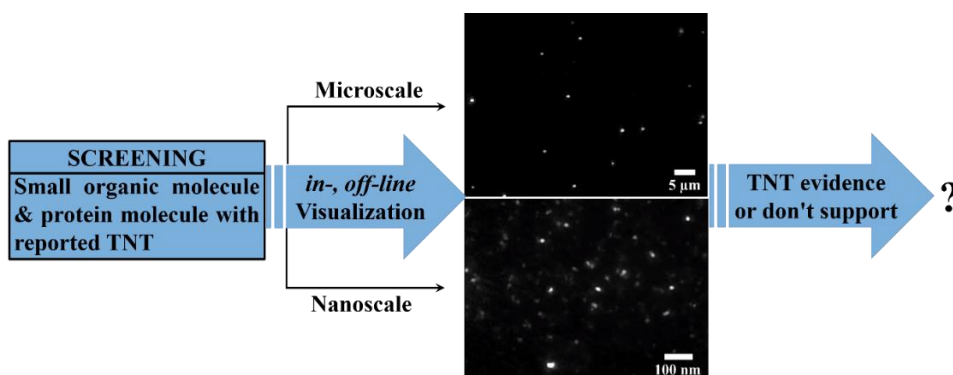
Figure 8-1: Schematic of two-step nucleation theory (TNT) experimental validation investigation using advanced visualization technologies

8.2.2. From virtual to reality, integrate imaging analysis to real application

As we reported in chapter 5 rapid development of artificial intelligence through object segmentation and classification is a big step forward in the real characterization of particulate process [6]. There are two challenges in imaging real-time process which are also the opportunities for deep learning-based imaging technology, accuracy and efficiency. Traditional mathematical algorithms require several seconds to process one image, which is impossible to implement in a time-based tracking system. What is worse, the mathematic models are hard to transfer to other systems with different field, brightness, contrast ratio between crystals and background. Beyond these two challenges (pixel-wise accuracy, less than 0.1 second per image), the deep learning-based imaging technology can be further enhanced by minimizing the time and effort for the training dataset. Proper training of the neural network to cover all aspects of crystal properties such as shape, visible size, number density, agglomeration, overlapping, breakage, etc. would facilitate monitoring and control of the solution crystallization processes.

To further promote the deep learning-based imaging crystallization, virtual reality (VR) and augmented reality (VR) technologies are suggested to build the training datasets that may contain millions of annotated crystals that cover all situations that may be encountered in a solution crystallization process [7-9]. As shown in Figure 8-2, the crystals in the left upper

image can be built in a virtual environment and used for data training. This idea is inspired by playing virtual games like DOTA in which all the virtual objects and actions can be built and rendered to mimic the real world. With known details of the rendered crystals in the images, the neural network can be trained by millions of virtual crystals and pictures, so that it can handle all the situations in a real solution crystallization process. Besides expanding the training dataset, as shown in Figure 8-2, high-quality real-time images can be acquired by a flexible in-line camera probe which is demonstrated with a back lighting module in the lower left image. Front lighting can also be considered for the camera probe in order to adapt it to different situations. Beside the training dataset and the real-time images, the most advanced artificial neural network should be used for the rapid development of artificial intelligence. At last, the crystals in various crystallization processes can be segmented and classified and then followed by data mining and process analysis. This proposal will empower the deep learning-based method to revolutionize the current status of real-time imaging technology and in the solution crystallization process.
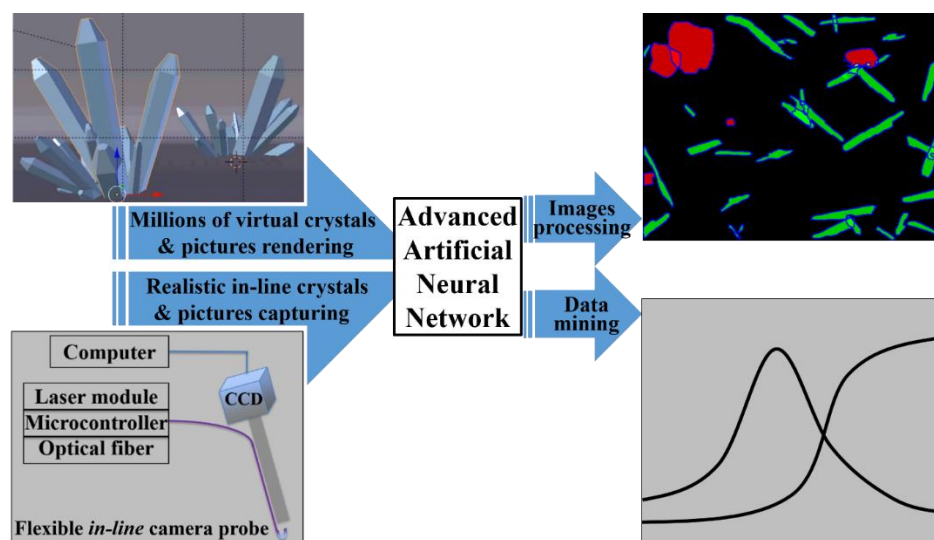
Figure 8-2: Schematic of integrating virtual crystal rending, high-quality in-line images capturing, and advanced artificial neural network into practicing deep learning-based imaging crystallization

8.2.3. Fine-tune continuous slurry in nucleation, dissolution, and growth (NDG) process configuration

The nucleation-based optimization methodology has proved to be an effective method to optimize the whole crystallization process [10, 11]. The robustness of an optimized nucleation process can be challenged by the sensitive operational parameters like the stirring speed, residence time as mentioned in chapter 7. To improve the process robustness and applicability to various chemical systems, a crystal nucleation, dissolution, and growth (NDG) model is proposed in an integrated two-stage MSMPR and tubular crystallizer series, as shown in Figure 8-3. In the two-stage MSMPR crystallizer, nucleation is supposed to take place in the first stage crystallizer and excess crystals will be dissolved in the second stage MSMPR crystallizer, which will provide a simple and effective control of the nucleation process. The continuous nuclei-containing slurry will be sent to the following tubular crystallizer for further growth. An air and liquid slug flow is suggested to avoid clogging and encrustation in the tubular crystallizer. Two cameras are proposed to be implement in this system, camera 1 can be used to monitor the slug flow, interface of air and liquid, and camera 2 can be used to monitor the crystal shape, size, etc. To avoid the possibility of clogging between the integrated stages, two transfer modules are proposed, as shown in Figure 8-4 using a peristaltic pump, a pinch valve and a 3-way valve in different configurations. With the help of a microcontroller, a tight control of air and slurry segmented flow can be realized to help to transfer the slurry smoothly and make room for following process optimization in tubular crystallizer stage. A simulation model should be developed to study the steady state condition in every stage crystallizer and optimize the operational parameters to achieve the best of this system [12].
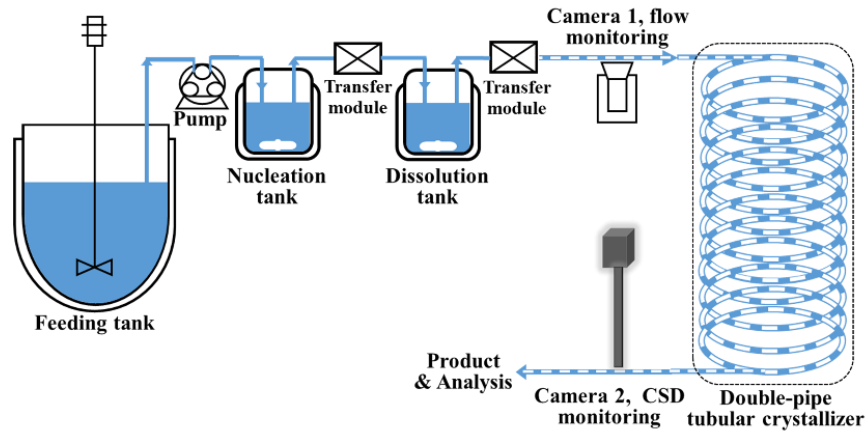
Figure 8-3: Schematic of crystal nucleation, dissolution, and growth (NDG) continuous crystallization equipment series
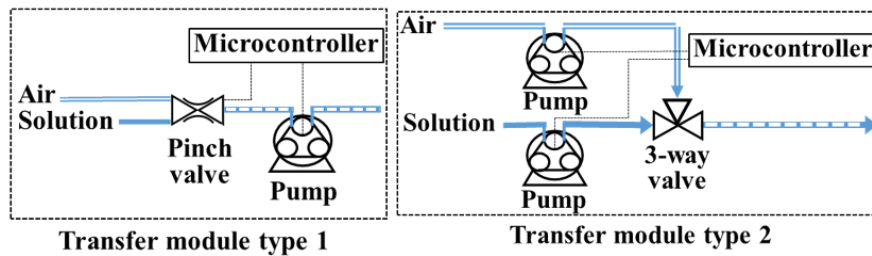
Figure 8-4: Schematic of the design of transfer modules in the continuous crystallization process

8.3.   References

1. Erdemir, D.; Lee, A. Y.; Myerson, A. S. Nucleation of crystals from solution: classical and two-step models. *Acc. Chem. Res.* 2009, 42(5), 621-629.

2. Myerson, A. S.; Bernhardt, L. T. Nucleation from solution. *Science* 2013, 341, 855-856.

3. Smeets, P. J.; Finney, A.R.; Habraken, W. J.; Nudelman, F.; Friedrich, H.; Laven, J.; De Yoreo, J. J.; Rodger, P. M.; Sommerdijk, N. A. A classical view on nonclassical nucleation. *Proc. Natl. Acad. Sci. U.S.A.* 2017, 114(38) 7882-7890.

4. Vekilov, P. G. The two-step mechanism of nucleation of crystals in solution. *Nanoscale* 2010, 2(11), 2346-2357.

5. Schubert, R.; Meyer, A.; Baitan, D.; Dierks, K.; Perbandt, M.; Betzel, C. Real-time observation of protein dense liquid cluster evolution during nucleation in protein crystallization. *Cryst. Growth Des.* 2017, 17(3), 954-958.

6. Christiansen, E. M.; Yang, S. J.; Ando, D. M.; Javaherian, A.; Skibinski, G.; Lipnick, S.; Mount, E.; O'Neil, A.; Shah, K.; Lee, A. K.; Goyal, P. In silico labeling: Predicting fluorescent labels in unlabeled images. *Cell* 2018, 173(3), 792-803.

7. Alhaija, H. A.; Mustikovela, S. K.; Mescheder, L.; Geiger, A.; Rother, C. Augmented reality meets computer vision: Efficient data generation for urban driving scenes. *Int. J Comput. Vis.* 2018, 126(9), 961-972.

8. Tian, Y.; Li, X.; Wang, K.; Wang, F. Y. Training and testing object detectors with virtual images. *IEEE/CAA Journal of Automatica Sinica.* 2018, 5(2), 539-546.

9. Agarwal, S.; Terrail, J. O.; Jurie, F. Recent Advances in Object Detection in the Age of Deep Convolutional Neural Networks. *arXiv preprint* 2018, arXiv:1809.03193.

10. Acevedo, D.; Jarmer, D. J.; Burcham, C. L.; Polster, C. S.; Nagy, Z. K. A continuous multi-stage mixed-suspension mixed-product-removal crystallization system with fines dissolution. *Chem. Eng. Res. Des.* 2018, 135, 112-120.

11. Han, B.; Ezeanowi, N. C.; Koiranen, T. O.; Hakkinen, A. T.; Louhi-Kultanen, M. Insights into Design Criteria for a Continuous Sonicated Modular Tubular Cooling Crystallizer. *Cryst. Growth Des.* 2018, 18(12), 7286-7295.

12. Sulttan, S.; Rohani, S.; Coupling of CFD and population balance modeling for a continuously seeded helical tubular crystallizer. *J. Cryst. Growth.* 2019, 505, 19-25.

Appendices

Chapter 3 appendix

Chapter 3: From Jellylike Phase to Crystal: Effects of Solvent on Nucleation of Cefotaxime Sodium
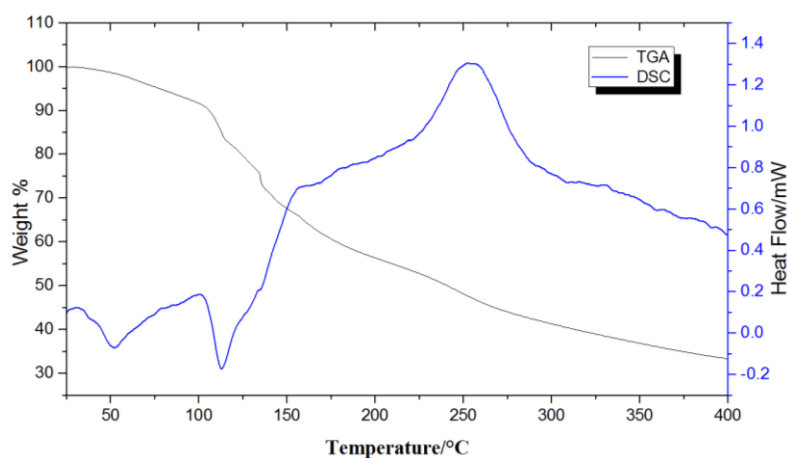
Figure 0-1: TGA and DSC curves of C2
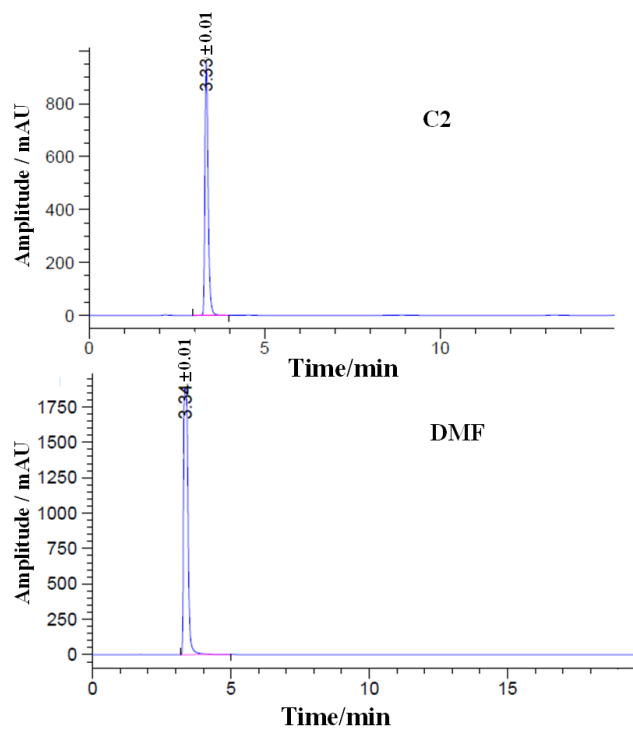
Figure 0-2: HPLC chromatograms of DMF and C2. (The uncertainty of the time is 0.01 min)
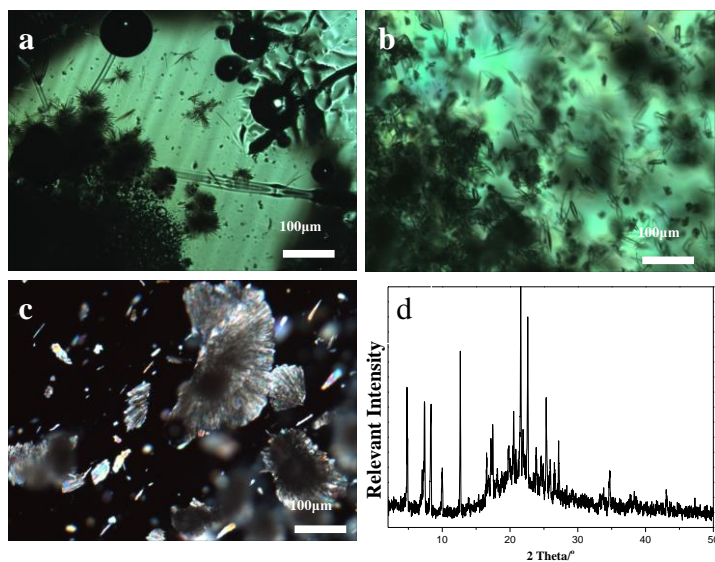
Figure 0-3: Microscopic images of crystals obtained from JLP crystallization under the atmosphere of (a) formamide, (b) methanol, (c) pyridine. (d) is XRPD of the crystal crystallized under pyridine atmosphere

Chapter 4 appendix

Chapter 4: Motion-Based Multiple Object Tracking of Ultrasonic-Induced Nucleation: A Case Study of L-Glutamic Acid
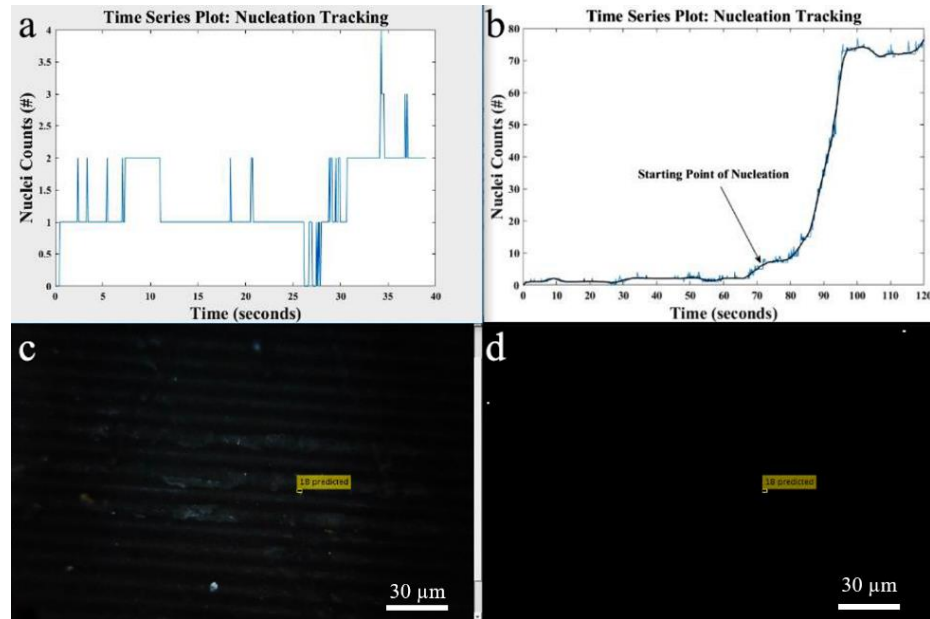
Figure 0-4: In-situ detection results under the conditions of 40 g/L and 35°C. (a) Plot at 38th second of crystals counts against time series using the MMOT model; (b) Plot of crystals counts against time based on nucleation tracking of the whole process. (c) Detected objects at 38th second. (d) Detected objects at 38th second after background was subtraction

Table 0-1: MATLAB Code for motion-based multiple object tracking (MMOT)

```
function multiObjectTracking()

obj = setupSystemObjects();
ts = timeseries();
start = 0;
resultFigHanlder = figure;
tracks = initializeTracks();
frameNo = 0;
nextId = 1;
while ~isDone(obj.reader)
    frame = readFrame();
    [centroids, bboxes, mask] = detectObjects(frame);
    predictNewLocationsOfTracks();
    [assignments, unassignedTracks, unassignedDetections] = ...
        detectionToTrackAssignment();
    updateAssignedTracks();
```

```matlab
      updateUnassignedTracks();
      deleteLostTracks();
      createNewTracks();
      updateNumberOfParticles();
      displayTrackingResults();
      frameNo = frameNo + 1;
  end
     function updateNumberOfParticles()
        ts=ts.addsample('Data',length(tracks),'Time',(frameNo-start)/obj.frameRate);
     end
     function obj = setupSystemObjects()
        inputFileName = 'nuc4.mp4';
        outputFileName = 'nuc4_out.mp4';
        maskFilename = 'nuc4_mask.mp4';
        obj.reader = vision.VideoFileReader(inputFileName);
        obj.frameRate = obj.reader.info.VideoFrameRate;
       obj.writer = vision.VideoFileWriter(outputFileName, 'FrameRate', obj.frameRate,
'FileFormat', 'MPEG4');
        obj.maskWriter = vision.VideoFileWriter(maskFilename, 'FrameRate',
obj.frameRate, 'FileFormat', 'MPEG4');
        obj.videoPlayer = vision.VideoPlayer('Position', [20, 400, 700, 400]);
        obj.maskPlayer = vision.VideoPlayer('Position', [740, 400, 700, 400]);
        obj.detector = vision.ForegroundDetector('NumGaussians', 5, ...
           'NumTrainingFrames', 10, 'MinimumBackgroundRatio', 0.8);
        obj.blobAnalyser = vision.BlobAnalysis('BoundingBoxOutputPort', true, ...
           'AreaOutputPort', true, 'CentroidOutputPort', true, ...
           'MinimumBlobArea', 30);
     end
    function tracks = initializeTracks()
        tracks = struct('id', {}, 'bbox', {}, 'kalmanFilter', {},  'age', {}, ...
           'totalVisibleCount', {}, ...
           'consecutiveInvisibleCount', {});
     end
     function frame = readFrame()
        frame = obj.reader.step();
     end
     function [centroids, bboxes, mask] = detectObjects(frame)
        mask = obj.detector.step(frame);
        mask = imopen(mask, strel('rectangle', [3,3]));
        mask = imclose(mask, strel('rectangle', [15, 15]));
        mask = imfill(mask, 'holes');
        [~, centroids, bboxes] = obj.blobAnalyser.step(mask);
     end
     function predictNewLocationsOfTracks()
        for i = 1:length(tracks)
           bbox = tracks(i).bbox;
```

```matlab
            predictedCentroid = predict(tracks(i).kalmanFilter);
            predictedCentroid = int32(predictedCentroid) - bbox(3:4) / 2;
            tracks(i).bbox = [predictedCentroid, bbox(3:4)];
        end
    end
    function [assignments, unassignedTracks, unassignedDetections] = ...
            detectionToTrackAssignment()
        nTracks = length(tracks);
        nDetections = size(centroids, 1);
        cost = zeros(nTracks, nDetections);
        for i = 1:nTracks
            cost(i, :) = distance(tracks(i).kalmanFilter, centroids);
        end
        costOfNonAssignment = 20;
        [assignments, unassignedTracks, unassignedDetections] = ...
            assignDetectionsToTracks(cost, costOfNonAssignment);
    end
    function updateAssignedTracks()
        numAssignedTracks = size(assignments, 1);
        for i = 1:numAssignedTracks
            trackIdx = assignments(i, 1);
            detectionIdx = assignments(i, 2);
            centroid = centroids(detectionIdx, :);
            bbox = bboxes(detectionIdx, :);
            correct(tracks(trackIdx).kalmanFilter, centroid);
            tracks(trackIdx).bbox = bbox;
            tracks(trackIdx).age = tracks(trackIdx).age + 1;
            tracks(trackIdx).totalVisibleCount = ...
                tracks(trackIdx).totalVisibleCount + 1;
            tracks(trackIdx).consecutiveInvisibleCount = 0;
        end
    end
    function updateUnassignedTracks()
        for i = 1:length(unassignedTracks)
            ind = unassignedTracks(i);
            tracks(ind).age = tracks(ind).age + 1;
            tracks(ind).consecutiveInvisibleCount = ...
                tracks(ind).consecutiveInvisibleCount + 1;
        end
    end
    function deleteLostTracks()
        if isempty(tracks)
            return;
        end
        invisibleForTooLong = 30;
        ageThreshold = 8;
```

```
      ages = [tracks(:).age];
      totalVisibleCounts = [tracks(:).totalVisibleCount];
      visibility = totalVisibleCounts ./ ages;
      lostInds = (ages < ageThreshold & visibility < 0.6) | ...
         [tracks(:).consecutiveInvisibleCount] >= invisibleForTooLong;
      tracks = tracks(~lostInds);
   end
   function createNewTracks()
      centroids = centroids(unassignedDetections, :);
      bboxes = bboxes(unassignedDetections, :);
      for i = 1:size(centroids, 1)
      centroid = centroids(i,:);
         bbox = bboxes(i, :);
         kalmanFilter = configureKalmanFilter('ConstantVelocity', ...
            centroid, [200, 50], [100, 25], 100);
         newTrack = struct(...
            'id', nextId, ...
            'bbox', bbox, ...
            'kalmanFilter', kalmanFilter, ...
            'age', 1, ...
            'totalVisibleCount', 1, ...
            'consecutiveInvisibleCount', 0);
          tracks(end + 1) = newTrack;
          nextId = nextId + 1;
      end
   end
   function displayTrackingResults()
      mask = uint8(repmat(mask, [1, 1, 3])) .* 255;
      minVisibleCount = 2; % 8
      if ~isempty(tracks)
         reliableTrackInds = ...
            [tracks(:).totalVisibleCount] > minVisibleCount;
         reliableTracks = tracks(reliableTrackInds);
         if ~isempty(reliableTracks)
            bboxes = cat(1, reliableTracks.bbox);
            ids = int32([reliableTracks(:).id]);
            labels = cellstr(int2str(ids'));
            predictedTrackInds = ...
               [reliableTracks(:).consecutiveInvisibleCount] > 0;
            isPredicted = cell(size(labels));
            isPredicted(predictedTrackInds) = {' predicted'};
            labels = strcat(labels, isPredicted);
            frame = insertObjectAnnotation(frame, 'rectangle', ...
               bboxes, labels);
            mask = insertObjectAnnotation(mask, 'rectangle', ...
               bboxes, labels);
```

```
            end
        end
        obj.maskPlayer.step(mask);
        obj.videoPlayer.step(frame);
        obj.writer.step(frame);
        obj.maskWriter.step(mask);
        figure(resultFigHanlder);
        plot(ts);
    end
displayEndOfDemoMessage(mfilename)
end
```

Chapter 6 appendix

Chapter 6: Ultrasonic Irradiation and Seeding To Prevent Metastable Liquid–Liquid Phase Separation and Intensify Crystallization

Table 0-2: The measured data points in phase diagram Figure 6-3 and corresponding standard deviation

Weight (g), per 100g water, (±0.001g)	Solubility, (°C)	Without ultrasound		Using ultrasound	
		LLP separation, (°C)	Nucleation, (°C)	LLP separation, (°C)	Nucleation, (°C)
0.8	24.2 (0.03)	No	11.8 (0.05)	No	13.3 (0.11)
1.3	31.0 (0.02)	No	22.5 (0.06)	No	24.2 (0.08)
1.8	34.9 (0.03)	No	28.2 (0.06)	No	32.2 (0.05)
2.3	40.5 (0.03)	No	32.0 (0.11)	No	35.1 (0.08)
2.8	44.4 (0.03)	No	38.0 (0.08)	No	39.2 (0.05)
3.3	48.2 (0.03)	No	16.5 (0.18)	No	41.0 (0.05)
3.8	51.5 (0.05)	23.0 (0.08)	16.9 (0.13)	No	42.1 (0.06)
4.2	53.0 (0.05)	32.0 (0.08)	17.3 (0.08)	No	43.5 (0.03)
4.5	53.8 (0.06)	38.0 (0.06)	17.4 (0.11)	No	43.6 (0.11)
4.8	54.2 (0.05)	41.5 (0.05)	17.5 (0.08)	48.5 (0.01)	43.8 (0.08)
5.3	59.1 (0.11)	53.5 (0.06)	18.0 (0.13)	54.5 (0.03)	44.5 (0.06)
5.8	65.8 (0.08)	64.5 (0.08)	18.4 (0.11)	65.1 (0.01)	46.0 (0.06)
6.3	68.7 (0.13)	66.2 (0.11)	19.3 (0.11)	68.3 (0.06)	46.1 (0.08)
6.8	74.0 (0.13)	69.5 (0.08)	20.0 (0.08)	73.6 (0.05)	46.5 (0.11)
7.3	81.0 (0.13)	72.1 (0.08)	21.3 (0.11)	79.0 (0.08)	47.5 (0.08)

Note: The value in the bracket are standard deviation of the averaged data.

Table 0-3: The fitted equations of metastable curves in Figure 6-4 and corresponding R-squared

Curves	Fitted equations	R-square
LLP separation	$y_1 = 5373.8x - 36023x^2 - 126.3$	0.9939
Nucleation with LLP separation	$y_2 = 18.5 - 141.1 + 2596.2x^2$	0.9895
Nucleation without LLP separation	$y_3 = 2856.1x - 46458x^2 - 7.5$	0.9901
LLP separation with ultrasound	$y_4 = 2356.5x - 8273x^2 - 42.3$	0.9948
Nucleation with ultrasound	$y_5 = 46.6 - 59.5\exp(-75x)$	0.9938

Chapter 7 appendix

Chapter 7: Continuous Crystallization of α-form L-Glutamic Acid in an MSMPR-Tubular Crystallizer System
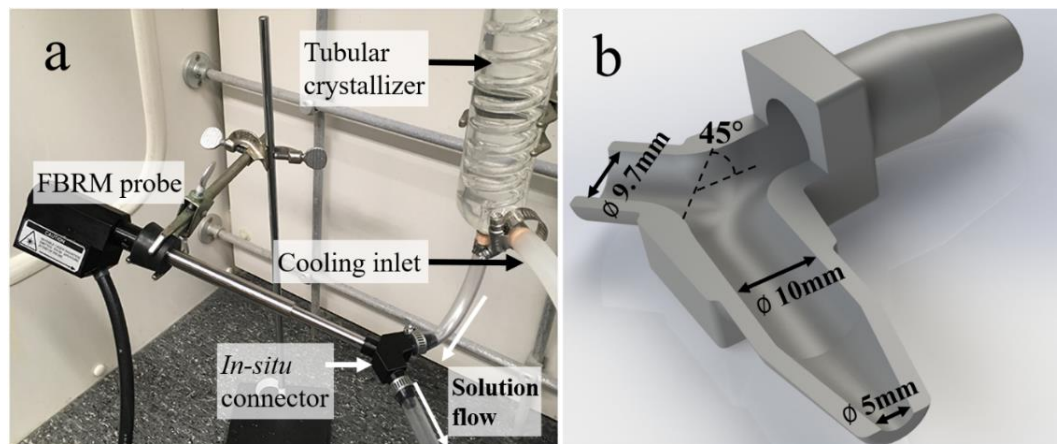
Figure 0-5: In-situ FBRM installation on a slender tubular crystallizer. (a) Picture of setup, (b) Cut-away view of the in-home designed model of in-situ connector

The principal component analysis (PCA). The conducted experiments were separated into two groups, one group included experiments with mean crystal size ranging from 5.0 to 15.0 microns and the other group included experiments with FBRM number density in the range from 500 to 1500 counts. These two groups were used to perform PCA, which can correlate the maximum variance with the fewest number of variables. It aimed to compress all the variables to a smaller number of sensitive operational variables, and then to control the MSMPR crystallizer more effectively.

The two groups of experiments were listed in the Table 0-4 and Table 0-5 below. Experiments in Table 0-4 were selected to analyze the factors that affect the seeds' mean size. Experiments in Table 0-5 were to analyze the key factors that determine the number density.

Table 0-4: Experiments in group one to analyze the principal components that effect the mean size of seeds ranging from 5.0 to 15.0 microns

Run #	T_n (°C)	S_0	N (rpm)	f (mL/min)	V_e (mL)	R_t (min)	Mean size (µm)	FBRM counts	Stdv (µm/#)	Crystal form
1	25.0	4.5	300	30	50	1.67	11.7	2864	1.6/378	α
3	25.0	3.0	300	50	50	1	5.6	547	1.1/143	α
4	25.0	2.5	600	30	50	1.67	10.4	840	1.9/112	α
16	25.0	2.5	900	30	50	1.67	9.3	1310	1.7/194	α
17	35.0	4.5	300	50	50	1	12.4	1966	2.3/247	α
18	35.0	4.0	300	30	50	1.67	12.3	2231	1.8/184	α
19	35.0	3.0	600	30	50	1.67	10.8	1178	1.5/175	α
7	35.0	2.5	600	30	50	1.67	9.2	545	1.8/92	α
20	35.0	2.5	900	50	100	2	11.8	1120	1.9/127	α
10	35.0	1.6	900	30	50	1.67	6.8	522	1.2/150	α
11	35.0	1.6	900	50	100	2	10.1	640	1.4/149	α
12	35.0	1.6	900	50	150	3	13.2	965	1.5/178	α

Notes: Supersaturation was calculated by $S_0 = \frac{C_0}{C^*}$, where C_0 is initial concentration and C^* is the saturated concentration at nucleation temperature; R_t was calculated by V_e/f; Stdv (µm/#) represents the standard deviation of mean size and FBRM counts. Each run was carried out at least three times and the reported mean size and FBRM counts represent the corresponding average values.

Table 0-5: Experiments in group two to analyze the principal components that effect the number density of seeds ranging from 500 to 1500 counts

Run #	T_n (°C)	S_0	N (rpm)	f (mL/min)	V_e (mL)	R_t (min)	Mean size (µm)	FBRM counts	Stdv (µm/#)	Crystal form
21	25.0	2.5	300	30	100	3.33	16.4	967	1.1/140	α
22	25.0	2.0	300	30	150	5	20.4	983	1.4/198	α
3	35.0	3.0	300	50	50	1	5.6	547	1.1/143	α
23	35.0	2.5	300	50	100	2	17.3	944	1.5/167	α
7	35.0	2.5	600	30	50	1.67	9.2	545	1.8/92	α
24	35.0	2.0	300	50	150	3	18.0	597	1.9/149	α
8	35.0	2.0	600	50	150	3	15.6	620	1.6/78	α
25	35.0	1.6	600	30	150	5	24.7	872	1.3/249	α
10	35.0	1.6	900	30	50	1.67	6.8	522	1.2/150	α
11	35.0	1.6	900	50	100	2	10.1	640	1.4/149	α
12	35.0	1.6	900	50	150	3	13.2	965	1.5/178	α
14	45.0	2.0	900	30	100	3.33	19.6	903	2.1/194	α&β

Table 0-6 and Table 0-7 show the parameters of operational factors from PCA for mean size and number density, separately. The first two principal components of both mean size and number density play the decisive roles in each group of experiments. The operational factors that matched a large absolute value in Table 0-6 and Table 0-7, were selected as the control factors in the first two principal components. V_e was the most sensitive factor in the first group experiments followed by N. As shown in Figure 0-6, compared with S_0, V_e and N indicated an obvious classification of experiments along with the axis of first component. So, V_e was selected as the most effective operational factor in controlling the mean crystal size. In the second group experiments, similar analysis indicated in Figure 0-7. V_e was the most sensitive factor in the first component and N was more sensitive in the second component. So, for number density optimization, V_e was also the first factor to be selected. N, as an independent factor, was selected as the second factor to control number density since V_e always resulted in the same direction of size and number density (either increase or decrease at the same time). For example, in the experiment of Size-/Counts+ (see Table

0-6), V_e was decreased to reduce the mean size which was accompanied by the decrease of number density. Increasing of N was the second factor to regain the number density.

Table 0-6: Parameters of operational factors from PCA for mean size

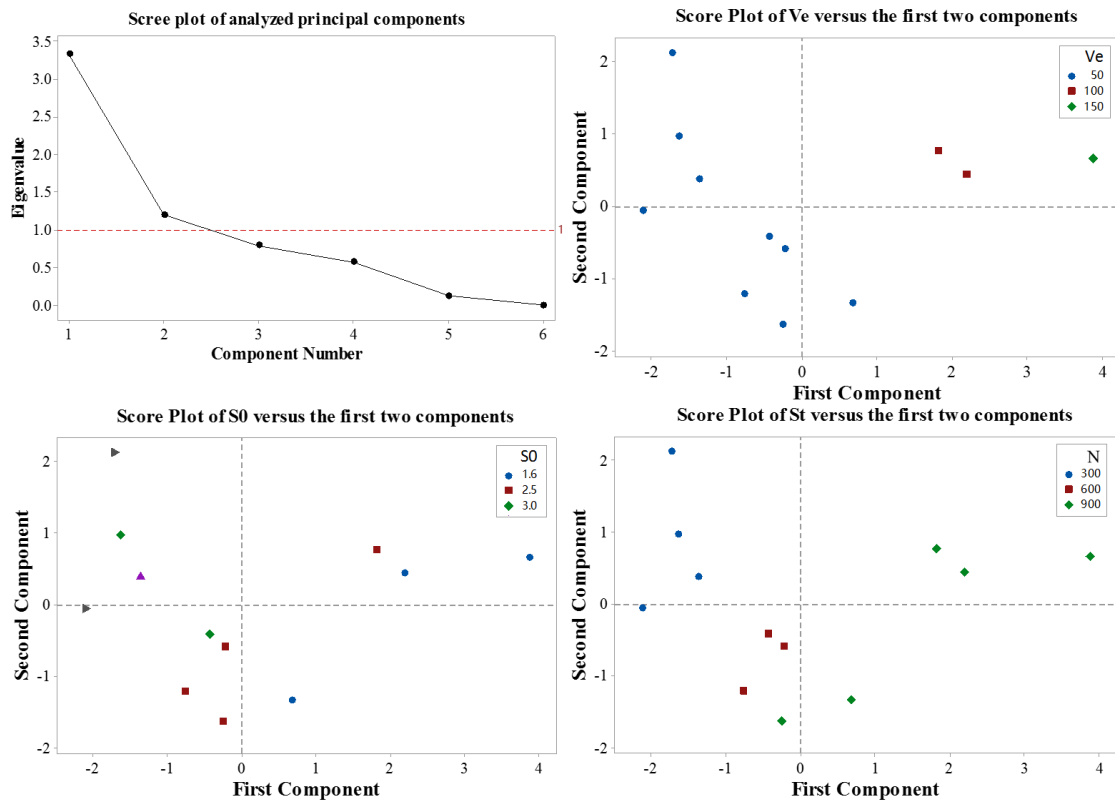| Variables	PC1	PC2	PC3	PC4	PC5	PC6
T_n	0.265465	0.302841	-0.90139	0.153704	0.041008	2.51E-16
S_0	-0.44245	0.37394	-0.11283	-0.45671	-0.66565	6.94E-17
N	0.460852	-0.37995	0.027652	0.311831	-0.73841	2.18E-16
f	0.239186	0.72492	0.372057	0.356342	-0.05931	0.385172
V_e	0.493618	0.290085	0.188257	-0.32742	0.027592	-0.72718
R_t	0.469584	-0.12016	-0.01128	-0.66058	0.075516	0.568205

Figure 0-6: Principal component analysis of the experiments with the mean size ranging from 5.0 to 15.0 microns. Scree plot that displays the eigenvalues versus the number of components in descending order; Score plot of V_e, S_0 and N versus the first two principal components

Table 0-7: Parameters of operational factors from PCA for number density

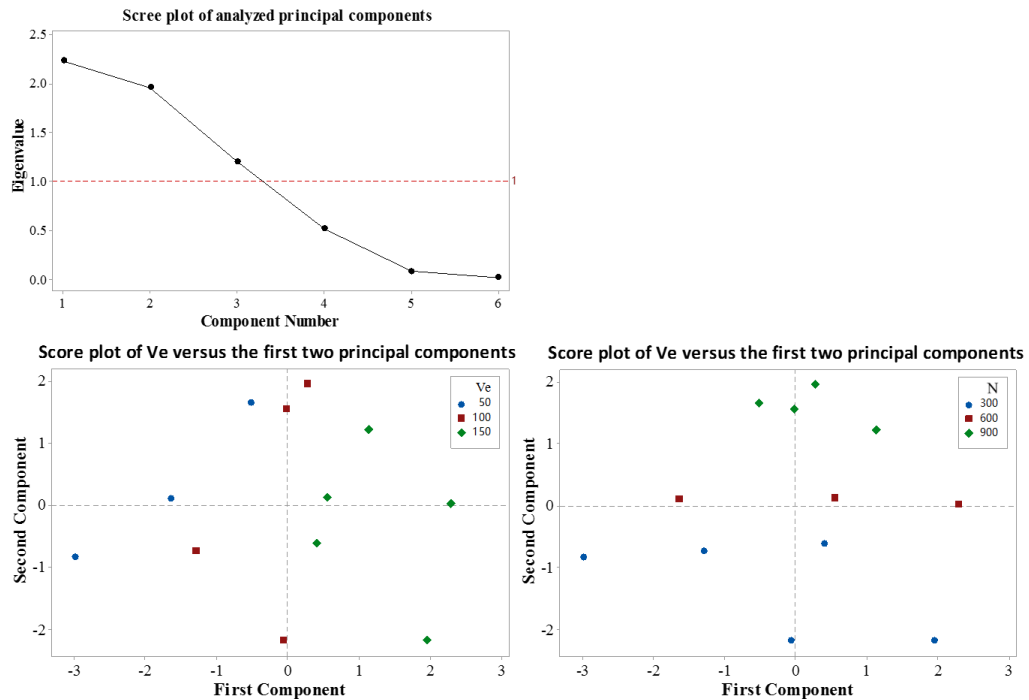| Variables	PC1	PC2	PC3	PC4	PC5	PC6
T_n	-0.12844	0.56984	-0.12377	0.771205	-0.22068	0.003576
S_0	-0.50145	-0.40529	0.020696	0.40394	0.646251	0.055197
N	0.128851	0.665915	0.144489	-0.25452	0.673733	-0.01953
f	-0.17651	0.058106	-0.86635	-0.18669	0.079512	-0.41681
V_e	0.560891	-0.13227	-0.4455	0.174911	0.20336	0.630467
R_t	0.608021	-0.21612	0.119765	0.334439	0.179079	-0.65218

Figure 0-7: Principal component analysis of the experiments with the FBRM counts ranging from 500 to 1500 counts. Scree plot that displays the eigenvalues versus the number of components in descending order; Score plot of V_e and N versus the first two principal components

Curriculum Vitae

Name: Zhenguo Gao

Post-secondary   Liaocheng University
Education and   Liaocheng, Shandong, China
Degrees: 2008-2012 B.A.

                             Tianjin University
                             Tianjin, China
                             2012-2019 Ph.D.

                             The University of Western Ontario
                             (Dual degree program with Tianjin University)
                             London, Ontario, Canada
                             2015-2019 Ph.D.

Honours and
Awards: Chinese Government Scholarship, 2015-2019
                             The Second Prize Scholarship in Tianjin University, 2012
                             The First Prize Scholarship in Tianjin University, 2013
                             National Encouragement Scholarship, Liaocheng University, 2010
                             The First Prize Scholarship in Liaocheng University, 2009, 2010

Related Work   Teaching Assistant
Experience   University of Western Ontario, 2016-2018

Affiliations/Memberships
American Institute of Chemical Engineers (AIChE), 2017, 2018, 2019

Publications:

Patents and Peer reviewed papers

1. **Zhenguo Gao**, *et al*. Self-induced Nucleation During Anti-Solvent Crystallization Process of Candesartan Cilexetil. *Cryst. Growth Des.,* 2018, 18 (12), 7655–7662

2. **Zhenguo. Gao**, *et al.* Image Analysis for In-line Measurement of Multidimensional Size, Shape, and Polymorphic Transformation of l-Glutamic Acid Using Deep Learning-Based Image Segmentation and Classification. *Cryst. Growth Des.* 2018, 18 (8), 4275-4281

3. **Zhenguo Gao**, *et al*. Continuous crystallization of α-form L-glutamic acid in an MSMPR-Tubular crystallizer system. *J. Cryst. Growth.* 2019. 507, 344-351

4. **<u>Zhenguo Gao</u>**, *et al*. Ultrasonic Irradiation and Seeding to Prevent Metastable Liquid-liquid Phase Separation and Intensify Crystallization. *Cryst. Growth Des* 2018, 18 (4), 2628–2635

5. **<u>Zhenguo Gao</u>**, *et al*. Motion-Based Multiple Object Tracking of Ultrasonic-Induced Nucleation: A Case Study of L-glutamic Acid. *Cryst. Growth Des* 2017, 17 (10), 5007-5011

6. **<u>Zhenguo Gao</u>**, *et al*. Recent Developments in the Crystallization Process: Toward the Pharmaceutical Industry. *Engineering.* 2017, 3 (3) 343-353

7. **<u>Zhenguo Gao</u>**, *et al.* From Jellylike Phase to Crystal: Effects of Solvent on Self-Assembly of Cefotaxime Sodium. *Ind. Eng. Chem. Res.* 2016, 55 (11), 3075-3083

8. Ying Bao, **<u>Zhenguo Gao</u>**, etc. A Preparation Method of Cefotaxime Sodium Crystals, *Patent CN* ,10489263 B. 2017, 6

9. Ying Bao, **<u>*Zhenguo Gao*</u>**, *et al*. Cefotaxime sodium N, N-dimethylformamide solvent compounds and preparation method, *Patent CN,* 103804395A. 2014, 5

10. Ying bao, Yongheng Yin, Yongli Wang, Haitao Zhang, Baohong Hou, **<u>Zhenguo Gao</u>** *et al.*, Preparation method of cefotaxime sodium crystal, *Patent CN,* 103275101A, 2013, 5

11. Xiandong Su, **<u>Zhenguo Gao</u>** *et al*. Gelation Mechanism of Erythromycin Ethylsuccinate During Crystallization, Transactions of Tianjin University 2018, 1-8

12. Yongheng Yin, **<u>Zhenguo Gao</u>** *et al*. Gelation Phenomenon during Anti-solvent Crystallization of Cefotaxime Sodium, *Ind. Eng. Chem. Res.* 2014, 53 (3), 1286-1292

13. Yongheng Yin, Ying Bao, **<u>Zhenguo Gao</u>**, *et al*. Solubility of Cefotaxime Sodium in Ethanol+ Water Mixtures under Acetic Acid Conditions. *J. Chem. Eng. Data*, 2014, 59 (6), 1865-1871

Conference Papers

14. **<u>Zhenguo Gao</u>**, et al. Investigation on the transition for gel to crystal of cefotaxime sodium, ISIC19 Sepember16-19, 2014, Toulouse, France, 52-54. Conference Paper

15. **<u>Zhenguo Gao</u>**, et al. (214e) Ultrasound-assisted crystallization in a two-stage continuous MSMPR crystallizer system. 2017 AIChE conference paper.

16. **Zhenguo Gao**, et al. (612f) Motion-Based Multiple Object Tracking of Ultrasonic-Induced nucleation: A Case Study of L-Glutamic Acid. 2017 AIChE conference paper.

17. **Zhenguo Gao**, et al. (610g) Imaging Crystallization Using Deep Learning to Quantitatively Track the Polymorphic Transformation of Carbamazepine, 2018 AIChE conference paper.

Academic Actives:

1. **Volunteer**, 19th International Workshop on Industrial Crystallization, BIWIC 2012, Tianjin, China (Sep. 2012)

2. **Volunteer**, 3th chemical engineering academic exchange conference of the young scientists in China, Tianjin, China (May 2013)

3. **Speaker**, 19th International Symposium on Industrial Crystallization, ISIC19, ISIC19,Toulouse, France, (Sep. 2014)

4. Chinese National industrial crystallization symposium, Guiyang, CHINA, **Poster**. (July 2017)

5. **Speaker**, 20th International Symposium on Industrial Crystallization, ISIC20, Dublin, IRLAND. (Sep. 2017)

6. **Speaker**, AIChE 2017 Annual Meeting in Minneapolis, MN, United States, (Oct. 2017)

7. **Speaker**, AIChE 2018 Annual Meeting in, Pittsburgh, PA, United States, (Oct. 2018)